MICROSTRUCTURE AND TRANSPORT IN CORRODED PROTON EXCHANGE MEMBRANE FUEL CELL CATHODES

A Dissertation
Presented to
The Academic Faculty

by

Andrew Gillmore Star

In Partial Fulfillment
of the Requirements for the Degree
Doctor of Philosophy in the
School of Chemical and Biomolecular Engineering

Georgia Institute of Technology
August 2018

MICROSTRUCTURE AND TRANSPORT IN CORRODED PROTON EXCHANGE MEMBRANE FUEL CELL CATHODES

Approved by:

Dr. Thomas F. Fuller, Advisor
School of Chemical & Biomolecular Engineering
Georgia Institute of Technology

Dr. Sankar Nair
School of Chemical & Biomolecular Engineering
Georgia Institute of Technology

Dr. Faisal Alamgir
School of Materials Science & Engineering
Georgia Institute of Technology

Dr. Gleb Yushin
Materials Science & Engineering
Georgia Institute of Technology

Dr. Paul A. Kohl
School of Chemical & Biomolecular Engineering
Georgia Institute of Technology

Date Approved: April 23, 2018

Dedicated to my exemplars: Kelly, Moe, and particularly, Garry, sine qua non.

ACKNOWLEDGEMENTS

I graciously acknowledge the people who have shaped me as a researcher and as a person. It is my hope that this dissertation represents a small portion of a career that will pay forward the many favors that have been paid unto me. Many people deserve acknowledgement: Tom Fuller allowed me to pursue science in the capacity of both "pure" and "applied" practitioner, including stumbling and failing, which led to important moments of growth and helped me stay focused on the science, move beyond trifles and politics, and always strive to make important contributions. Group members (and friends) were always kind, helpful, and intellectually inspiring: Brian Setzler, Vyran George, Tapesh Joshi, Rajiv Jaini, Greg Chipman, Jung Fang, and Jon Grunewald. Toyota Motor Corporation financially supported this work and Norimitsu Takeuchi offered helpful suggestions from the perspective of industry. Kenneth Neyerlin, Brian Pivovar, and the fuel cell group at NREL went to great lengths to support me and help refine ideas. Past mentors have impacted me in ways that have endured over many years: Andrew Udit, Aditya Khair, Michael Hill, and Aram Nersissian. For brevity, I forgo elaboration of a very long list of family, friends, and a Singaporean dinosaur who are incredibly dear to me and whom I consider contributors to this and all my works by supporting me over many years in many different forms.

TABLE OF CONTENTS

LIST OF TABLES

LIST OF FIGURES

LIST OF SYMBOLS AND ABBREVIATIONS

ΔG	Gibbs Free Energy Difference [J]
R	Gas Constant [J/mol/K]
T	Temperature [K]
k_B	Boltzmann Constant [$m^2kg/s^2/K$]
n	Electron equivalents
F	Faraday's constant [secAmps/mol]
a_m	Activity of species m
s_m	Stochiometric coefficient of species m
U_{cell}	Cell potential [V]
η_y	Cell overpotential arising from y [V]
ε	Porosity
τ	Tortuosity
τ_g	Geometric tortuosity
δ	Constrictivity
δ_g	Geometric constrictivity
$\tau_{Dijkstra}$	Tortuosity by Dijkstra algorithm
$\bar{\varepsilon}_{MB}$	Porosity by mass balance approach
$R_{i/j}$	Mass ratio of species i to species j
ρ_i	Mass density of species i [kg/m^3]
m_i	Catalyst loading [g/cm^2]
L	Thickness of relevant layer [m]
$S_2(r)$	Two-point correlation function

$C_2(r)$	Two-point cluster function
$D_{i,Kn}$	Diffusivity of species i in Knudsen regime [m^2/s]
$D_{i,m}$	Diffusivity of species i in molecular regime [m^2/s]
D_i^{eff}	Effective diffusivity of species i [m^2/s]
$\widetilde{D}$	Linearly parameterized diffusivity [m^2/s]
$C_{i,j}$	Concentration of species i at location j [mol/m^3]
RH	Relative humidity
b_1	Tafel slope
i_d	Current density [A/cm^2]
$i_{d,lim}$	Limiting current density [A/cm^2]
$E(\xi_i)$	Energy of the i^{th}microstructural instantiation
$\boldsymbol{F}_{ij}$	Interaction force between particles i and j
r_{ij}	Adjusted distance between particles i and j
x_{ij}	Distance between particles i and j
α	Obstruction Factor
α_{CFD}	Obstruction Factor by CFD
α_g	Geometric obstruction factor
r	Pore radius [m]
M_i	Molar mass of species i [kg/mol]
$\widetilde{N}$	Avogadro's number
σ	Lennard-Jones collision length [m]
Ω	Diffusion collision integral
λ	Mean free path [m]
$R_{i,j}$	Transport resistance of species i in location/layer j

ψ_{iono,O_2}	Permeation coefficient of oxygen through ionomer
Σ	Diffusion volume

SUMMARY

Impressive development of proton exchange membrane fuel cells (PEMFC) has been accomplished over the past several decades. Unfortunately, adoption of PEMFC technology has been slow despite global belief that electrified transportation is necessary in response to increasing pollution in cities and impending destabilizing effects of climate change. Cost and durability are the most pressing issues preventing commercialization and the cathode, the subject of this thesis, is the most expensive and least durable component. Further improvement will be required to realize widespread adoption of PEMFCs.

PEMFC degradation and transport were investigated, with emphasis on the microstructure of catalyst coated membrane cathode layers of platinum-catalyzed, H_2-fueled cells. A central contribution of this thesis was to advocate for and bring to bear new information and new techniques to better quantify the connection between cathode transport and degradation. The principal experimental accomplishment was development and use of focused ion beam and scanning electron microscope tomography that enabled direct three-dimensional imaging of degraded cathode catalyst layers. Much of the subsequent analysis relied upon information obtained by this method.

Albert Einstein is widely credited with the remark, “everything should be made as simple as possible, but no simpler.” A sincere attempt was made to compose this thesis in its most succinct form, directing the reader elsewhere for topics which have been conclusively elaborated upon, especially uncontroversial foundational knowledge, so that this document may serve as the most concise possible record of the novel contributions that were made. Computer codes were not appended but can all be made available upon request.

CHAPTER 1. INTRODUCTION

Proton exchange membrane fuel cells (PEMFC) convert hydrogen fuel and oxygen into water while generating electric power. PEMFCs are electrochemical reactors and a leading candidate technology to replace internal combustion engines (ICE) and enable a clean energy future. Unfortunately, cost and durability targets remain unmet largely due to the expense of the cathode layer and the various degradation mechanisms the unravel its desirable properties. This thesis aims to address the least well understood degradation mode, carbon catalyst support corrosion, in the cathode layers as this is one of the most urgent problems preventing PEMFC technology from competing in classical markets.

1.1 Energy and Transportation in the 21st Century

Two cornerstones of modern human civilization are rapid transmission of information and material, including people. Information was transmitted orally, then by telegram, telegraph, and now by satellite, at nearly the speed of light. Material has moved at the pace of geology, then by walking, horse, ship, train, car, and now aviation. Unfortunately, conveying great sums of mass requires great sums of energy.

In 2016, 71% of energy consumed in the United States originated from non-renewable, carbonaceous primary sources.[1] The United States Energy Information Administration forecasts predict that energy consumption behavior, modeled with various assumptions, is very unlikely to decrease over a reasonable near-term time horizon.[1] These tendencies and trends are similar globally.[2] Unfortunately, humanity's energy consumption

behavior results in air pollution and climate change. The Mauna Loa CO_2 concentration measurements are now famous while cities like Los Angeles notoriously collect dangerous concentrations of criteria pollutants largely originating from ICE automotive transport.

The transportation sector is responsible for nearly 30% of the total US energy consumption and generates approximately 20% of total global CO_2 emissions.[1] These must decrease to zero or very nearly zero to avoid the "real" and "present security threat" of climate change.[3] Argonne National Laboratory's Greenhouse Gases, Regulated Emissions, and Energy Use in Transportation (GREET) model has convincingly shown that an electrified fleet powered by a fully renewable source, via battery electric vehicles and/or fuel cell vehicles, is the only way to reduce well-to-wheel automotive green-house gas emissions to zero.[4] Replacing internal combustion engines with an electrified fleet powered by renewables also carries the benefit of eliminating tail-pipe, criteria pollutant emissions such as NOx, SOx, CO, and combustion-related hydrocarbons in densely populated city areas. For these reasons, improvement and adoption of PEMFC technology is considered highly desirable and arguably, necessary.

1.2 Proton Exchange Membrane Fuel Cells

An incredible number of lengthy and comprehensive books, chapters, and handbooks on the fundamentals of PEMFC physics, chemistry, and optimal operation have been written over several decades. For example, excellent texts were compiled by Vielstich, Lamm, Gasteiger, and Yokokawa in 2003, O'Hayre, Cha, Colella, and Prinz in 2005, Subramanian in 2006, Mench in 2008, and a handbook commissioned the Department of Energy which saw it *seventh* and most recent edition published in 2004. For further

appreciation of the myriad coupled engineering challenges and the scope of fuel cell engineering, a concise history of developments that led to modern PEMFC technology and the most important remaining problems was compiled by Perry and Fuller.[5]

A proton exchange membrane fuel cell (PEMFC) is an electrochemical reactor and energy conversion device that generates electric work by electrochemically oxidizing hydrogen fuel at the anode while reducing molecular oxygen and protons to water at the cathode. Figure 1 demonstrates operation of the membrane electrode assembly (MEA), the three most essential components of a PEMFC, the anode, proton-exchange membrane (PEM), and the cathode. Oxygen atoms are depicted in red, protons in light blue, and electrons in orange.

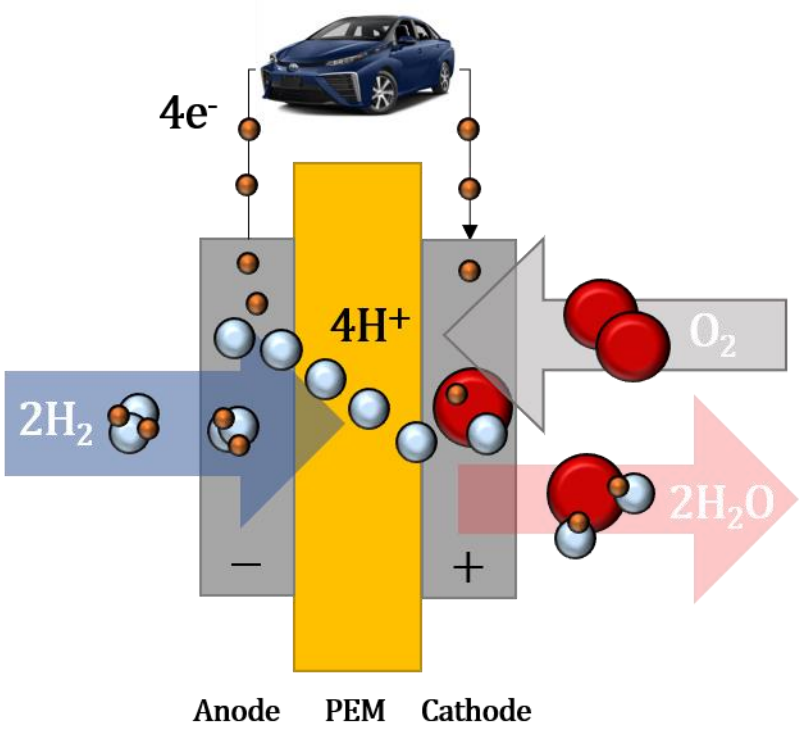

Figure 1 - Diagram of PEMFC operation. Hydrogen fuel is oxidized at the anode. Protons cross the PEM and recombine with oxygen as it is reduced to product water. Electron pass through an external circuit to generate electric work. Heat is generated from the net reaction.

The overall electrochemical reaction of the cell is given by Equation (1-1).

$$H_2 + \frac{1}{2}O_2 \rightarrow H_2O \tag{1-1}$$

The ideal half reactions, hydrogen oxidation (HOR) and oxygen reduction (ORR), are given by Equation**Error! Reference source not found.** (1-2) and Equation (1-3).

$$H_2 \rightarrow 2H^+ + 2e^- \tag{1-2}$$

$$\frac{1}{2}\mathrm{O_2} + 2\mathrm{H^+} + 2\mathrm{e^-} \rightarrow \mathrm{H_2O} \tag{1-3}$$

From the Gibbs free energies of the products and reactants, the Nernst equation predicts the maximum expected or reversible electrical potential of a H_2/O_2 cell.

$$U_{Nernst} = \frac{-\Delta G^{o}}{nF} + \frac{RT}{nF}\ln\left(\prod_m a_m^{s_m}\right) \tag{1-4}$$

U_{Nernst} is the Nernstian, equilibrium cell potential, ΔG^{o} is the reversible Gibbs free energy of reaction at standard pressure and at cell temperature T, n is the number of electron equivalents, F is Faraday's constant, R is the gas constant, a_m is the activity of reacting species m, and s_m is the stoichiometric coefficient, negative for products and positive for reactants, of species m. At standard conditions, the thermodynamic potential of an ideal H_2/O_2 cell is 1.229 V while at typical operating conditions, this potential resides between 1.1 and 1.2 V depending on the activities of the species and whether product water forms as liquid or vapor. The maximum thermal efficiency of an H_2/O_2 electrochemical cell, assuming the lower heating value of water, is obtained by $\Delta G/\Delta H$ and is 90% or greater depending on the operating temperature of the cell. In practice, real PEMFC systems are typically ~65% efficient compared to real ICEs which are typically 20-30% efficient. In consideration of replacing ICEs with PEMFCs, it should be noted that PEMFCs also operate at much lower (i.e., safer) temperature and have no moving parts.

A complete PEMFC system requires supporting components to enable operation. Single cells are typically tested when investigating cell- and smaller scale phenomena with

the understanding that cells can be arranged serially into "stacks" to achieve a power output suitable for transportation and/or stationary applications. Single-cell testing requires single-cell flow fields for reactant (fuel) delivery and electronic conduction, porous diffusion media to facilitate gas and liquid water exchange between the flow fields and the electrodes while conducting electrons, and current collectors (and wires) as electronic interfaces between the flow fields and an external electric load such as an electric motor. PEMFC stacks require external cooling to meet the heat rejection requirement of the exothermic reaction while single-cell, research-scale hardware typically requires heating to maintain controlled temperature conditions due to the low total heat generated per unit volume of hardware. A graphical teardown of the full PEMFC "sandwich" is shown in Figure 2.

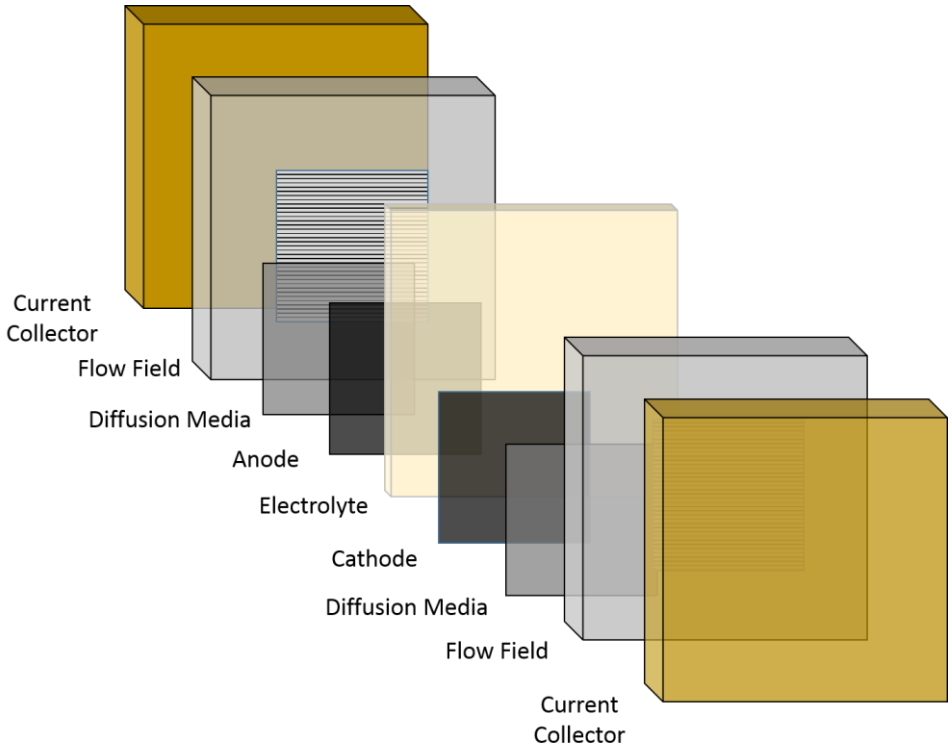

Figure 2 – Graphical teardown graphic of the single-cell hardware and various components comprising the PEMFC "sandwich."

1.3 Perspective and Current Issues in PEMFCs

As in any real system, PEMFCs do not achieve their theoretical limits and engineers seek to minimize the difference between real and theoretical performance. This analysis typically begins with an accounting of various deviations (losses, or "overpotentials") from the thermodynamic Nernst cell potential and is written as Equation (1-5) where absolute values are used to ensure overpotentials are subtracted when they would otherwise be added due to convention regarding the direction of current in a cell.

$$U_{cell} = U_{Nernst} - \eta_{act,a} - \left|\eta_{act,c}\right| - \eta_{iR} - \eta_{MT,a} - \left|\eta_{MT,c}\right| - \eta_{ix} \qquad (1\text{-}5)$$

U_{cell} is the observed/measured cell potential. $\eta_{act,a}$ is the activation overpotential at the anode, arising from the energy per unit charge required to overcome the activation barrier of HOR. $\eta_{act,c}$ is the activation overpotential at the cathode arising from ORR. η_{iR} is the sum of "Ohmic" overpotentials that arise from the finite electronic and ionic resistivity of the materials used in the PEMFC sandwich. $\eta_{MT,a}$ is a "mass transport" overpotential at the anode that arises from the finite timescale of reactant transport from flow-field to catalyst surface and $\eta_{MT,c}$ is the mass transport overpotential at the cathode. η_{ix} is an overpotential arising from crossover of H_2 (fuel) through the PEM, from the anode to cathode, that gives rise to a mixed-potential at the cathode thereby lowering the observed open-circuit potential from the theoretical open-circuit potential. η_{ix} can also be increased through introduction of impurities or unintended short-circuits in the cell.

This accounting serves as a starting point for PEMFC research wherein the apparent engineering objective is to minimize the sum of the overpotentials. In state-of-the-art PEMFC systems, $\eta_{act,a}$ and $\eta_{MT,a}$ are small and in some cases neglected thanks to the facile kinetics of HOR and the small collisional cross-section, i.e., large diffusivity, of molecular hydrogen. η_{iR} can often be assumed equal to the η_{iR} of the PEM due to the much greater electronic conductivity of carbon, flow fields, and current collectors compared to the proton conductivity of PFSA in the PEM. η_{iR} is minimized through adequate PEM hydration and use of thinner membranes although, thinner membranes may permit additional reactant crossover which may increase η_{ix}. Finite η_{ix} is to some extent considered an irretrievable loss as molecular hydrogen's small collisional cross section allows it to permeate all materials, including PFSA membranes, at a low but non-trivial rate. The two remaining overpotentials arise from the cathode layer, $\eta_{act,c}$ and $\eta_{MT,c}$. These

two overpotentials dominate cell losses at high current density thereby preventing high power density operation which undermines the fundamental rationale for adopting PEMFCs over, for example, battery-powered transport applications.

A spider diagram as in Figure 3 succinctly demonstrates the status of and progress made toward relevant technical targets that would enable PEMFCs to compete in markets.[6]

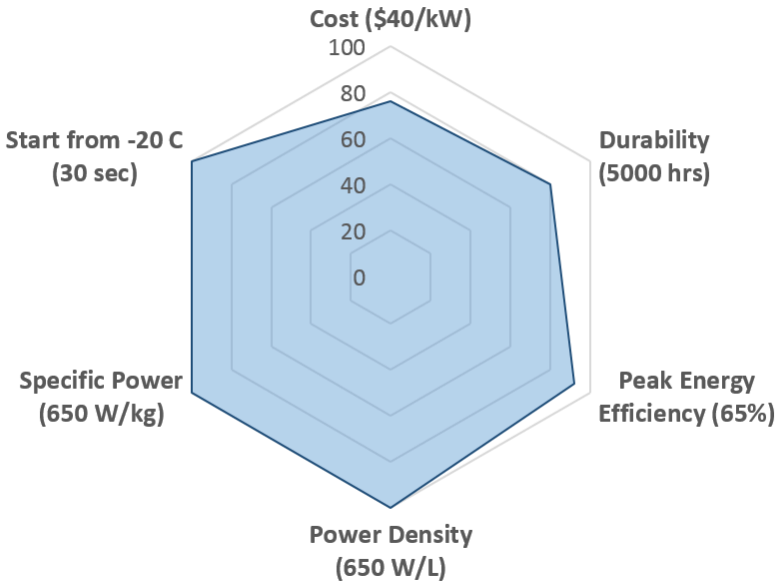

Figure 3 - Department of Energy-specific technical targets and progress made as of June 2017 by percent of target achieved in state-of the art PEMFCs.

Cost and durability targets lag in state-of-the-art systems although it is important to note that these targets are highly coupled; making progress on one target in exchange for a loss on another target is generally not desirable. A further breakdown of the current costs of stack components, assuming an as-intended scaled-up industry of 500,000 stacks fabricated per year is shown in Figure 4.[6]

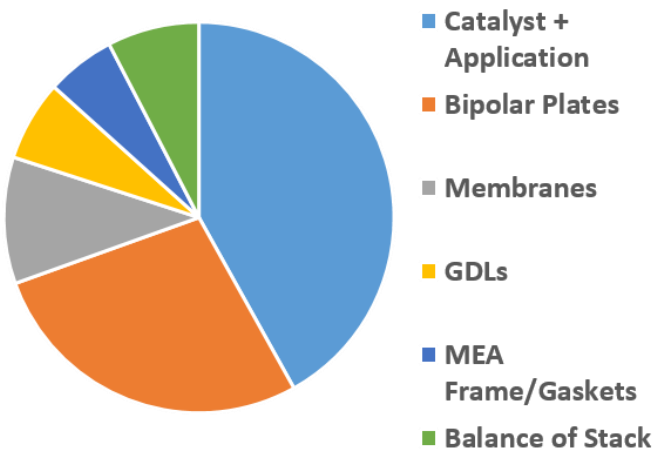

Figure 4 – DOE estimation of breakdown of stack cost by component

The cathode catalyst layers are the single most expensive component largely due to the necessary reliance on platinum as electrocatalyst to facilitate ORR. Research for new and improved materials will always proceed however, it is commonly believed that platinum or platinum-alloy spherical-particle catalyst, carbon black catalyst support, and Nafion® or similar PFSA ionomer must be used to simultaneously achieve the cost, performance, and durability targets. Moreover, it has been shown that any eventual architecture must be scalable up to the rate of ~1 MEA/second, severely constraining the prospect for complex materials that require elaborate syntheses.[7] Accordingly, the preponderance of contemporary PEMFC research involves optimizing features of the cathode catalyst layer. Taking these considerations together, this thesis aimed to make contributions *within* these boundaries, supposing that such contributions could be utilized within a reasonable time horizon.

1.4 Degradation and Corrosion in PEMFCs

All materials degrade over time but the kinetics of degradation will significantly affect the choice of specific materials and/or processing conditions used in commercial systems. Platinum electrocatalyst degrades through several mechanisms including particle dissolution, ripening, detachment, migration, and re-precipitation all of which have been studied extensively [cite several]. These mechanisms are all considered destructive in that they reduce the electrochemically active surface area (ECSA) available to catalyze ORR, a severe penalty to pay when using an expensive catalyst. The proton-exchange membrane and ionomer may degrade chemically and/or mechanically. The C-F bonds prevailing in PFSA resist chemical attack but are not impervious; trace hydrogen crossover to the cathode may result in peroxide generation near the PEM/cathode interface which chemically degrade PFSA on non-trivial timescales.[8] Thermal and relative humidity cycling induces swelling in PFSA which can lead to mechanical failure. The carbon catalyst support degrades by oxidation (corrosion). Carbon support corrosion remains insufficiently quantified and understood, despite several demonstrated effects in experiments that intentionally induced carbon corrosion. For this reason, corrosion is a central thrust of this thesis.

Corrosion (oxidation) of the carbon catalyst support is thermodynamically spontaneous at the operating conditions of interest.[9] Thus, corrosion proceeds during normal cell operation and is greatly accelerated by temperature and transiently elevated cell potentials experienced over the lifetime of a PEMFC.[10,11] Corrosion can degrade the desirable properties of the cathode via adverse material loss and rearrangement.[8] Specific adverse effects include electrical isolation of platinum and/or carbon, underutilization of Pt catalyst, loss of hydrophobicity which promotes flooding, and collapse of porous

microstructure.[8] Products of corrosion, CO and CO_2, may cause further damage to the membrane and/or poison the Pt catalyst. Electrochemical carbon corrosion proceeds by the following generalized reaction,[12]

$$C + 2H_2O \rightarrow CO_2 + 4H^+ + 4e^- \qquad U^\theta = 0.207\ V \qquad (1\text{-}6)$$

U^θ denotes the standard potential of the reaction. Diverse carbon-oxide surface moieties may arise before oxidation to carbon dioxide and catalytic coupling between the carbon-oxides, electrocatalyst, and ionomer influence the kinetics, likely accelerating the corrosion reaction.[13] Loss of electrochemical surface area (ECSA) typically accompanies corrosion;[8] however, despite the voltage penalty incurred by catalyzing the oxygen reduction reaction, full cell modeling[14] and TEM imaging[15] suggest that cathode mass transport losses overtake kinetic (activation) losses as the dominant fraction of cell voltage losses following extensive corrosion.[10,14] Indeed, extensive corrosion leads to a "collapse" of the cathode microstructure which may obstruct transport of oxygen, protons, and/or water.[16] Corrosion mechanisms have been proposed but none are considered conclusively predictive and it is increasingly believed that the precise interplay of all the constituent materials must be accounted for to develop adequately predictive models.[13,17,18,19,20] In 2018, corrosion remains one of the most critical and least comprehensively understood degradation modes preventing PEMFCs from achieving the simultaneous performance/cost/durability targets and reaching widescale adoption. This thesis aimed to address this shortcoming.

1.5 Modeling and Microstructure in PEMFCs

Porous electrode theory, particularly as advanced by John Newman and successors over several decades,[21] provides the most important foundation for thinking about PEMFC cathodes mathematically, i.e., quantitatively. In component and full-cell mathematical models, porous (multi-phase) media are often macro-homogenized, averaged from a top-down or "bulk" perspective, and treated as a single-phase with effective properties due to the difficulty of reliably resolving microscopic and nanoscopic inhomogeneities and the extreme computational cost of modeling and simulation of highly resolved systems as compared to reduced complexity systems.

Recently, however, advances in microscopy have improved the fidelity of imaging and brought down cost substantially. Indeed, understanding the precise structure of the porous electrodes at the microscale throughout a cell's service life is imperative to achieving the performance demanded by technical targets and can now be assessed at accessibly low cost. One of the major overarching suppositions of this thesis was that advanced microscopy may be incorporated as an efficient characterization tool for accelerating the rate of progress of cathode and full PEMFC development. PEMFC stack cost reduction is currently not on pace to meet DOE specified targets derived from the need to reduce pollution and CO_2 emissions as discussed in Section 1.1. Thus, to make progress on PEMFC technology at the desired rate, this thesis argues for and contributes to resolving the realm of the very small to improve fundamental understanding of relative degradation rates and the performance implications thereof.

The remainder of this thesis is divided into five chapters. Chapter two discusses the advantages, disadvantages, and developments of the FIB-SEM technique used throughout. Chapter three details a project that investigated the hypothesis of corrosion-induced

cathode collapse using the novel approach of FIB-SEM. Chapter four demonstrates the potential for adopting advanced tomography coupled with computational calculations as a standard characterization technique for engineers. Chapter five utilizes the tools of developed in previous chapters to compare two leading candidate carbon blacks as catalyst support. Chapter six discusses a project for enhancing the fidelity of FIB-SEM that never quite left the ground but could be promising starting point for some ambitious researcher in the future.

CHAPTER 2. FOCUSED ION BEAM-SCANNING ELECTRON MICROSCOPE TOMOGRAPHY

The marquee technique developed and utilized for the work in this thesis was focused ion beam and scanning electron microscope tomography (FIB-SEM). Advocating for and advancing the use of FIB-SEM for characterizing PEMFC cathodes was perhaps the most important contribution of this thesis. The technique was sufficiently challenging and important enough to requisite its own chapter as subsequent chapters make extensive use of the imaging data obtained. All FIB-SEM work was performed on an FEI Nova Nanolab 200 owned and operated by the Institute for Electronics and Nanotechnology at Georgia Institute of Technology. This chapter includes an introduction to FIB-SEM tomography, description of the specific challenges of using FIB-SEM on PEMFC cathodes, and discussion of the developments made for use on corroded PEMFC cathodes.

2.1 Introduction to FIB-SEM Tomography

Tomography is the technique of mapping interior projections of volumes and is widely utilized in materials science. Many people have basic familiarity with a "brain scan," a form of tomography. FIB-SEM tomography requires material sectioning (removal) and surface imaging for data acquisition in contrast to techniques such as transmission electron microscopy or x-ray computed tomography that non-destructively image projections through a tilt series.[22] Destructive tomography is like slicing through a loaf of bread, slice by slice, in order to see inside. FIB-SEM tomography has successfully characterized numerous materials including solid oxide fuel cells, geological samples, and

Li-ion batteries.[23,24,25] The first demonstrations of FIB-SEM on a PEMFC cathode came from Ziegler et al. and Schulenburg et al., both in 2011.[26,27]

FIB-SEM of PEMFC cathodes is a challenging technique compared to many other established methods; however, lack of consensus in basic characterization measurements and model parameters used to represent real PEMFC cathodes justifies the need for FIB-SEM. As one example, Dobson et al. collected the parameters used by dozens of PEMFC cathode models across literature and found researchers used values ranging between 0.1 and 0.5 for cathode agglomerate porosity.[28] Models cannot be predictive without accurate parameters and the use of advanced imaging such as FIB-SEM can reduce uncertainty in these parameters and improve fundamental characterization capabilities.

2.2 FIB-SEM Tomography of PEMFC Cathodes

FIB-SEM offers great promise in characterizing PEMFC cathodes because of the length scales of the materials comprising the cathode. Figure 6 depicts the architecture of a conventional cathode catalyst layer.

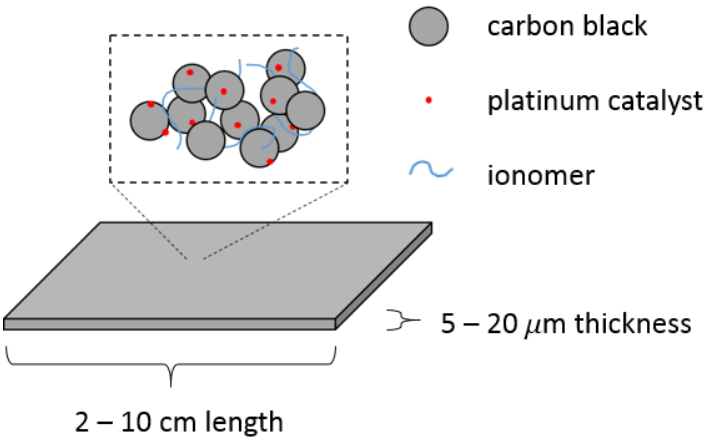

Figure 5 – Graphic demonstrating a cathode and its constituent materials.

Carbon black catalyst support comprised of 30-50 nm diameter primary particles are decorated with nanometer-diameter platinum catalyst nanoparticles and interspersed with PFSA (often, Nafion®) ionic-conducting polymer (ionomer). These materials tend to associate into aggregates and aggregates may form larger "agglomerate" structures although the dynamics governing aggregation are poorly understood and depend strongly on the species fractions and processing conditions used. Cathode layers are typically 5 – 20 μm thick and approximately 2 – 10 cm in length.

Given these characteristic lengths, FIB-SEM is arguably the only known method of tomography capable of resolving all or most of the relevant materials while imaging volumes large enough as to be statistically representative of the entire cathode. Several excellent reviews on tomography bear this out.[22,29,30] Although x-ray nano-CT approaches the resolution limits necessary for imaging the mesoporous structure of cathode catalyst layers, Wargo et al. compared to x-ray nano-CT and FIB-SEM in a PEMFC microporous layer (MPL) and convincingly showed that a substantial amount of fine detail was lost due to the diffraction-limited spatial resolution of x-rays as compared to electrons.[31]

Importantly, cathode layers have smaller features than microporous layers. Non-trivial detail was lost in imaging MPL layers with x-rays, which guarantees that non-trivial detail would be lost in evaluating cathode layers with x-rays. Because the ultimate objective of PEMFC research is to improve full cell performance through optimizing cathode transport and FIB-SEM is the most promising method for direct imaging, expanding research efforts on FIB-SEM of cathode layers will likely yield important results.

Successful FIB-SEM requires both the physical acquisition of images and their digital reconstruction into a volume. The two components are described separately although it must be noted that success in the digital (downstream) component requires satisfactory success in the physical component. Figure 6 demonstrates the FIB-SEM workflow. A cathode sample is mounted onto a sample stub. A region of interest (ROI, also referred to later as volume of interest, VOI), a sub-volume of the cathode, is chosen and serial imaging and interior cross-section surface material removal advance through the ROI. The result is a stack of 2D SEM images. These images are digitally segmented into pore and solid phase then interpolated into a volume.

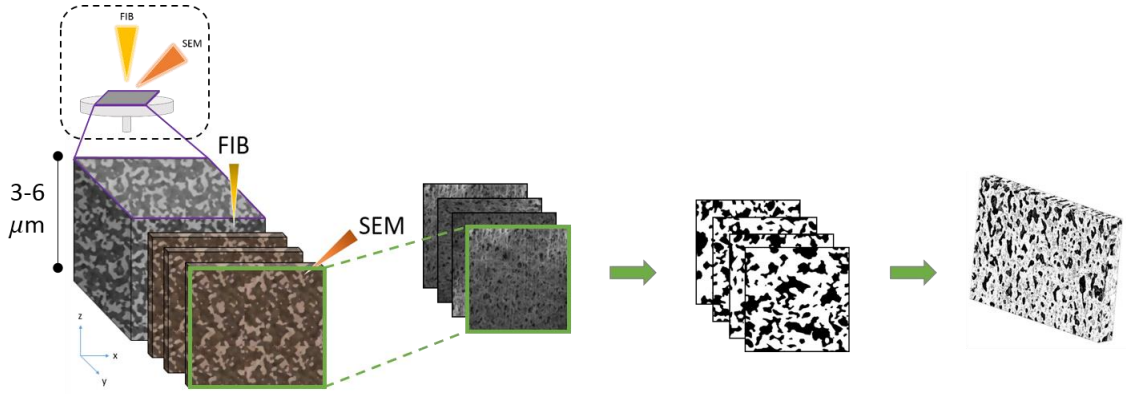

Figure 6 – FIB-SEM tomography demonstrated in full

A visualized example of the final output of FIB-SEM is provided in Figure 7.

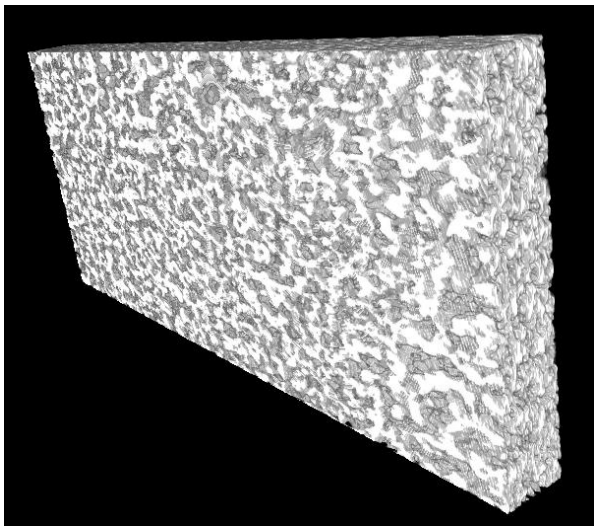

Figure 7 – Example visualization of final FIB-SEM tomography result. Volume displayed is approximately 4 μm × 2 μm× 0.5 μm.

2.2.1 Physical Component

The physical component of FIB-SEM includes SEM imaging and FIB serial surface material removal. Another graphic of the sample setup, orientation of the dual beams, and progression of serial slicing and surface imaging is shown in Figure 9.

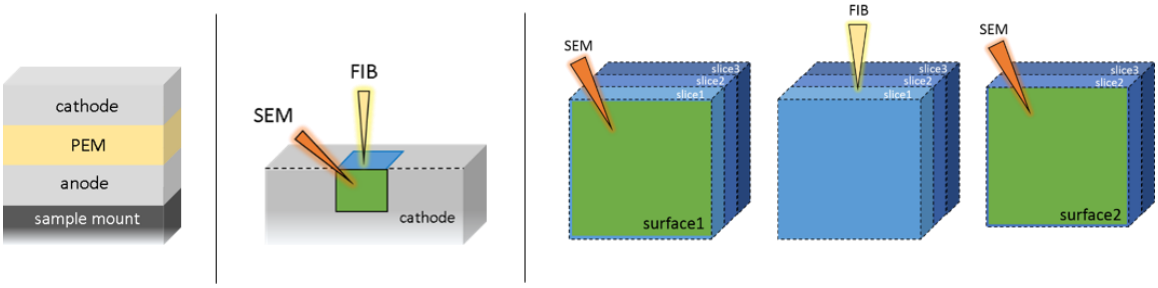

Figure 8 - Setup and orientation of the cathode layer for FIB-SEM tomography (left), orientation of the dual beams relative to the ROI (middle), and depiction of serial surface removal (slicing) and imaging (right).

An extremely valuable but often underappreciated benefit of FIB-SEM is the ability to interrogate the microscopic structure and properties of *as-fabricated* cathode layers as compared to individual constituent materials. For example, BET porosity and pore size distributions are often reported for Pt/C and other catalysts but this measures the properties of the catalyst powder, not the as-fabricated cathode. Moreover, significant evidence exists suggesting that catalyst coated membranes, gas diffusion electrodes, and decal electrodes differ in various properties and performance due to the complicated dynamics that occur during catalyst ink drying.[32] Catalyst ink deposited on to a substrate introduces structural order at the interface which propagates into the layer.[33] All of this suggests that there is considerable reason to believe that studying the as-fabricated electrode is the best approach for evaluating cathode properties and successful FIB-SEM may be the best method for doing so.

Successful physical FIB-SEM requires high-fidelity scanning electron imaging and minimization of artificial error by the focused ion beam. PEMFC cathode layers are considered a challenging FIB-SEM application due to the highly porous structure and low mechanical rigidity of the layer. Toward enabling successful FIB-SEM, on-tool parameters were varied to minimize ion beam artifacts including incomplete sputtering, material redeposition, inadequate heat dissipation,[34,8] and to ensure high fidelity imaging of the high porosity microstructure.[35,27,36] Combinations of FIB accelerating voltage, ion flux (ion beam current through a given area), and ion fluence, the integral of the ion flux over the time of beam application, were tested to minimize error. These studies are typically considered required workup for FIB-SEM applications and become more important given the challenge of this specific application.[34] An example of "curtaining," an artificial obscuring of the to-be-imaged surface often caused by the use of excessive ion beam current, is shown in Figure 10.

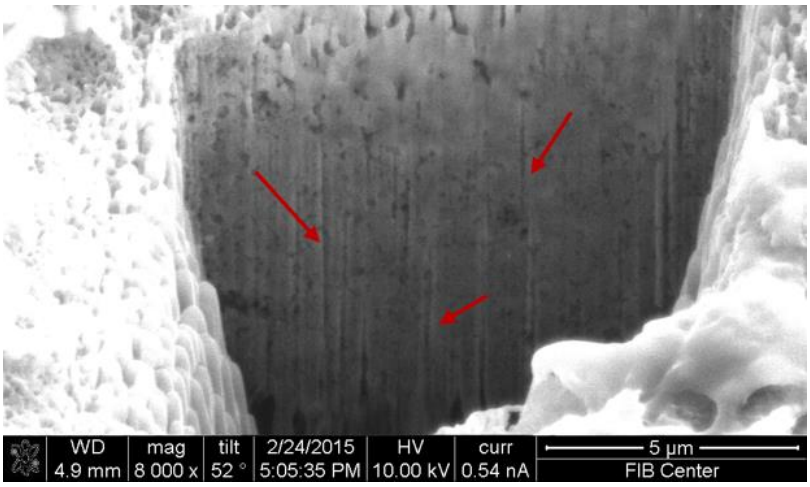

Figure 9 – Example of the "curtaining" effect. Red arrows point to vertical lines, false features of the microstructure introduced by application of an excessive ion beam, not present in the material before ion milling.

An example of a cathode viewed in profile following the application of various ion beam parameters is shown in Figure 11.

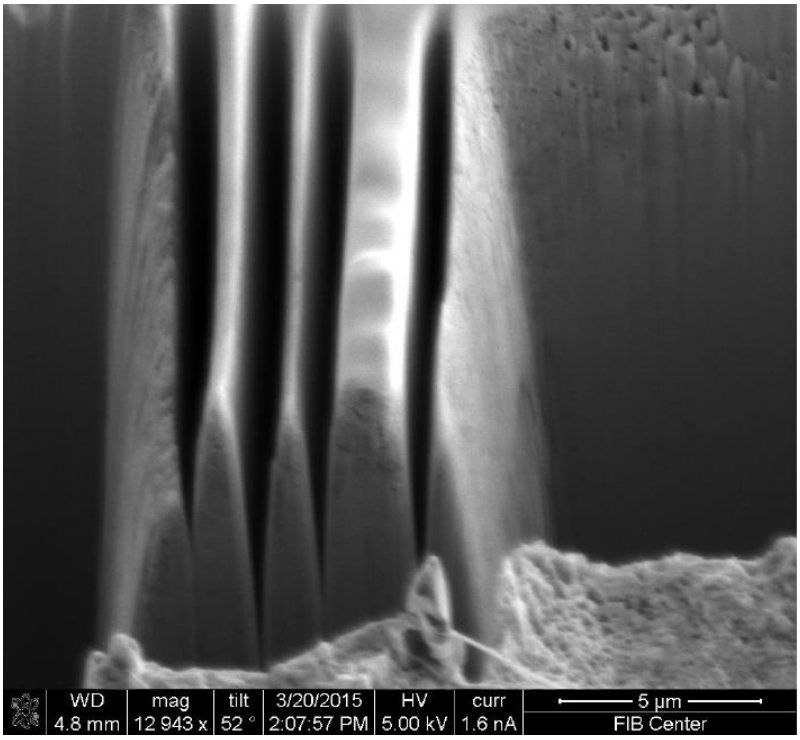

Figure 10 – Cross-sectional profile of remaining material after milling with varying ion beam accelerating voltages.

Noting the shapes of remaining material portions following milling, it was apparent that the choice of beam parameters significantly influenced the shape and fidelity of the ROI and the to-be-imaged surface. Our workup indicated that higher ion beam accelerating voltage resulted in "cleaner" slicing (surface removal) with curtaining sufficiently reduced as to ensure a large ROI area acceptable for imaging. At higher ion beam currents with fluence kept equal, imaged surfaces became obscured by artifact, as was anticipated. This obscuring was due to a combination of ionomer overheating beyond the glass transition temperature, which would lead to ionomer flow (rearrangement), implantation of gallium material originating from the primary ion beam, and sample (cathode) material sputtering and redeposition in to the ROI. The optimal ion beam current was determined empirically by reducing current until the features of a surface cross-section were unobscured as

compared to a cross-section milled using the lowest stable beam current on the tool. This current was reduced to ~40 pA when features appeared equal to the lowest stable current. Still, to ensure the best possible accuracy, a 10 pA ion beam current was used to minimize all possible artifact introduced by the ion beam. This resulted in longer data collection times; however, for the downstream applications of the FIB-SEM data in this thesis, accuracy was deemed more important than the loss of time. Fluence was minimized such that the ion beam was applied no longer than the time required to remove a surface from the field of view. This helped to minimize unnecessary gallium implantation in the ROI. In practice, each slice required around two minutes to mill. Related research indicates that at 10 pA beam current, local temperature in the sample will only rise a few degrees Celsius from ambient temperature, assuming the effective heat transfer coefficient of the cathode layer was not orders of magnitude less than estimates by other researchers.[37,38] Moreover, Osborn et al. showed that the glass transition temperature of Nafion® occurs around 100˚ C and is therefore essentially immune to flow at the temperatures experienced during ion milling at the currents used in this work.[39] In some cases, the electron beam can cause insulating materials to "jump" or accelerate across the field of view due to Coulomb forcing. This was empirically circumvented by taking an image at very low electron beam current such that no jumping, occurred then progressively increasing current until material moved. In practice, the range of SEM accelerating voltages and beam currents used never induced artifact into any of the cathode samples tested. Our results were corroborated by a landmark study investigating the extent of FIB-SEM damage on PEMFC samples at Brookhaven National Laboratory. The study compared FIB-SEM tomographic images to synchrotron-based x-ray tomographic images and found that no appreciable mesoscopic

structural rearrangement of PEMFC cathode layers took place upon imaging when milling at ion beam parameters of 30 kV and 40 pA [cite this study].

A platinum protective square was applied atop the ROI to further prevent beam artifice during set up and preparation of the ROI. The slicing thickness used throughout this work was nominally specified at 20 nm and verified using a diagonal fiducial across the top of the platinum protective square. The diagonal fiducial was a nanometer-depth milled diagonal line from corner to opposite corner of the platinum protective square. Because depth parallel to the electron beam is difficult to "see" in an SEM, the diagonal line served as a mapping or "ruler" of the depth dimension into the lateral dimension for easy determination of ROI depth while progressive through images in a volume. In Figure 12, a red arrow points to the diagonal fiducial in a cross-sectional image taken slightly more than half-way through a ROI volume.

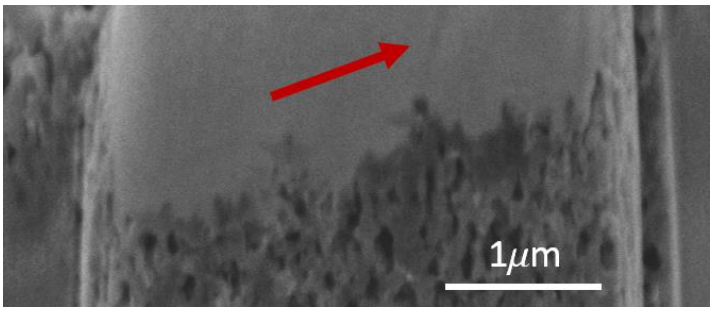

Figure 11 – Example of a diagonal fiducial line seen milled into the platinum protective square at the top of an interior cross-section in a FIB-SEM image.

2.2.2 Digital Component

FIB-SEM tomography requires registration, interpolation, and segmentation of the image stack generated. Registration and interpolation were straightforward. Registration,

the process of aligning images relative to one another, of PEMFC cathodes was straightforward and of minimal concern when satisfactory fiducial markers were used. If a sufficiently large field of view is used during SEM imaging, the ROI itself may suffice as an adequate fiducial for registration. One example of this can be seen in Figure 12 and another, more clearly, in Figure 17, presented in section 2.3. Registration was accomplished utilizing existing translational and rotational transformation algorithms via StackReg and TurboReg plugins implemented in the National Institutes of Health-developed FIJI image processing software.[40] In a few cases, minor manual corrections were applied to ensure the best possible accuracy. Linear interpolation between images in the stack was used in this thesis.

Segmentation was more challenging and remains an important problem for future research in PEMFC cathode tomography. Indeed, automated segmentation of images remains a significant problem across many fields, especially medical imaging and computer vision for artificial intelligence. For PEMFC cathode FIB-SEM, a resultant image stack may typically span 100 – 300 images with approximately 10^6 – 10^7 pixels per image amounting to as many as or more than 10^9 total pixels requiring segmentation per tomogram, an obviously unreasonable task for a person to attempt. This obliges reliance on algorithmic processing. The most significant challenge of cathode segmentation is the so-called "shine-through" effect. Shine-through describes the difficulty of segmenting highly porous materials. Material just behind the imaged plane may appear bright enough under the influence of the electron beam as to confuse algorithms into assigning a pixel as solid phase in the imaged plane that should be assigned as pore phase in the imaged plane

and solid phase in the *subsequent* image. This is graphically depicted in Figure 13 with a question mark indicating difficulty in choice of segmentation algorithm.

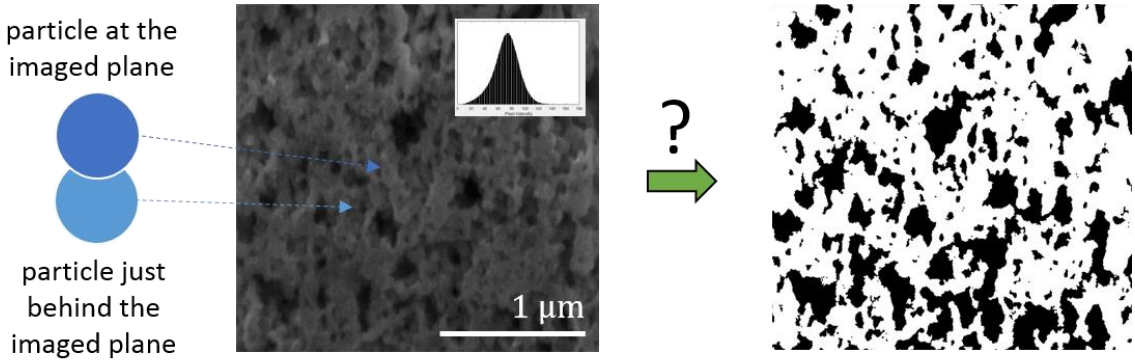

Figure 12 - Graphical depiction of "Shine-through"and how it may result in erroneous image segmentation.

Prill et al. undertook the most rigorous attempt to the best of our knowledge in PEMFC cathode segmentation.[41,42] They simulated the electron collision cascade of a 5 keV electron beam on a digitally generated volume of carbon spheres and determined the resultant secondary electron signal that would be detected. This resulted in a nearly ground truth set of images which were then used in a search for an accurate segmentation algorithm. They found that morphological filters and a watershed segmentation algorithm resulted in single-digit error when applied to the whole set of their ground truth images. In two papers, Salzer et al. later quantified the downstream consequences of error associated with FIB-SEM demonstrating that accurate segmentation of the microstructure significantly influences downstream calculations utilizing the segmented FIB-SEM data.[43,44]

We tested and compared various simple combinations of common filters and segmentation algorithms, a method similar to the method of Prill et al., and a human-

computer interactive method, which was ultimately used as it provided the best results on our images. Particularly, because we did not have access to any ground-truth images, we relied more on the ability of the human brain to interpret correctness of segmentation around complex features prone to incorrect segmentation by shine-through artifacts.

Segmentation was accomplished by an interactive segmentation approach relying on a Sauvola local segmentation algorithm implemented using MATLAB's Image Processing Toolbox.[45] The Sauvola criterion is given in Equation 2-1.

$$T_{px} > m_{px} \cdot \left[1 + k_{px}\left(\frac{s_{px}}{r_{px}} - 1\right)\right] \tag{2-1}$$

T_{px} was a pixel's classified phase and was assigned pore phase if the inequality evaluated true and solid if the inequality evaluated false for each pixel, m_{px} was the mean value of the local segmentation neighborhood, s_{px} was the standard deviation of the values in the local segmentation neighborhood, and k_{px} and r_{px} were parameters that were independently chosen for each tomogram.[46] A small program was written to rapidly identify error-prone regions where shine-through artifacts were present, display these regions of the original images with segmented images overlain, and provide the option to vary the segmentation parameters k_{px} and r_{px}. Segmented images overlaid upon original images were inspected and parameters were rapidly varied until the segmented images were judged to most accurately represent the high porosity microstructure with minimal pixel misclassification rate. Interactive segmentation workflows such as this are increasingly utilized in medical imaging segmentation, an area in which tolerance for false positives and/or false negatives is practically zero.[47] In this way, the benefits of both the

speed of a computer and the interpretive ability of a human brain were both utilized to great extent.

2.3 FIB-SEM Developments for Corroded Cathodes

The need for the developments described in this subsection arose in response to collection of our first corroded samples. Using identical methodology, beginning of life samples were imaged with high fidelity; however, highly corroded cathodes exhibited a significantly increased charging effect to the point that downstream image segmentation was made unreliable. The well-known charging effect implied insufficient electron conductivity of the sample,[48] however, initially, nothing about the FIB-SEM procedure was changed between imaging pristine and corroded samples. It is important to note that imaging an as-fabricated catalyst coated membrane meant that FIB-SEM was performed on cathodes that were electrically floating atop the insulating PEM such that electron conduction to ground took place in the plane of the cathode layer as depicted in Figure 14. Mitigating the charging effect also minimizes and mitigates the possibility for electromechanical drift which can further complicate downstream image processing.

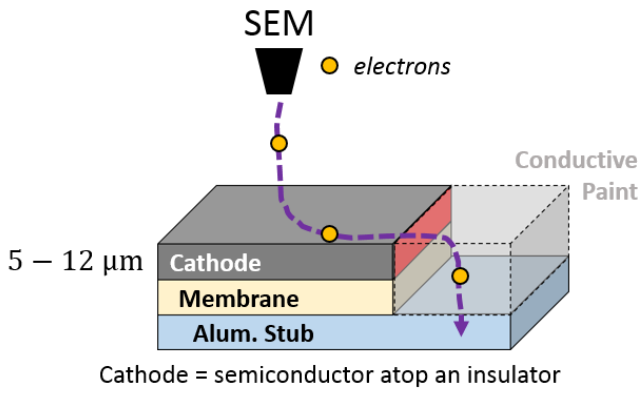

Figure 13 - Diagram of electron conduction path and the charge flux area (red). Electrons must travel in the plane of the cathode, through conductive paint applied, and finally into the aluminum sample stub to reach ground.

Loss of in-plane electronic conductivity then must have been the cause of charging following corrosion. This was assumed caused by the reduction of the charge flux area required to dissipate all the charge not emitted as secondary signal; cathodes are known to thin in the through-plane direction following corrosion thereby reducing the charge flux area [cite Reimer 2006]. Moreover, corrosion often results in a decrease in the carbon/ionomer fraction, which would decrease the effective (composite) electronic conductivity of the cathode layer, although the specific connectivity of the carbon and ionomer could to lead to local heterogeneities that are difficult to probe.

To reduce the charging effect observed in corroded samples, precise control of colloidal silver conductive paint was used to ensure the most facile dissipation of charge. This amounted to a version of the "coffee ring" problem that arises in drying of colloidal suspensions, particularly droplets [cite two]. In the coffee ring problem, the competition between capillary and Marangoni forces in a colloidal droplet determine where solid colloidal particles ultimately deposit, radially, as solvent evaporates. Through colloidal

silver paint droplet size control and accelerating the drying time through application of a perpendicular stream of air, we were able to adequately, albeit crudely, direct the deposition of silver to create high silver concentration “bridges” between the ROI and copper tape connected to the sample stub. In some cases, an additional platinum grounding strap was used to connect the ROI to the silver paint. This resulted in the highest possible electrical conductivity bridge from the ROI to ground. In Figure 15 an example of the cathode/Ag-paste interface is shown as a dashed red line above which, an example of a high and low Ag concentration regions, as confirmed by EDS, are shown.

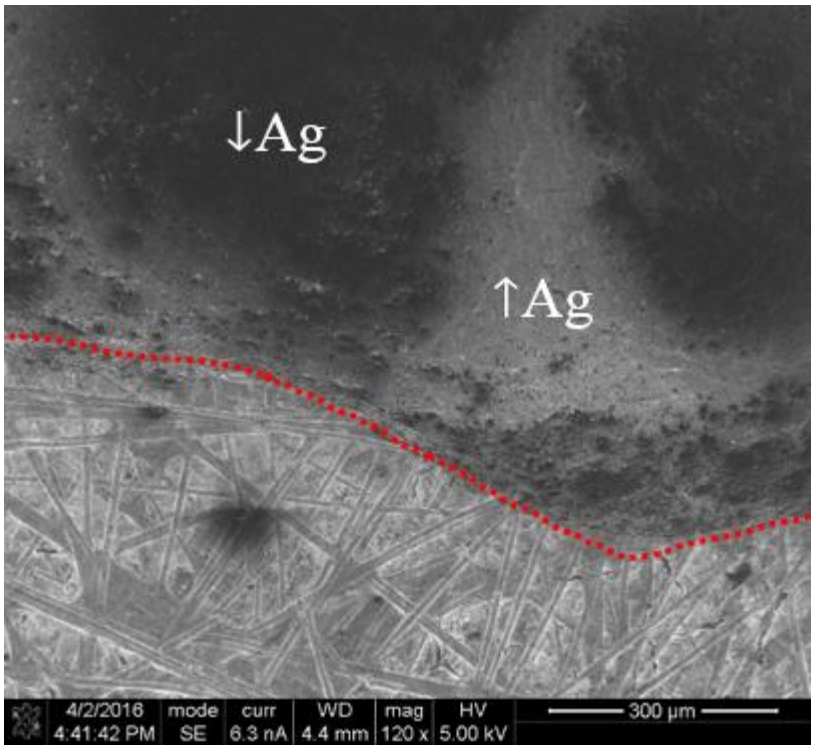

Figure 14 - Example of high and low Ag concentration regions demonstrating the ability to control local Ag concentration and create the best electron conduction paths to facilitate charge dissipation. Ag paste is above the dashed red line, the cathode sample is below it.

Figure 16 depicts the in-lab sample preparation of the cathode samples. In this graphic, VOI abbreviates “volume of interest” used synonymously with ROI in this thesis.

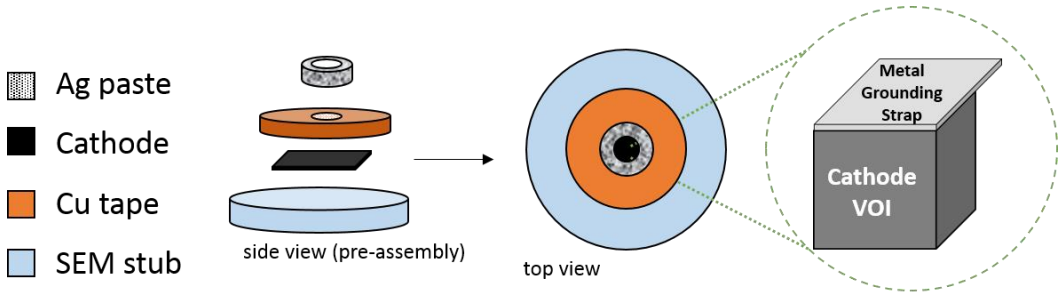

Figure 15 – Cathode sample in-lab praration depiction. Silver paste provides additional electrical connection from the cathode sample through the copper tape and ultimately to ground. In some cases, a grounding strap connected the VOI to the silver paint.

In Fig. 17, an example of an interior slice from a set of tomographic images of a highly corroded sample using the optimized methodology is shown demonstrating that charging was acceptably reduced. Reducing the charging effect was critical because it allowed for the use of both a higher electron beam accelerating voltage and current to be used. These in turn increased brightness and image resolution, without charging, which increased the reliability and success rate of downstream image processing.

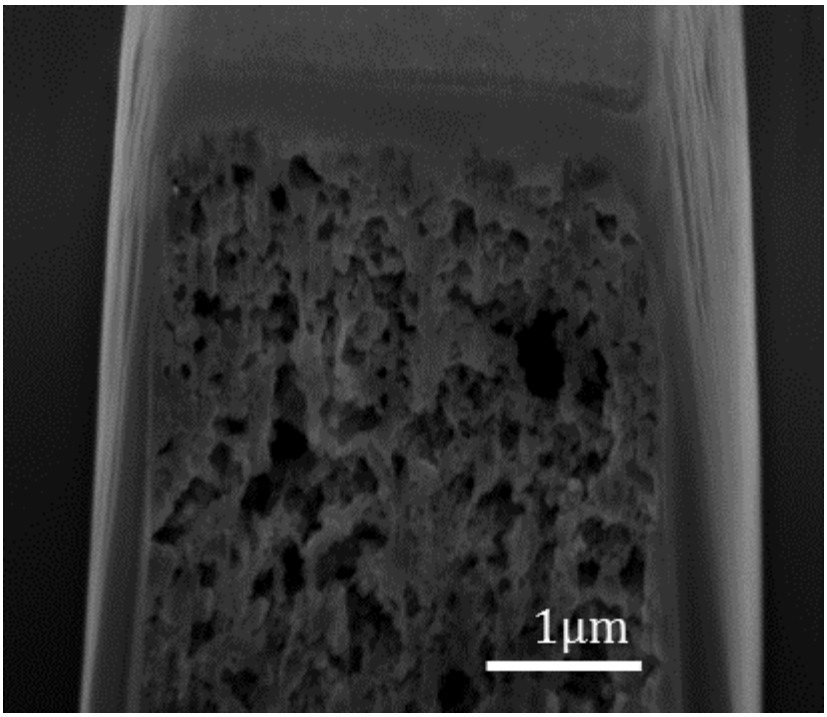

Figure 16 - Example of interior cross section with charging acceptably reduced to ensure accurate segmentation in image processing.

CHAPTER 3. INVESTIGATING MICROSTRUCTURAL COLLAPSE IN N_2 ENVIRONMENT

Extensive corrosion has been shown to result in collapse of the porous cathode microstructure in PEMFCs and has been presumed responsible for severe mass-transport voltage losses observed in polarization data. In this project, corrosion of the carbon support was studied by electrochemical methods, non-dispersive infrared spectroscopy, and FIB-SEM tomography to evaluate the connected roles of carbon loss, microstructure, and performance degradation. *In silico* characterization of the three-dimensional, digital microstructures generated by FIB-SEM included porosity, short-path tortuosity, and two-point correlation functions before and after corrosion. Carbon loss and H_2/air *operando* performance decay were strongly correlated but contrary to expectation, the associated porosity loss and tortuosity gain did not explain the observed performance decay; cell failure occurred long before microstructural collapse was observed. Platinum catalyst ripening as well as the preferential corrosion of the amorphous interior of carbon black primary particles were likely the two predominant degradation mechanisms induced among the cells tested. These results connect and clarify the roles of performance, microstructure, and corrosion degradation and demonstrate that microstructural collapse need not underlie cell failure.

3.1 Motivation

In this project, a FIB-SEM tomographic method was applied to several corroded PEMFC cathodes to better understand and quantify the relationship between

microstructural changes and performance degradation caused by corrosion. Many authors have demonstrated that extensive corrosion of the cathode layer leads to thinning and porosity loss.[10,49,50] Taken together, these changes constitute collapse of the porous electrode microstructure which degrade cell performance by hindering facile species transport to and from catalyst sites. Fuel cells were exposed to accelerated stress tests (AST) to induce electrochemical corrosion of the cathode catalyst support while cathode effluent was monitored by an online, non-dispersive infrared spectrometer. Post-mortem FIB-SEM, cathode thickness measurements, and *in silico* characterization of the digital representations of the microstructure were carried out to determine transport parameters and characteristics that underlie fuel-cell performance and durability.

3.2 Experimental Methods

3.2.1 Materials

Ion Power NR-212 catalyst coated membranes with 0.3 mg_{Pt}/cm^2 were used in all experiments. TGP-H-060 Toray carbon paper with 5% wet proofing was used as gas diffusion media (Fuel Cell Store). 127 μm (5 mil nominal) PTFE was die-cut and used as gasket material (McMaster-Carr). Cells were assembled in 25 cm^2 single cell hardware with triple serpentine Poco graphite flow fields (Fuel Cell Technologies). The hardware was joined by eight bolts that were fastened by torque wrench set to 4.0 Nm. Cells were tested using a Scribner 850e fuel-cell test system with an 880 frequency response analyzer and a Metrohm Autolab 302N potentiostat/galvanostat. CO_2 was detected with a California Analytical Instruments 601 non-dispersive infrared detector (NDIR). Thermogravimetric analysis (TGA) was performed on a TGA Q50 (TA instruments). FIB-SEM was performed

on an FEI Nova Nanolab 200 maintained by the Institute for Electronics and Nanotechnology at the Georgia Institute of Technology.

3.2.2 Electrochemical Characterization

H2/air polarization curves, H2/air electrochemical impedance spectroscopy (EIS), and H2/N2 voltammetry were employed for characterization and benchmarking of fuel-cell performance. Specific cell conditions are noted with the data and presented in the Results section. Cells were "wet-up" and broken in by sixty cycles of alternating between OCV, 0.6 V, and 0.2 V for one minute each. Shortened break-in protocols, ten cycles of the same procedure, were applied after corrosion accelerated stress testing but before post-corrosion characterization to ensure observed losses were not "recoverable" losses[8]. Polarization curves were measured following fifteen-minute holds at 0.2 V then the current was scanned toward open circuit voltage at 0.15 A/s. This method was fully reproducible and slower (0.1 A/s and 0.05 A/s) scan rates showed no appreciable difference. In this thesis, the electrode receiving air during galvanic operation will always be referred to as the cathode. The "beginning of life" (BOL) state of each fuel cell was assessed immediately after wet-up and break-in but with no further use. The "end of test" (EOT) state was assessed after a given corrosion protocol and after the additional shortened break-in procedure was applied. Tafel slopes and exchange-current densities were extracted from the low current density region of these polarization curves. Ohmic losses were determined separately by current interrupt and EIS and were found unchanged before and after AST. H2/air EIS spectra were preceded by a brief potential hold at 0.2 V followed by a fifteen-minute hold at the steady-state current density. The impedance response was measured from 10 kHz – 10 mHz with 5% of DC current as perturbation. To determine

electrochemical surface area (ECSA), a procedure outlined by Abbou et al. was used: cell potential was swept from 0.1 V up to 0.8 V then back to 0.1 V three times at 50 mV/s while H_2/N_2 at 0.1 SLPM/0.15 SLPM and 75% relative humidity (RH) were delivered to the cell[51]. For all samples, the second and third sweeps were identical and the third sweep was used to calculate electrochemical surface area by hydrogen adsorption-related charge passed[52].

Cell data was highly reproducible due to the use of precision-manufactured CCMs purchased from Ion Power. Plots of Tafel slopes in Figure 17 and ohmic overpotential in Figure 18 for multiple cells demonstrate reproducibility between cells.

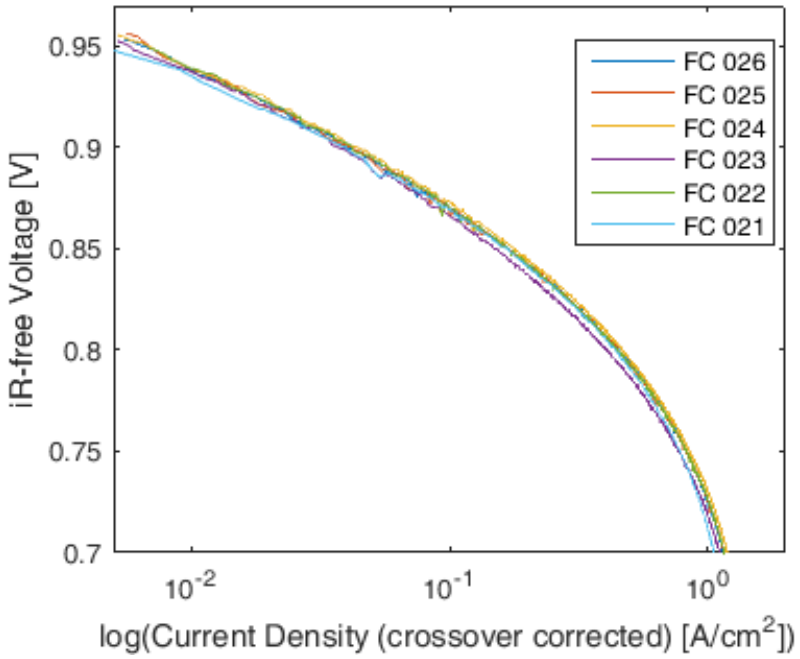

Figure 17 – Plots of Tafel slopes for multiple cells demonstrating excellent reproducibility among cells.

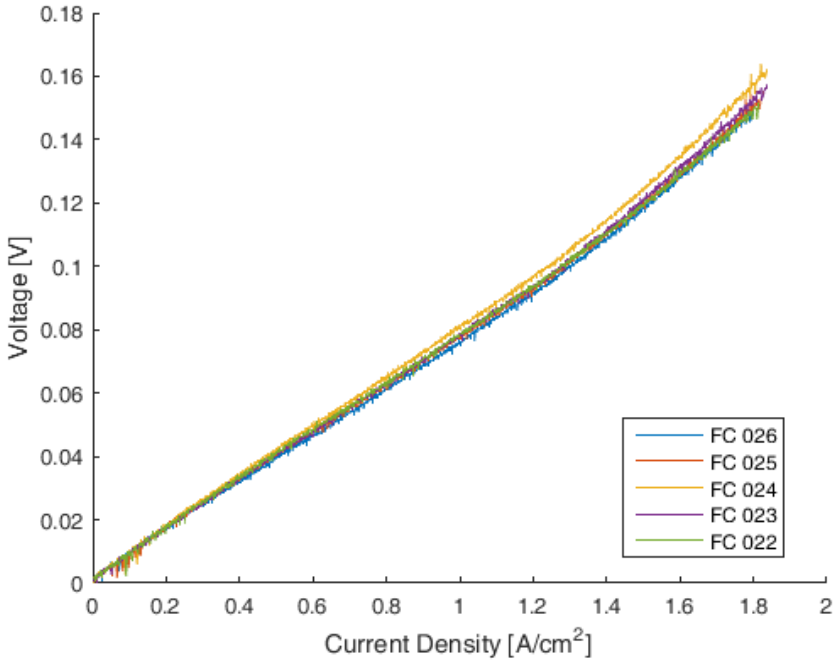

Figure 18 - Ohmic overpotential versus current density for multiple cells demonstrating excellent reproducibility among cells.

3.2.3 FIB-SEM

Following disassembly of the fuel cell, the gas diffusion layer was removed from MEA samples and MEAs were dried at 25 °C for at least sixteen hours. Fast drying silver suspension (Ted Pella) and copper tape (3M) were used to affix approximately 2 mm × 2 mm MEA samples to an SEM stub. The silver suspension was dried under forced air for ten minutes then the affixed samples were placed under coarse vacuum (-70 kPa gauge) for at least four hours. Samples were taken from the ~1 cm^2 portion of the 25 cm^2 cathode active area shown in green in Figure 19. All post-mortem tests were performed on these regions of corroded samples.

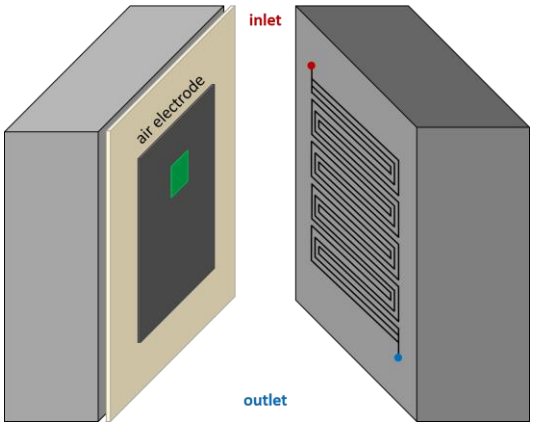

Figure 19 - Post-mortem samples were taken from the ~1 cm2 green region of the active area.

After sample preparation, samples were transferred to the FIB-SEM chamber and left until chamber pressure reached at least 6×10^{-6} Torr. FIB-SEM region of interest (ROI) site selection was chosen to approach the conductive silver paint as closely as possible. In practice, roughly ten to twenty microns separated the ROI from the silver paint. A platinum square deposited by gallium ion-initiated organoplatinum cracking at 30kV, 30 pA protected the ROI and a platinum grounding strap connected the ROI to the silver paint to prevent disruption of the region of interest and ensure the most facile possible dissipation of charge and heat. SEM parameters were 4 kV and 1.6 nA. FIB parameters were 30 kV and 10 pA with nominal slice thickness specified at 20 nm and verified by fiducials.

Each pixel in a 2D image represented 3 nm × 2 nm of cathode area. The total FIB-SEM volumes sampled and number of slices per sample are listed in Table 2.

Table 1 - Sampled volume and number of slices for each FIB-SEM sample.

FC #	BOL	BOL	BOL	5	6	6	6	7	7	8	8
Volume [μm^3]	13	7	4	5	9	10	5	10	4	15	7
# Slices	174	147	146	146	152	165	155	137	90	244	154

3.2.4 Cathode Thickness Measurements

Cathode samples of ~1 mm^2 were taken from the ~1 cm^2 portion of the cathode active area shown in green in Figure 1, prepared by liquid nitrogen freeze fracture, and imaged via SEM. Dozens of thickness measurements were taken at multiple locations

along the imaged length of cathode. These measurements were averaged and the mean was regarded as the cathode thickness.

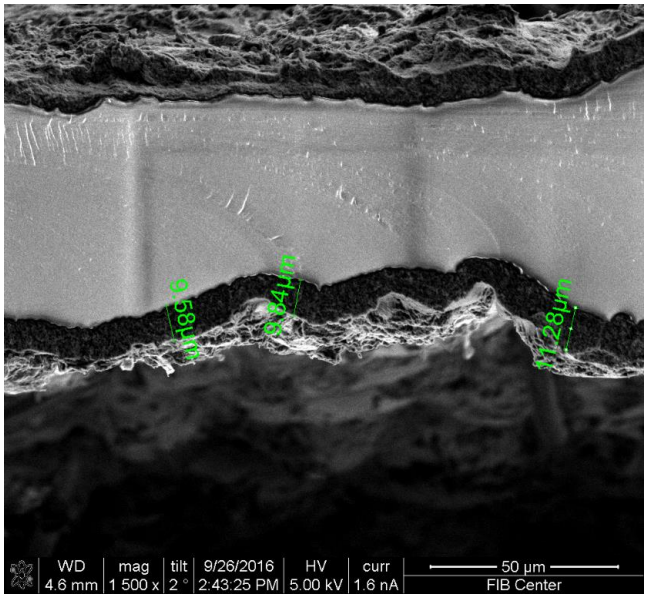

Figure 20 - Example of a cathode thickness measruement prepared by LN_2 freeze fracture and imaged by SEM.

3.2.5 In silico Characterization

Porosity distributions were calculated as the ratio of void voxels to total voxels in an ij plane through the k-direction where i, j, k are Cartesian dimensions and mean porosity was the mean of the distribution,

$$\varepsilon_k = \frac{n_k}{N_k} \quad \text{and} \quad \bar{\varepsilon} = \frac{1}{k_T}\sum_{k=1}^{k_T} \varepsilon_k \ . \tag{3-1}$$

In Equations (3-1), n_k is the number of void voxels in the k^{th} ij-plane, N_k is the total number of voxels in the k^{th} ij-plane, and k_T is total number of ij-planes.

Tortuosity is generally understood as the ratio of the path distance a fluid parcel travels through porous media to the path distance that parcel would travel through the corresponding unimpeded ($\varepsilon = 1$) distance[53]. One mathematical definition, labeled average Dijkstra tortuosity, $\bar{\tau}_{Dijk}$, in this project, was built upon the ratio between the Dijkstra distance (minimum traversable path distance) and the Euclidean distance between two points in the microstructure[54].

The Dijkstra and Euclidean distances were both calculated from a starting point nearest the GDL/cathode interface to all other points in the digital representation of the cathode. The result was $N_T - 1$ Dijkstra/Euclidean distance ratios where N_T is the total number of voxels in the digital microstructure. These ratios were averaged to obtain a single value for each microstructure,

$$\bar{\tau}_{Dijk} = \frac{1}{N_T - 1} \sum_{p=1}^{N_T - 1} \left(\frac{L_{Dijkstra}}{L_{Euclidean}} \right)_p \quad . \tag{3-2}$$

The advantage of this calculation was that it sampled short, tortuous paths throughout the entire digital cathode volume, not only a single short path from one point to another point. In this way, inherent heterogeneity of the microstructure was sampled which ensured that $\bar{\tau}_{Dijk}$was representative of the entire sampled volume. Importantly, this collapses pathing information from the entire microstructure into a single, scalar parameter.

n-point correlation functions provide information about the microstructure of heterogeneous media and were used to help understand and quantify the degree to which inter-particle collapse and/or expansion occurs during corrosion. Torquato[55] provides an extended mathematical treatment of the canonical *n*-point correlation functions. Briefly, the one-point function provides the porosity of the sample; the two-point correlation function is the probability that the endpoints of a randomly sampled vector of norm r will both fall into phase p and is a statistical measure for characterizing short-range order in random media. Two-point correlation functions, $S_2(r)$, were calculated by a Monte Carlo method in which each vector norm, r, was sampled $>10^6$ times. To probe longer-range ordering effects, two-point cluster functions, $C_2(r)$, were calculated by a similar Monte Carlo method. $C_2(r)$ can be thought of as special case of $S_2(r)$, whereby the sampled vector falls both in the same phase *and* the same cluster (a *connected* region of the relevant phase).

3.3 Results and Discussion

The corrosion-performance landscape was surveyed by a series of corrosion protocols including potential holds and square-wave cycling as shown in Table 2. Additional cells were tested to help estimate the expected polarization losses as a function of accelerated stress testing but do not contribute importantly to the results in this chapter. Potential holds are designated by the duration of the hold and the value of the elevated potential. Cycling is designated by the number of cycles, the upper and lower potential limits (UPL/LPL), and the time spent at each potential, in parentheses. AST protocols were chosen to reflect and investigate a range of pertinent conditions including the influence of

UPL, LPL, time, and cycling vs. holds within reasonable proximity to the standardized corrosion protocols recommended by the DOE[56].

Table 2 - Fuel cell corrosion protocols tested and corresponding total carbon loss. Electrochemical data is presented below for FC 1 – 8 and FIBSEM data is presented below for FC 5 – 8.

Fuel Cell	Corrosion Protocol	Carbon Loss ($\mu g/cm^2$)	Carbon Loss (%)
1	100 cycles 0.1 V (30s) - 1.25 V (30s)	66	22
2	18 hours 1.2 V hold	54	18
3	1500 cycles 0.1 V (3s) - 1.3 V (3s)	95	32
4	3000 cycles 0.1 V (3s) - 1.3 V (3s)	111	37
5	**500 cycles 0.4 V (3s) - 1.3 V (3s)**	**42**	14
6	**1500 cycles 0.4 V (3s) - 1.3 V (3s)**	**87**	29
7	**2500 cycles 0.4 V (3s) - 1.3 V (3s)**	**102**	34
8	**4000 cycles 0.4 V (3s) - 1.3 V (3s)**	**130**	43
11	24 hours 1.3 V hold	186	62

An essential Department of Energy (DOE) technical target for cell failure is a 10% voltage loss in the 1.0 – 1.5 A/cm^2 region of the polarization curve[56]. At high current densities, this test was developed specifically to address the problem of mass-transfer related voltage losses. EOT polarization curves are shown for the >1.0 A/cm^2 region in Figure 3.

Data were measured at T_{cell} = 70° C, 0.5 LPM H_2 (75% RH), and 1.5 LPM air (75% RH). A composite curve representing the BOL performance and a red curve representing the DOE durability target are also shown. FIB-SEM data was collected only for FC 5-8 and BOL samples. Individual BOL polarization curves that comprise the BOL composite are shown in Figure 21.

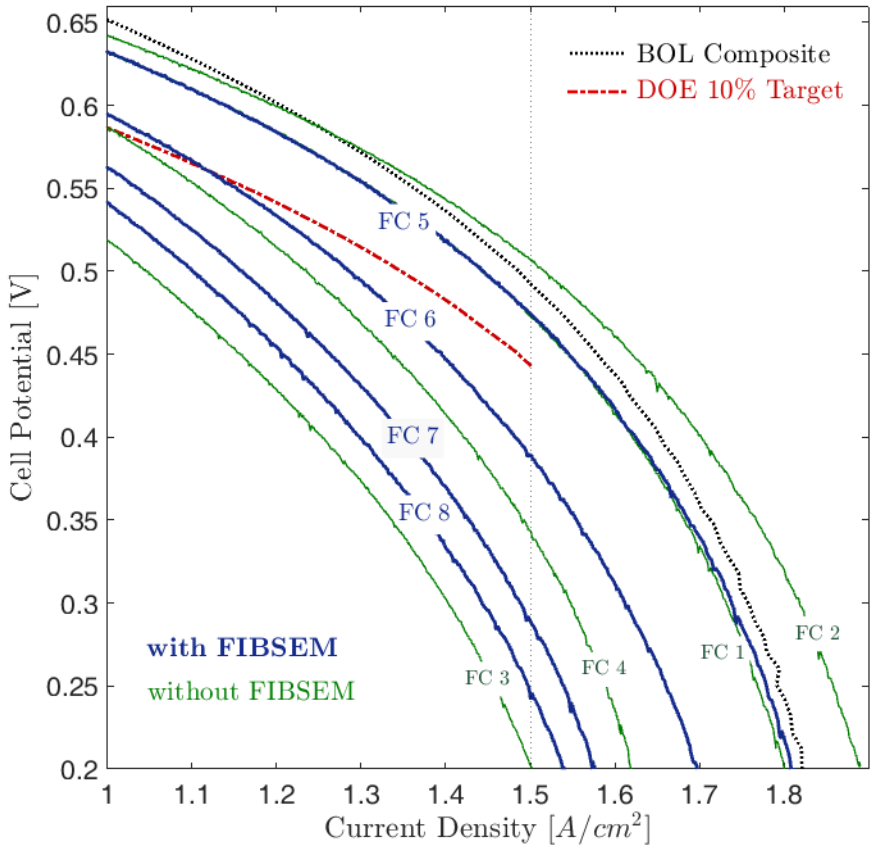

Figure 21 - EOT polarization curves, the BOL composite, and the DOE 10% voltage loss from BOL failure target. Cell conditions were Tcell = 70° C, 0.5 LPM H2 (75% RH), and 1.5 LPM air (75% RH).

Carbon loss was a good but imperfect predictor of polarization curve performance degradation in the >1.0 A/cm^2 region. Performance in this region decayed monotonically with carbon loss for FCs 1, 3, 4, 5, 6, and 7. Notably, limiting current for FC 2 *increased* after corrosion and the performance of FC 4 degraded more than FC 8 despite the greater

carbon loss by FC 8. However, FC 4 was exposed to 0.1 V LPL compared to 0.4 V LPL for FC 8 and lost a greater fraction of ECSA from BOL to EOT despite undergoing fewer AST cycles.

To clarify the relationship between corrosion and performance degradation, FC 5-8 were compared at the microstructural level. These cells underwent an identical corrosion cycling procedure but with varying number of cycles applied. Cathode microstructural collapse has been observed following extensive carbon corrosion and has been implicated for severe mass-transport voltage losses observed in aged cells[14]; however, the evolution of this collapse is not well understood. Collapse is a colloquial term for porosity loss that has a profound effect on transport phenomena in porous media and thus, cell performance. One may write an equation for cathode porosity,[57]

$$\bar{\varepsilon}_{MB} = 1 - \left(\frac{1}{\rho_{Pt}} + \frac{R_{C/Pt}}{\rho_C} + \frac{R_{C/Pt}R_{I/C}}{\rho_I}\right)\frac{m_{Pt}}{L}\ , \tag{3-3}$$

in which ρ_i is the mass density of species i, $R_{i/j}$ is the mass ratio of species i to j, m_{Pt} is platinum mass loading, L is cathode thickness, and $\bar{\varepsilon}_{MB}$ is porosity by this approach, herein labeled "porosity by mass balance." Equation (4) describes pristine cathodes and corroded cathodes with small variation in carbon mass density relative to carbon loss, negligible fluorine mass loss relative to initial fluorine mass, and majority retention of platinum within the cathode. The result is a realizable porosity surface, $\varepsilon = f(\Delta m_C, L_{cathode})$, with porosity as a function of carbon loss and cathode thickness. The corrosion history of a cathode thereby maps a path or trajectory on the realizable porosity surface. A path may cross an equiporosity curve one or more times; *i.e.*, the cathode may hollow *then* collapse

or collapse *then* hollow as it corrodes. Although simplified, this approach requires only initial cathode parameters and two simple measurements for corroded samples, carbon loss and cathode thickness.

In Figure 22, porosity results are plotted as functions of carbon lost by both FIB-SEM and mass balance approaches. FIB-SEM was performed one or more times on each corroded sample to ensure reasonable reproducibility of the methodology. Parameters used in the mass balance approach are listed in Table 3: manufacturer reporting and TGA confirmation determined BOL mass ratios, EOT cathode thicknesses were measured by SEM after freeze fracture and EOT carbon mass loss was determined by NDIR. Densities assumed for platinum, carbon, and ionomer were 21 g/cm^3, 1.8 g/cm^3, and 1.9 g/cm^3, respectively[58]. Platinum loading was assumed constant at 0.3 mg/cm^2 as an N_2 (O_2-free) environment suppresses platinum-into-membrane migration during corrosion AST[59]. Furthermore, the choice of N_2 environment, thick membranes (50 μm), and 0.4 V as LPL indicate that hydrogen peroxide formation will remain negligibly low thereby preventing severe fluoride release via radical attack of the ionomer[60]. The lines serve as a visual to emphasize the non-monotonic porosity variation. Porosity distributions in the through plane direction were also examined. Although small local variations arose, no appreciable through-plane porosity gradient was observed in any of the samples tested.

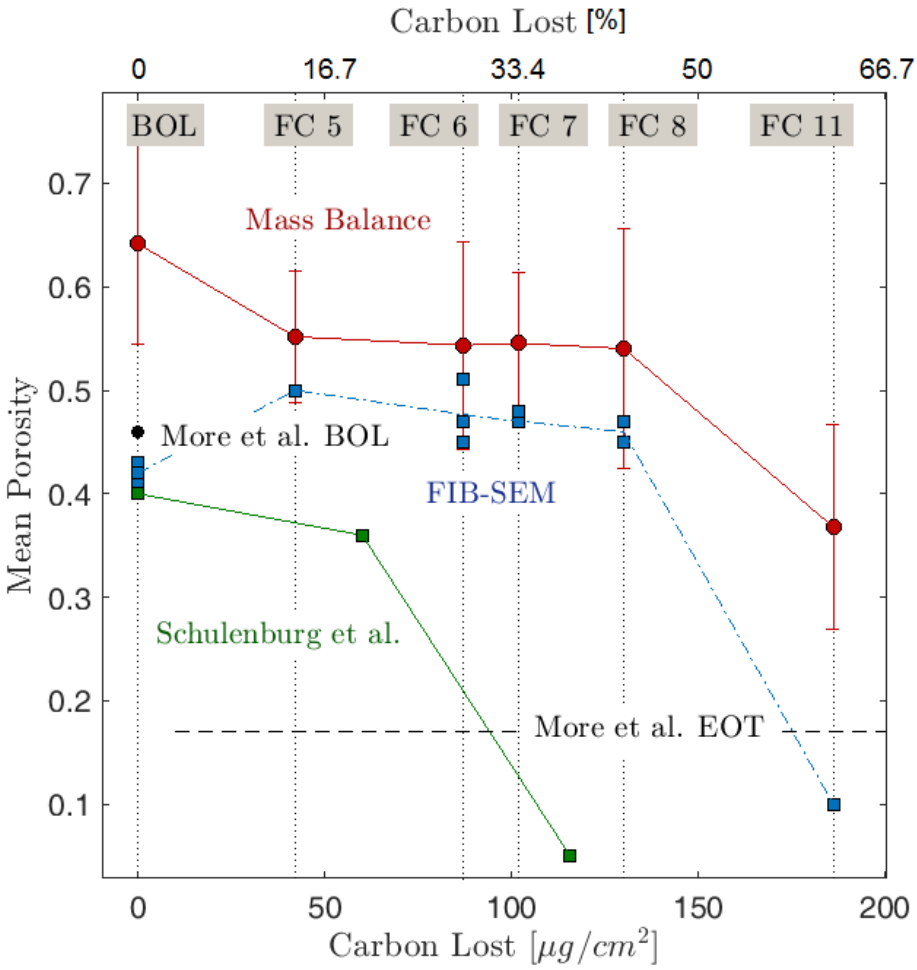

Figure 22 - Porosity vs. carbon lost after ASTs determined by FIB-SEM and mass balance approaches. The BOL FIB-SEM data includes an arrow and (2x) which indicate that two data coincidentally overlap.

Porosity, as measured by FIB-SEM, appeared to increase from BOL to FC 5 then decrease slightly between FC 5 and FC 8 before ultimately, a more substantial "collapse" event was observed. Excluding FC 11, the porosity range was only 14% and negligible anisotropy was observed in the through-plane (GDL/cathode interface → cathode/membrane interface) porosity distributions. The mass balance approach resulted in a 14% reduction in porosity from BOL to FC 5 due to the significant loss in cathode thickness measured between these two samples. Cathode thickness decreases were small

between FC 5-8 which resulted in an apparent constant porosity due to countervailing carbon mass loss and cathode thickness loss. Ultimately, although by a different AST, extensive corrosion led to severe porosity loss (FC 11) which has been observed by other authors[50,27]; in a similar study, Schulenburg et al. measured BOL porosity, EOT porosity, and carbon loss by FIB-SEM. More et al. measured BOL and EOT porosity by STEM imaging but did not report carbon loss. As such, More's EOT porosity is displayed as a dashed line in Figure 22 to indicate the certainty regarding eventual microstructural collapse but uncertainty in the carbon loss required to induce the collapse. FIB-SEM error bars were not included due to the difficult nature of exactly quantifying the error by FIB-SEM however, an estimate of the error can be made. Melo et al. demonstrated that a 30 kV, 40 pA Ga^+ ion beam may induce chemical changes in the ionomer and amorphization of carbon crystal structures but spatial rearrangement of material at the length scales of interest in this work was not observed[61]. Moreover, the present work utilized a 30 kV, 10 pA Ga^+ ion beam which further mitigated potential sample damage compared to the experiments conducted by Melo et al. To the best of our knowledge, Salzer et al. are the only group to have validated PEMFC cathode segmentation algorithms for images of real cathodes against simulated ground truth images[44]. They reported a 9.6% mean error in pixel classification using a global thresholding method which they found had similar success to a Sauvola method, as was applied in this work. However, their method did not utilize human intervention and was therefore possibly less accurate than the method used in this work. This gives some idea of the error involved in the FIB-SEM method, both physical and digital.

Table 3 – Parameters used for mass balance porosity calculation based on beginning of life thickness and TGA measurements, carbon mass loss detection during AST, and post-mortem thickness measurements

Sample	C Loss [μg/cm^2]	C Loss [%]	$R_{C/Pt}$	$R_{I/C}$	$L_{cathode}$ [μm]
BOL	0	0	1.0	1.3	9.2 (σ = 1.4)
FC 5 (500 cycles)	42	14	0.9	1.6	7.0 (σ = 0.8)
FC 6 (1500 cycles)	87	29	0.7	1.9	6.5 (σ = 1.2)
FC 7 (2500 cycles)	102	34	0.7	2.0	6.4 (σ = 0.8)
FC 8 (4000 cycles)	130	43	0.6	2.4	6.1 (σ = 1.3)
FC 11 (24 hr. 1.3 V hold)	186	62	0.4	3.5	4.1 (σ = 1.1)

In addition to porosity, Dijkstra tortuosity, and limiting current density are shown for each sample in Table 4. Limiting currents were read from the polarization data in Figure 21. Porosity data in Table 4 are the averages of the FIB-SEM measurements from Figure 22. Tortuosity decreased slightly then increased slightly to above the BOL value although the range was only 15% of the BOL value and limiting current reduced by only 13% after 4000 cycles and 130 $\mu g_C/cm^2$ lost.

Table 4 – Porosity, tortuosity, and limiting current after 0, 500, 1500, 2500, and 4000 AST cycles to induce corrosion.

Sample	$\varepsilon_{\mathrm{FIB-SEM}}$	τ_{Dijk}	i_{lim} [A/cm^2]
BOL	0.40	1.61 (σ = 0.12)	1.86
FC 5 (500 cycles)	0.51	1.56 (σ = 0.16)	1.84
FC 6 (1500 cycles)	0.48	1.54 (σ = 0.13)	1.74
FC 7 (2500 cycles)	0.47	1.55 (σ = 0.14)	1.64
FC 8 (4000 cycles)	0.45	1.77 (σ = 0.18)	1.62

Perhaps the most significant finding of this project was that cathode porosity, tortuosity, and limiting current were not severely affected by substantial corrosion. These mass-transport characteristics varied as to suggest that effective oxygen diffusion through meso- and macropores of corroded cathodes was not hindered and may have increased although the overall variation was small. Importantly, this demonstrates that microstructural "collapse," as has been implicated, was not the cause of cell failure as defined by the DOE durability target and ostensibly need not be the failure mode preventing cells from reaching these targets. Microstructural collapse was observed after further corrosion (FC 11, 186 $\mu g_c/cm^2$) but cell performance had failed long before the collapse was observed.

An expanded understanding of the carbon loss and transport parameter observations can be realized by considering the perspective of the carbon support primary particle. From this perspective, carbon loss and rearrangement (corrosion) may take place by four modes as shown in Figure 23: inter-/intra- particle hollowing/collapse. These modes may be coupled and may occur locally and/or globally within the cathode.

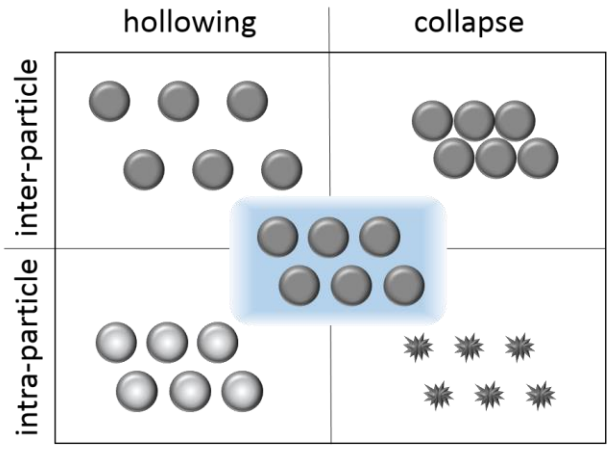

Figure 23 - Four modes of corrosion relative to carbon support primary particles

The small variations in parameters governing cathode mass-transport resistance in the microstructure suggest that neither inter-particle collapse nor hollowing substantially affected the microstructure. To corroborate this, two-point correlation functions normalized by phase fraction, $S_2(r)/\epsilon$, for the solid phase are shown in Figure 24 where r is the norm of the sampled vector. For samples with more than one FIB-SEM result, the result with porosity nearest the mean for each carbon loss value was used. $S_2(r)$ decayed approximately equally rapidly and displayed slight short-range order around 50 nm for all samples, characteristic of the mean pore diameter. Anticipated limiting behavior was closely followed: $S_2(r) \to \epsilon$ as $r \to 0$ and $S_2(r) \to \epsilon^2$ as $r \to \infty$. Two-point cluster

functions were also calculated but displayed nearly indistinguishable behavior from $S_2(r)$. These results corroborate the porosity results indicating that no dramatic change in short-range or long-range inter-particle order took place; that is, neither hollowing nor collapse, after corrosion.

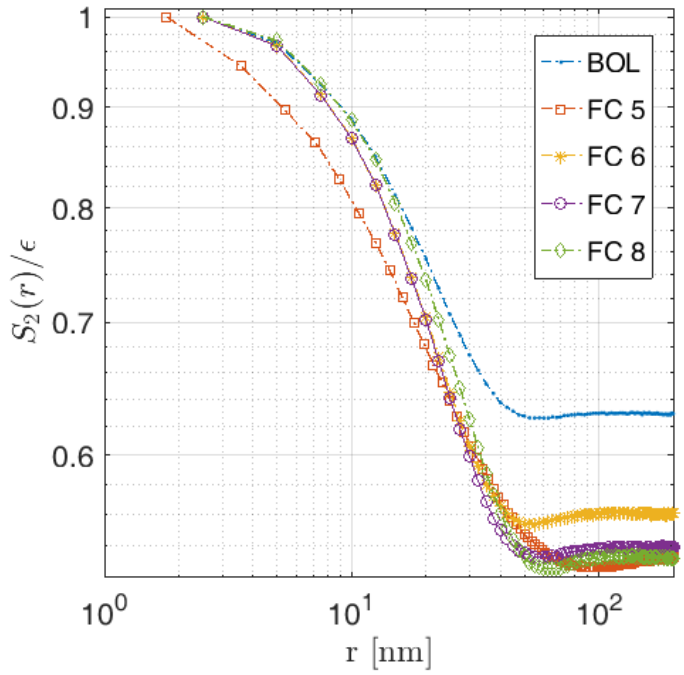

Figure 24 - Two-point correlation functions normalized by solid phase fraction, (S_2 (r))/ϵ, determined by a Monte Carlo method with >106 randomly spatially located samplings at each value of r.

Ruling out gross inter-particle reorganization suggests intra-particle hollowing was the dominant mode of corrosion. Indeed, preferential corrosion of the amorphous carbon interior of carbon black primary particles (cf. turbostratic graphitic exteriors) has been observed by IL-TEM imaging[62,20]. Moreover, the mass balance results of FC 5-8 corroborate this because intra-particle hollowing would not be directly observed by the FIB-SEM imaging performed in this work. Thus, if interior, amorphous carbon preferentially corroded but remained "hidden" from FIB-SEM, porosity would be lost

slower by mass balance than by FIB-SEM, as was observed. This may also help explain the slightly higher porosities calculated by mass balance as compared to FIB-SEM. Progressive intra-particle hollowing would not strongly influence tortuosity or the two-point correlation function, further in agreement with those results. Even via a purely intra-particle hollowing route, some critical extent of corrosion would likely result in mechanical instability of the carbon support that would eventually cause local and/or global collapse.

A discrepancy arose between the BOL and FC 5 samples whereby mass balance porosity decreased while FIB-SEM porosity increased. Although the cause of this discrepancy was not fully resolved, an explanation can be posited. FIB-SEM interrogates cathode volumes from the cathode surface (i.e., the cathode/GDL interface) to some through-plane depth regardless of where that surface is relative to BOL cathode thickness. Figure 25 clarifies this fact, showing how the FIB-SEM imaged volume approaches the PEM as cathode thickness is lost during corrosion. Recalling that considerable cathode thickness was lost from BOL to FC 5, the two discrepant samples, while thickness loss was greatly reduced among other samples, gives reason to suspect heterogeneous carbon loss and/or rearrangement took place from BOL to FC 5 but less so between FC 5-8.

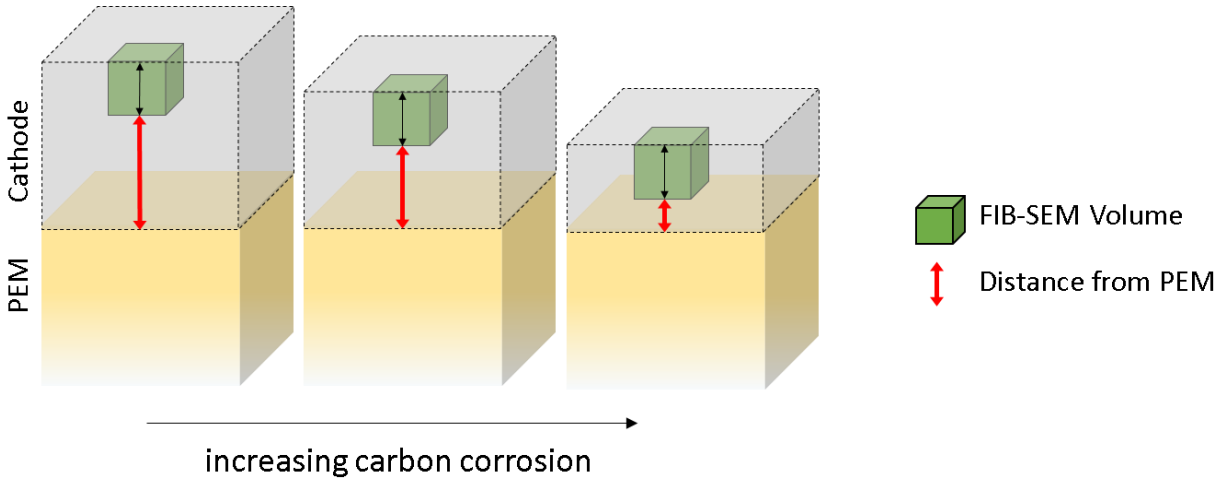

Figure 25 - The FIB-SEM volume is always imaged at the surface of the cathode regardless of the distance from the proton exchange membrane.

Returning to performance changes, carbon and ECSA fraction losses versus number of cycles further explain the observed performance degradation. These are shown in Figure 26. Both data sets were fit with power law models of form $\alpha\left(N_{cycles}\right)^{\beta}$ with $\beta = 0.5$ for carbon and $\beta = 0.2$ for ECSA.

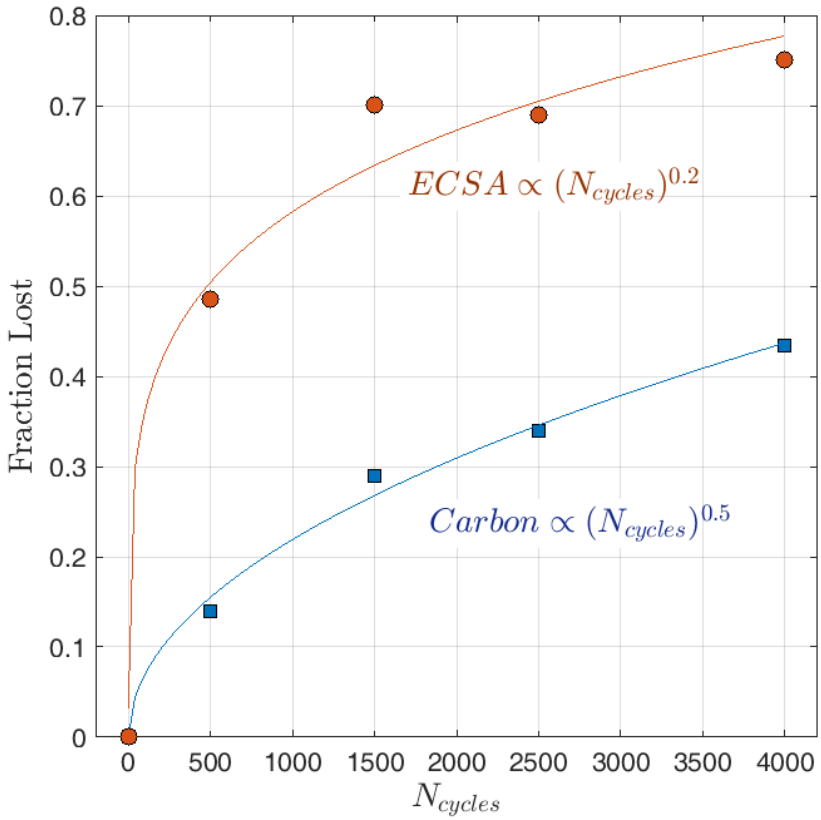

Figure 26 - Fraction of Carbon and ECSA Lost versus Number of Corrosion Cycles – loss as a function of the number of cycles applied). Corrosion protocol conditions were 0.4 V (3s) – 1.3 V (3s). Data were fit to an optimal power law model, best fit exponents were

The initial ECSA fraction loss rate was approximately an order of magnitude larger than the carbon fraction loss rate although the ECSA fraction loss rate decayed faster. Decay in the corrosion reaction rate could be due to one or more of the following: depletion of the preferentially corroding amorphous carbon, formation of passivating platinum-oxides that indirectly slow platinum-catalyzed corrosion, or formation of passivating carbon-oxides that directly slow corrosion[63,64]. The choice of 0.4 V as LPL was reducing relative to platinum-oxide formation potentials and most carbon-oxide formation potentials suggesting passivation was not a sufficient explanation for the observed decay in corrosion

rate. ECSA fraction was lost faster than carbon fraction (~49% after 500 cycles) indicating that platinum Ostwald ripening absent passivation could have mitigated Pt-C coupling thereby lessening corrosion promotion as fewer and fewer Pt catalytic sites remained available. Still, this did not rule out the explanation that preferential corrosion of the amorphous carbon took place; both could have been responsible for the decay in corrosion rate. As has been previously reported, the carbon corrosion rate displayed exponentially decaying behavior in long (>2 hrs.) corrosion protocols, which is characteristic of two species corroding in parallel at different rates, in this case, amorphous and graphitic carbon[65].

3.4 Conclusions

A commonly used AST was applied to several PEMFCs and performance, corrosion, and microstructure were investigated by FIB-SEM tomography and complementary techniques. The corrosion-induced variation in mass-transport resistance characteristics were small even as cell performance degraded beyond failure defined by the DOE target. Microstructural collapse did not occur until cell performance was far beyond a failed state and therefore was not the underlying cause of observed cell potential losses.

As suggested in the discussion and reported by other authors, the specific corrosion protocol applied could make considerable difference in the end condition and performance of the cell. The intrinsic and extrinsic corrosion-promoting qualities and experiences of a cell result in an historical “corrosion path” whereby some paths result in better cell performance than others. In this way, multiple paths to failure must exist and the least desirable paths could possibly be avoided through rational design. Similar studies on a

broader range of corrosion conditions could help further quantify conditions that promote or inhibit microstructural collapse and demarcate which corrosion paths may lead to collapse, if any, before cell failure by other mechanisms.

As an improved co-understanding of carbon loss, performance, and microstructure becomes available, improvements in the predictive capability of degradation models are expected. Correlations between corrosion and microstructure could improve sophistication of continuum models while microstructural data could serve as a guide for atomistic and/or microkinetic models. A more complete understanding of degradation and mitigation strategies could help lead to widespread adoption of PEMFCs in the automotive sector.

CHAPTER 4. COMBINING TOMOGRAPHIC IMAGING WITH IN SILICO COMPUTATION FOR RAPID EFFECTIVE PEMFC CATHODE TRANSPORT CHARACTERIZATION

In this project, an approach for determination of effective oxygen diffusivity of a PEMFC cathode catalyst layer was developed. Accurate determination of effective oxygen diffusivity is critical for modeling and characterization of cathode design architectures. *In silico* geometric characterization methods exploit the increasing availability, capability, and decreasing cost of both tomographic imaging and high-performance computing. Geometric methods can be made simple and fast and could accelerate efforts to iteratively improve cathode design. The method described herein relied on mathematically exact and statistically significant definitions of geometric tortuosity and geometric constrictivity, in addition to porosity. To demonstrate generality and robustness, a correlation for obstruction factor underpinned by these parameters was statistically induced from hundreds of instantiations of stochastic cathode microstructures generated by a simulated annealing method and validated versus the obstruction factor of real cathode microstructures obtained separately by our group and a prominent group working on cathode FIB-SEM at the University of Freiburg. This work demonstrated the utility and viability of adopting a combined tomography/geometric-computational approach for determination of the cathode catalyst layer effective diffusivity and underlying geometric transport properties. The analysis assumed a typical platinum catalyst-based PEMFC cathode but could easily be extended to PGM-free cathodes in which accurate characterization may be of even greater importance due to the thicker cathode layers required in PGM-free systems. This approach

could be widely adopted and relied upon for characterization as the materials and processing conditions of cathode layers are iteratively tested and improved.

4.1 Motivation: Geometric Obstruction Factor for Cathode Transport

To quantify mass transport at the component and full-cell length scale, researchers often balance simplicity and accuracy with macro-homogenized governing equations through which a constant effective diffusivity parameter mediates the flux-force constitutive relation for oxygen transport. For example Equation (4-1) and Equation (4-2) comprise a common mathematical relation for effective diffusivity as would govern oxygen diffusing in the PEMFC cathode layer.[66,57,67]

$$D_{O_2}^{\text{eff}} = \frac{\varepsilon}{\tau}\overline{D}_{O_2} \tag{4-1}$$

$$\overline{D}_{O_2}{}^{-1} = D_{O_2,\text{molecular}}{}^{-1} + D_{O_2,\text{Knudsen}}{}^{-1} \tag{4-2}$$

From theory of gaseous transport in porous media, these equations invoke intrinsic properties of the porous medium to describe an effective diffusivity, $D_{O_2}^{\text{eff}}$, that accounts for the well-known diffusion hindrance observed in a porous medium as compared to an open channel. Porosity, ε, tortuosity factor, τ, and the pore size distribution, implicitly via Equation **Error! Reference source not found.**(4-2) are often used. In pursuit of the technical targets, researchers seek to accurately measure and ultimately maximize $D_{O_2}^{\text{eff}}$ when testing new materials and architectures and when predicting cell performance. The importance of an accurate determination of $D_{O_2}^{\text{eff}}$ can be demonstrated by a simple model of

cell performance via Equation 3.[57,68] U_{cell} is cell potential, i_d is the exchange current density, U is an open circuit voltage parameter, b_1 is the Tafel slope at low i_d, b_2 is the Tafel slope at high i_d, R_{mem} are the ohmic resistances assumed dominated by the membrane, and i_{lim} is the limiting current density.

$$U_{cell} = U - b_1 \ln\left(\frac{i_d}{i_0}\right) - R_{mem} i_d - b_2 \ln\left(\frac{i_{lim} - i_d}{i_{lim}}\right) \tag{4-3}$$

For four electron oxygen reduction with cathode oxygen transport resistance dominating the diffusion media transport resistance[69] and all else equal, a 10% decrease in effective diffusivity determination could be expected to decrease the limiting current density by ~10% according to (4-4).

$$\begin{aligned} i_{d,lim} = nF\boldsymbol{N}_{O_2,lim} &= 4FD_{O_2}^{\text{eff}} L_{cath}^{-1} \left(C_{O_{2,channel}} - C_{O_{2,PtSurf}}\right) \\ &= 4FD_{O_2}^{\text{eff}} L_{cath}^{-1} C_{O_{2,channel}} \end{aligned} \tag{4-4}$$

This variation is critical: simulated polarization and power density plots are shown in Figure 27 for an approximately state-of-the-art cell where limiting current was decreased by 10% and 20%, from 2.5 A/cm^2 to 2.25 and 2 A/cm^2. Simulated parameters were U = 0.95, b_1 = 60 mV/dec, i_0 = 1e-2 A/cm2, R_{mem} = 3 mΩcm^2, and b_2 = 120 mV/dec.

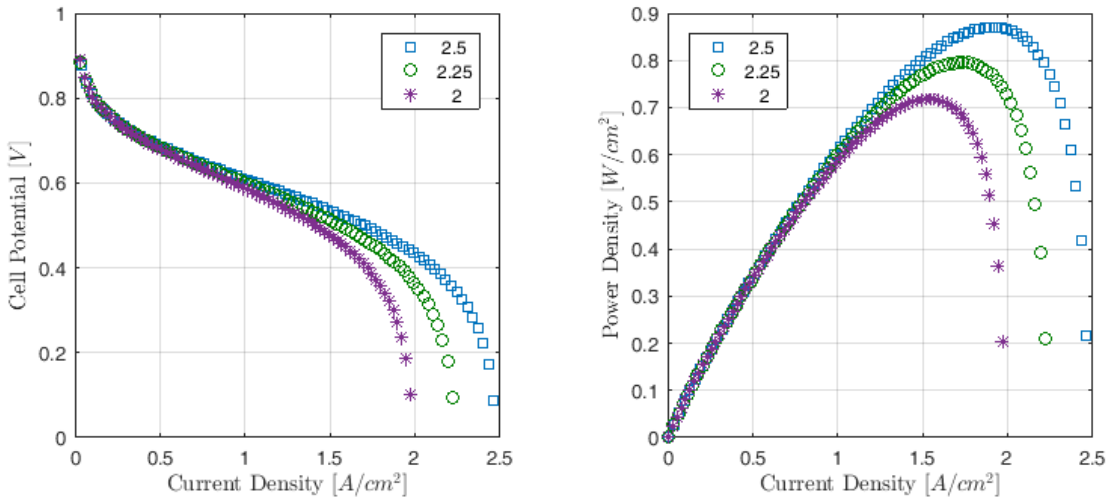

Figure 27: Cell potential (left) and power density (right) versus current density for three limiting currents: 2.5, 2.25, and 2.0 Amps/cm^2

From the maxima in Figure 27 on right, the peak power density may be concomitantly reduced by ~10% and ~20%, roughly the difference between beginning of life and end of life for a cell. This amount of uncertainty in $D_{O_2}^{eff}$ could substantially confound modeling and characterization efforts of cathode architectures. Unfortunately, *operando* measurement of cathode $D_{O_2}^{eff}$ remains challenging due to the cathode's necessary coupling with supporting components (e.g. diffusion media and proton-exchange membrane) and hardware (e.g. bipolar plates) that enable cell operation. This obliges alternative approaches, a niche which contemporary and emerging tomographic methods can fill.

Tomographic methods offer direct observation of relatively large volumes (100 nm^3 – 1 mm^3) of cathode microstructure capable of resolving some or all the constituent materials (catalyst, catalyst support, ionomer). Direct imaging also confers information of the complementary void phase, i.e., pore connectivity. Tomographic techniques are becoming

increasingly sophisticated through simultaneous detection of multiple signals, advances in computer vision and software automation, and/or *post-factum* mathematical processing. Simultaneously, the cost of data acquisition is decreasing due to steadily increasing demand and the very low cost of a marginal tool-hour.[70] Accordingly, PEMFC cathode tomographic data which is further evidenced by a database search as shown in Figure 2.

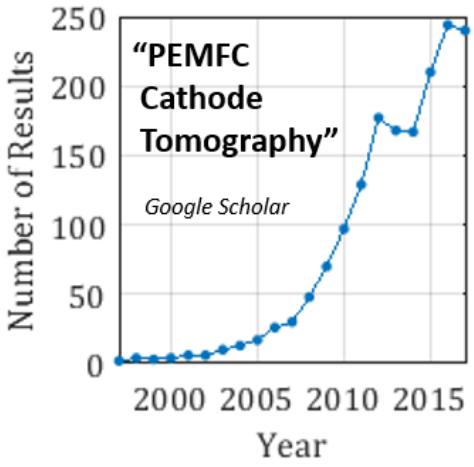

Figure 28: Google Scholar database search results by year for "PEMFC Cathode Tomography"

Tomographic data may be used in two ways: 1) proceeding "downward;" simulating increasingly complex physics on directly imaged cathodes for an increasingly realistic understanding of *operando* behavior and/or 2) proceeding "upward;" translating the most accurate available information from the micro-scale to the macro-scale to inform full-component and full-cell modeling and characterization. This paper concerns the second pursuit.

To determine $D_{O_2}^{\text{eff}}$ from tomographic data, one may simulate diffusion as in an *operando* cathode and compare the result to diffusion in an open channel of equal dimension as in Figure 3.

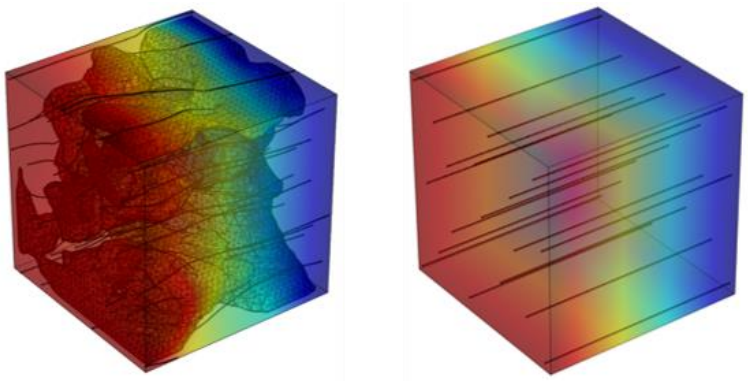

Figure 29: Example of simulated diffusion through a porous cathode (left) as compared to an open channel (right) with a concentration gradient (red → blue) and transport trajectories (black).

The ratio of the normal components of the O_2 fluxes, $\hat{n} \cdot \boldsymbol{N}_{O_2}$, in the porous (p) to open (o) medium may then be determined as in Equation (4-5).

$$\alpha = \frac{\iint \hat{n} \cdot \boldsymbol{N}_{O_2,p}\, dS}{\iint \hat{n} \cdot \boldsymbol{N}_{O_2,o}\, dS} \tag{4-5}$$

α is a ratio describing the reduction of diffusive material flux due to the presence of the porous medium where S is an orientable surface through which oxygen flows, for example, a planar cross-section orthogonal to the through-plane direction of the cathode. Referred to as the obstruction factor or formation factor, α is equivalently interpreted as in Equation (4-6).

$$D_{O_2}^{\text{eff}} = \alpha D_{O_2} \tag{4-6}$$

In Equation (4-6), D_{O_2} can be replaced with $\overline{D}_{O_2}$ from Equation (4-2) if a molecular diffusion resistance is assumed to precede a Knudsen diffusion resistance in series. The approach of Equations (4-5) and (4-6) lumps and circumvents properties such as porosity and tortuosity that describe the porous medium from theories of transport in porous media. However, it is often desirable to separate individual effects both for characterization purposes and for use in component- and cell-scale modeling.

Porosity is well defined and made tractable by high-resolution tomography, but significant ambiguity remains in the tortuosity parameter including its definition, determination, and practical use. Ambiguity in tortuosity propagates forward in characterizing the porous medium, determining $D_{O_2}^{\text{eff}}$, and quantifying transport a problem that will require further attention to realize improved PEMFCs. Tjaden et al. excellently renewed attention[71] toward this shortcoming as it applies to electrochemical devices although tortuosity has a long history which was addressed well by Clennell[72] among others. Tortuosity is colloquially defined as the elongation of fluid/particle pathing through a porous medium as compared to linear pathing. However, adopting the mathematical formulation of Equations (4-1) and (4-2), τ is a parameter that accounts for everything hindering diffusion minus porosity; an "everything else" parameter. As an extension, the constrictivity factor, δ, is occasionally implemented nominally to account for flux resistance arising from transport through constrictive, small radius pores as compared to

un-constrictive, large radius pores. Mathematically, this can be written as Equation (6), a modification to Equation (4-7).[73]

$$D_{O_2}^{\text{eff}} = \frac{\varepsilon\delta}{\tau}\overline{D}_{O_2} \tag{4-7}$$

By conception, δ and τ are distinct parameters and permutations of microstructures featuring low/medium/high τ/δ could be realized. δ and τ can also be mathematically posed separately, an essential step toward deconvoluting separate effects. However, δ and τ are not *fully* independent parameters when describing a real fluid in porous media; pathing *is* influenced by the pore size distribution and connectivity in a random, heterogenous material.[74]

Although a satisfactory, generalized reconciliation still does not exist, both the tortuous path elongation and pore radii can be precisely mathematically defined and calculated by geometric methods at the microscale with the aid of spatial tomographic imaging data. This project demonstrates a method to obtain $D_{O_2}^{\text{eff}}$ by a purely geometric approach utilizing geometric tortuosity, geometric constrictivity, and porosity as transport parameters. Using only these parameters, a correlation for $D_{O_2}^{\text{eff}}$ was induced demonstrating the viability of reliance on tomographic imaging data for improved cathode characterization and transport modeling with simple, inexpensive methods that could be ubiquitously applied. Extensive description of the methodology and calculations are first presented followed by results, discussion and general conclusions.

4.2 Role of Simulated Volume

Simulations on the largest possible volumes of cathode data would be desirable to ensure results are statistically representative of entire cathodes. Unfortunately, computational cost scales with the number of nodes which scales with cube of the dimension of the computational domain for simulations on $\mathbb{R}^3$. To address this, porosity was used as a probe to assess the minimum representative simulated volume allowable for calculations on microstructures used in this work. Porosity was determined for randomly sampled, contiguous sub-volumes of FIB-SEM cathode microstructure of varying total number of voxels. One hundred porosity values were sampled for several values of total voxels. This result is shown in Figure 30 on left. When fewer total voxels are used, the porosity value determined is less likely to be representative of the mean value of the entire microstructure. To quantify the error in using this method, the maximum percent deviation of each hundred samples from the mean porosity was plotted in Figure 30 on right. The maximum percent deviation was deemed sufficiently small when 10^8 voxels were used. Thus, all subsequent calculations and simulations were performed on volumes of 1.25×10^8 voxels.

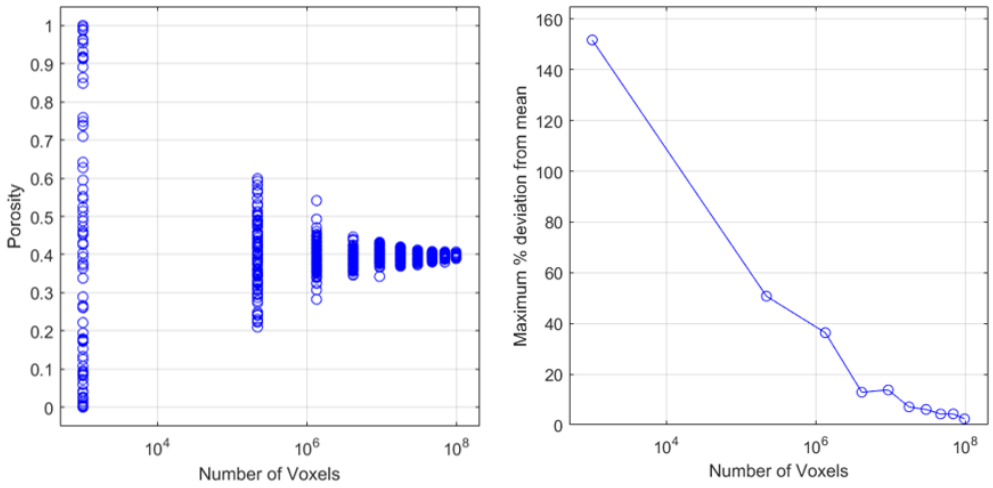

Figure 30 - Porosity versus total number of voxels with 100 porosity samplings for each number of voxels (left), maximum percent deviation of the porosity calculation versus number of voxels (right).

4.3 Geometric Tortuosity and Constrictivity

Geometric tortuosity was founded upon a short path distance, L_{sp}, and was calculated in the PEMFC through-plane direction by a Dijkstra pathfinding algorithm. Dijkstra's algorithm is described elsewhere[54] in detail but a brief explanation is provided here. From graph theory, the pore-phase voxels of the microstructure comprise a graph of unweighted, undirected nodes. For the purposes of determining tortuosity by short path distance, these nodes are initially considered unvisited. A starting node is chosen and the distance to its neighbors is determined. These neighbors are then considered visited. The distances to the neighbors of those neighbors are then determined, and so on. The shortest path distance from the starting node to any other node is updated if a smaller distance is found while the front of visited nodes propagates forward. Once all voxels are visited, the shortest path from the start voxel to the end voxel is rigorously determined.

In the context of transport in porous media, short path distance and therefore, geometric tortuosity, can be defined in more than one way. In Figure 31, a "Straight-Across" path is shown below in blue and a "First-Through" path is shown in red. The difference is that the Straight-Across path terminates when it reaches the same corresponding point of the microstructure on the end edge (or its nearest available end point if the corresponding point is of different phase) while the First-Through path terminates at the point on the end edge representing the shortest possible pathing through the media. For simplicity of demonstration, the example below is two-dimensional although the short-paths used in this work were determined in three-dimensions.

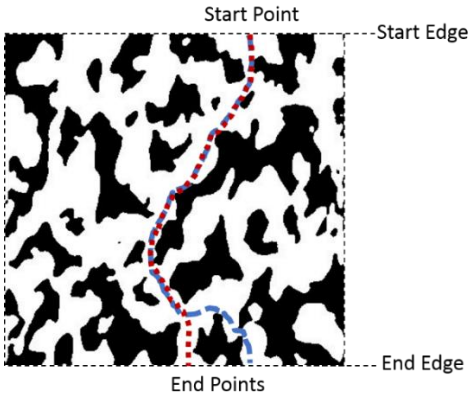

Figure 31: 2D example of a Straight-Across path (blue) compared to a First-Through path (red).

Straight-Across paths represent the most commonly applied definition of the tortuosity while First-Through paths represent paths of minimum "geometric resistance" across the cathode microstructure. The difference between the two appears negligible in the example above but could become drastic when liquid saturation becomes comparable to porosity such that a significant fraction of pores become blocked, depending on local wettability.[75,76] Partially blocked pores would likely increase the ratio of Straight-Across distance to First-Through distance. This paper does not explicitly consider the presence of

liquid water because the local distribution of ionomer on platinum/carbon catalyst and the ionomer's side-chain orientation control local wettability properties and these remain largely unknown. However, this understanding is anticipated to improve in coming years[77,78,79] and the methods described in this paper can be easily extended to investigate nonzero water saturation once the local ionomer distribution and dispersion properties on Pt/C are better understood. In this work, geometric tortuosity, τ_g, was defined as the "Straight-Across" short-path distance divided by the through-plane length of the cathode.

Straight-Across tortuosity was determined as discussed in the Methods section. Figure 32 demonstrates Straight-Across short path statistics. On left, several short path lengths normalized by the cathode thickness were sampled and the mean for all sixty samples is plotted as a black line. The histogram and standard deviation is shown at middle. On right, the probability that a mean geometric tortuosity determined by n trials was within β percent error of the $n = 60$ mean value is plotted. This was determined by a Monte Carlo method of $>10^6$ samplings and probability curves are shown for $\beta = 0.5, 1, 2,$ and 3 percent. This demonstrates that only a handful of samplings (trials) are required to obtain a mean geometric tortuosity with acceptably low deviation error i.e. a tortuosity representative of the entire cathode microstructure. Naturally, as seen in Figure A2 on right, more trials monotonically increased the probability that the mean was within β percent error of the $n = 60$ mean. Importantly, this method of sampling multiple trials is ideally suited for parallel processing (i.e. on multi-core computers or clusters) which ensures modest total computational times.

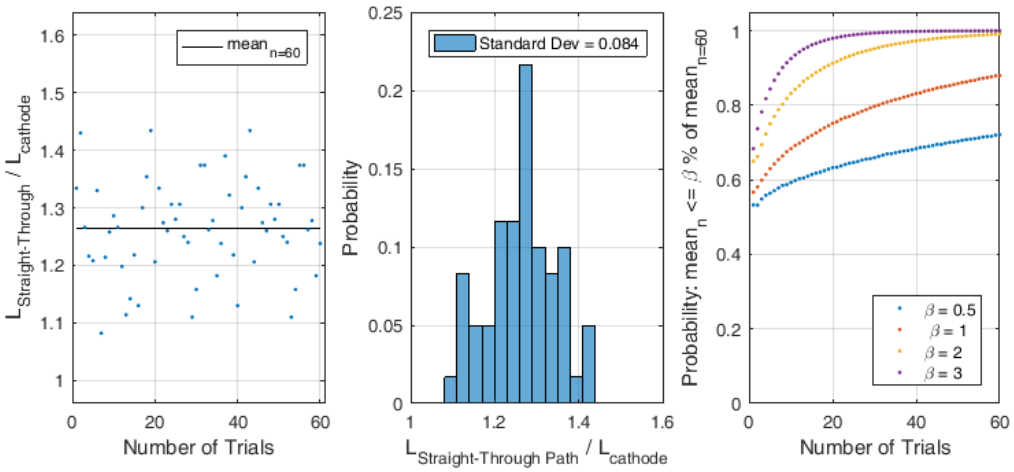

Figure 32 - Straight-Across path lengths normalized by cathode thickness and their mean (n = 60) (left), histogram and standard deviation (middle), probability that n trials will result in <= β percent deviation from the n = 60 mean value (right).

Constrictivity is a macroscopic parameter founded upon pore radii and their connectivity and is discussed at length in various texts on transport in porous media.[80] To determine pore radii, a maximal-sphere-inscription method is commonly applied[81] which has helped characterize various porous media and informed pore-scale models.[82] However, this method has some difficulty assigning local radii to, and requires subjective intervention near, irregular, microscopic (cf. mesoscopic) features.[83] These features are typical, not exceptional, in PEMFC cathodes.[8] For use of pore radii in accurate geometric calculations, a voxel-wise-accurate method for local pore radius is desirable as geometric methods sample specific voxels, not full pores. A method referred to in this work as an "Asterisk" method was developed and applied. At each voxel in the pore phase, twenty-six vectors representing the 26-connected directions emanate radially outward. Each vector extends outward until reaching the solid phase. The mean of the norms of these 26 vectors is labeled the local pore radius for that voxel. This provides a measure of the characteristic pore size at every voxel without undue bias near irregular features into which maximal spheres may

not comfortably fit. Graphics in Figure 5 visually depict the Asterisk method for determination of pore radius.

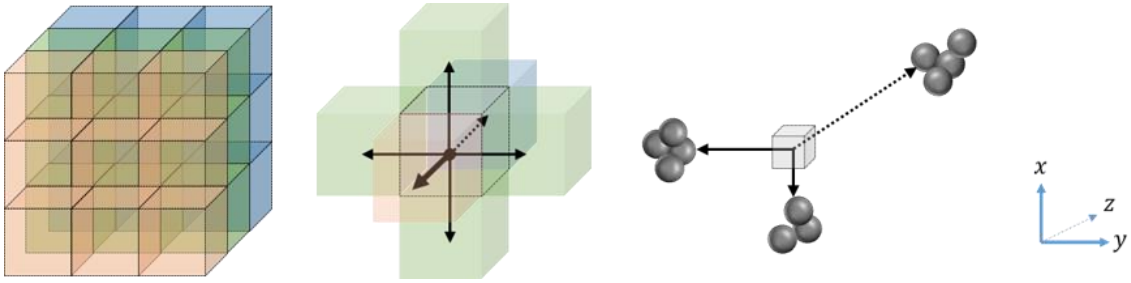

Figure 33 - 27 voxels demonstrating 26-connection of the central, test voxel (left); 6-connected voectors emanating from the test voxel for simplicity of depiction (middle); 3 emanating vectors of varying length extend radially outward until solid obstacles are reached (right).

The Asterisk method reproduced a cathode pore size distribution consistent with many other researchers.[26,84] The histogram is shown in Figure 34 on left and is voxel-wise accurate as seen in a representative 2D example image in Figure 34 on right. Note that the histogram in Figure 34 displays pore diameters for ease of comparison to most of the relevant literature although pore radii are used elsewhere in this work.

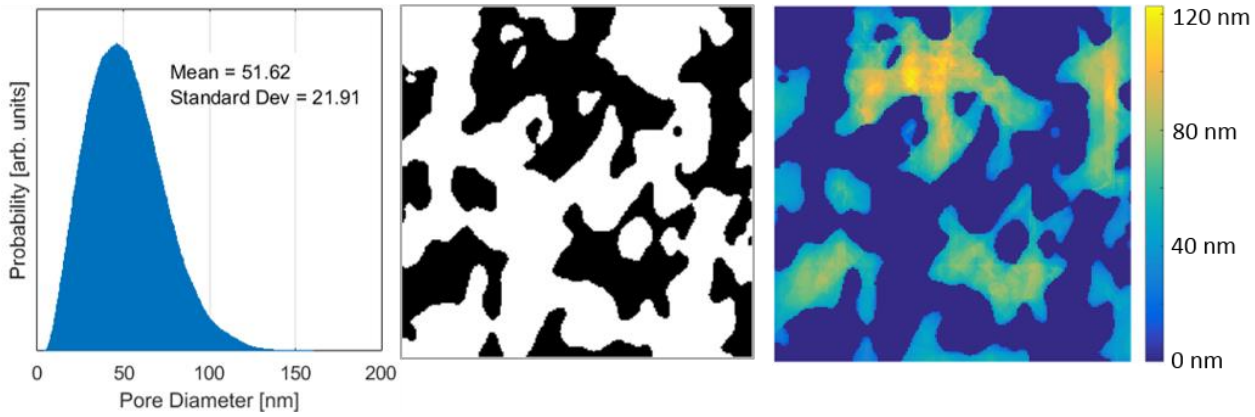

Figure 34 - Pore size distribution by Asterisk method (left), 2D example of a digitally segmented cathode cross-section (middle), 2D example of the voxel-wise pore size by Asterisk method (right).

Macroscopically, δ modulates (decreases) effective diffusivity to account for the constrictive nature of the pores of the microstructure. Mathematically, $\delta \in \Delta : \Delta = (0,1)$ while physically, $\delta \to 0$ represents the limit of perfectly constricted pores, an impermeable solid, and $\delta \to 1$ represents perfectly un-constricted pores, an open channel.[85] Microscopically, equipped with the voxel-wise pore radius as determined by the Asterisk method, a tortuous path as previously described will traverse voxels with known pore radius and therefore, known constrictive character. This constrictive character was exploited to add the effect of bulk flux-resistance due to narrowed pores in addition to the effect of nonlinear, tortuous pathing. For each tortuous path, the mean of radii of that path $\langle r_{sp} \rangle$, was determined. To scale geometric constrictivity, δ_g, to a value within the (0,1) range, $\langle r_{sp} \rangle$ was normalized by r_m the pore radius at which oxygen Knudsen diffusivity equals oxygen molecular diffusivity. Importantly, the normalization radius was independent of any specific microstructure (e.g. compared to the largest pore radius in the observed distribution) such that accurate comparison could be made between various

microstructures. Thus, $\delta_g = \langle r_{sp} \rangle / r_m$ and r_m was set equal to 1.6×10^{-6}. This normalization is elaborated upon below in the CFD Simulations Section

4.4 Simulated Annealing of Stochastic Microstructures

Stochastic cathode microstructures were generated by a simulated annealing method similar to and inspired by the work of Kim and Pitsch, Yeong and Torquato, Mukherjee and Wang, and Inoue and Kawase.[86,87,88,89] Polydisperse, spherical occlusions were randomly seeded in a periodic volume and annealing was simulated via occlusion translation/relaxation that minimized a relevant energy function. Each step in the annealing process resulted in an instantiation of the stochastic microstructure where instantiation i is denoted ξ_i such that a seed microstructure was ξ_1, the microstructure after one annealing step was ξ_2, and a microstructure was considered fully annealed when $\xi_n - \xi_{FIBSEM} \leq \psi$ where ψ was a specified tolerance. The energy function was defined as the deviation of the stochastic microstructure's two-point correlation function $S_2(r)$ from the "true" $S_2(r)$ determined from a FIB-SEM microstructure as in Equation (4-8).

$$E(\xi_i) = \sum_r \left[S_2(r)_{FIBSEM} - S_2(r)_{\xi_i} \right] \tag{4-8}$$

A plot of a typical pre-annealed $S_2(r)$ is shown in Figure 35 at middle and its annealing correlation function is on right. ψ was set equal to 0.03 which corresponded to less than 1% total devitation of from $S_2(r)_{FIBSEM}$.

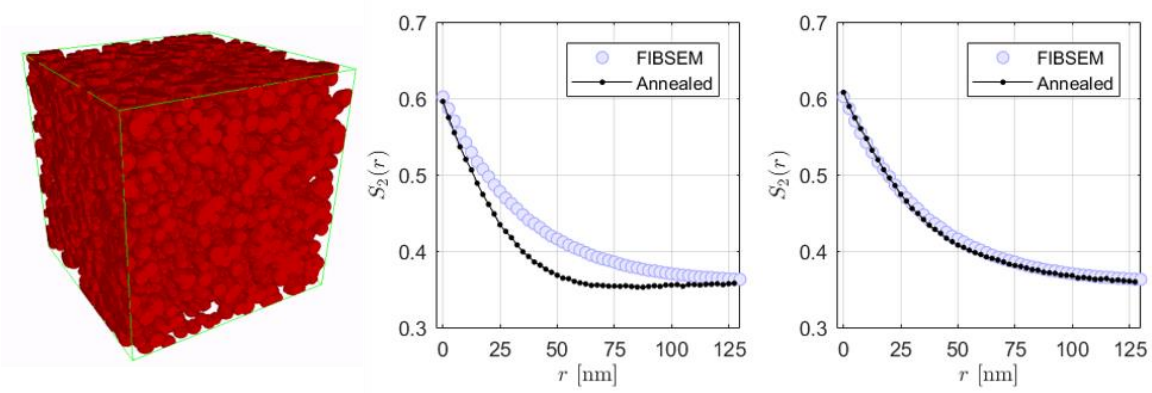

Figure 35 - Example of a stochastic, annealed microstructure (1.25 um x 1.25 um x 1.25 um) (left), $S_2(r)_\xi$ before and after annealing compared to $S_2(r)_{FIBSEM}$ (right).

As Kim and Pitsch noted, the choice of annealing algorithm only determines the *rate* at which the microstructure converges to the annealed structure, assuming the algorithm chosen can reach the fully annealed state.[89] Still, it is desirable for convergence to take place in reasonable time. To speed convergence, microstructures were seeded with a system representative of real cathodes and hypothetical aggregation dynamics were applied. Modern furnace blacks for electrochemical applications (e.g. Vulcan and Ketjen) feature narrow primary particle size distributions.[90,62] To rapidly mimic the structure of real cathodes, heterogeneous structures of monodisperse spheres with ionomer thin films, Rayleigh-distributed, polydisperse spheres were randomly distributed in a periodic volume. The probability density function of a Rayleigh distribution shifted to exhibit a minimum allowable radius corresponding to a minimum radius of carbon black primary particles, r_{min}, is given by Equation (4-9).

$$P(r) = \left(\frac{r}{s^2}\right)\exp\left(\frac{-r^2}{2s^2}\right) + r_{min} \tag{4-9}$$

The polydispersity of the occlusions endowed a similar narrow range of occlusion radii to the stochastic microstructure such that the smallest occlusion was approximately equal to the smallest radius of a typical carbon black primary particle and the largest occlusion was ~20% larger in radius than the largest typical carbon black primary particle to allow for the presence of a non-uniformly distributed ionomer film with thickness on the order of nanometers.[91] Accordingly, the spherical occlusions obeyed Rayleigh statistics with $s = 2$ and $r_{min} = 23$ nm with a maximum particle size enforced at 25% greater than the mean occlusion radius. Aggregation and agglomeration dynamics of carbon black and cathode catalyst dispersion inks remain poorly understood so hypothetical dynamics were applied in this work.[90,62] Although the dynamics were not necessarily realistic, the final, annealed microstructures were realistic because of the initially seeded structures and the final statistical homology with the FIB-SEM correlation function. During annealing, occlusions translated while experiencing an interparticle pair-potential and a thermal-like (random) perturbation that diminished over time according to a slow linear cooling schedule. The pairwise force, assumed conservative, on a particle was chosen empirically and served only to accelerate annealing. The force on a particle arising from the interaction between it and another particle (particles j and k) was given by Equation (4-10). This force profile ensured a steep response at small distances and a long, attenuated response at longer distances to allow longer-ranging order to arise as was observed in the FIB-SEM $S_2(r)$.

$$\boldsymbol{F}_{jk} = \left(\frac{\beta_1}{r_{jk}} + \frac{\beta_2}{r_{jk}^2} - \frac{\beta_3}{r_{jk}^6}\right)\hat{\boldsymbol{r}}_{jk} \tag{4-10}$$

The parameters used were β_1 = 0.1, β_2 = 1, and β_3 = 1e5, $\hat{\boldsymbol{r}}_{jk}$ was the unit vector from particle j towards particle k, and r_{jk} was an adjusted interparticle distance given by Equations (4-11) and (4-12).

$$r_{jk} = d_{jk} + r_{EQ} \tag{4-11}$$

$$d_{jk} = \|x_{jk}\| - \max(r_j, r_k) + \min(r_j, r_k) \tag{4-12}$$

$\|x_{jk}\|$ was the 2-norm (length) of the vector from the centroid of particle j to particle k, and r_j was the radius of particle j. The adjusted distance allowed particles to equilibrate under influence of the force such that partial overlap of particles, more than kissing but less than full engulfment, was energetically favored. The amount of overlap was tuned by the r_{EQ} parameter and was set equal to 32.7 nm in this work. This ensured particles equilibrated such that the centroid of the smaller particle would reside just inside the larger particle.

Because this approach is forward-looking, a weakness was reliance on existing FIB-SEM data for simulated annealing. Due to the strong dependence of $S_2(r)$ on phase fraction, microstructures annealed to the FIB-SEM data would all be 40% porous because the FIB-SEM microstructure was 40% porous. This has benefits and drawbacks. On the one hand, all PEM cathodes made with conventional materials and processing conditions will exhibit porosity near this value so 40% is suitable and representative. On the other hand, robust, general results would be worse off without accounting for variation in porosity, an essential property contributing to the obstruction factor. Accordingly, $S_2(r)_{40\%,FIBSEM}$ was scaled to allow generation of higher- and lower-porosity microstructures. The scaled functions,

$S_2(r)_{35\%}$ and $S_2(r)_{45\%}$ were determined by preserving essential statistical properties from $S_2(r)_{40\%,\ FIBSEM}$. For the scaled correlation functions, the desired porosities were chosen which automatically constrained $S_2(0)_{35\%}$, $S_2(0)_{45\%}$, $S_2(r \to \infty)_{35\%}$, and $S_2(r \to \infty)_{45\%}$.[55] Reasoning physically, the probability of decay of long-range order over distance of each correlation function should be similar given that the scaled functions are meant to represent the same materials and processing conditions only at different porosity values. Mathematically, we interpret this to imply that $\partial_r S_2(r)$ of the scaled functions should equal that of the true (FIB-SEM) function. Thus, $S_2(r)_{35\%}$ and $S_2(r)_{45\%}$ were constructed as to minimize $U(r)$, the difference of the first derivates of the scaled functions from the unscaled function over the relevant range of radii subject to the constrained values at $r = 0$ and $r \to \infty$ (Equation (4-13)). Figure 36 shows the scaled functions and their first derivatives as compared to the FIB-SEM function.

$$U(r) = \sum_{r}^{r_\infty} \partial_r S_2(r)_{40\%} - \partial_r S_2(r)_{35/45\%} \tag{4-13}$$

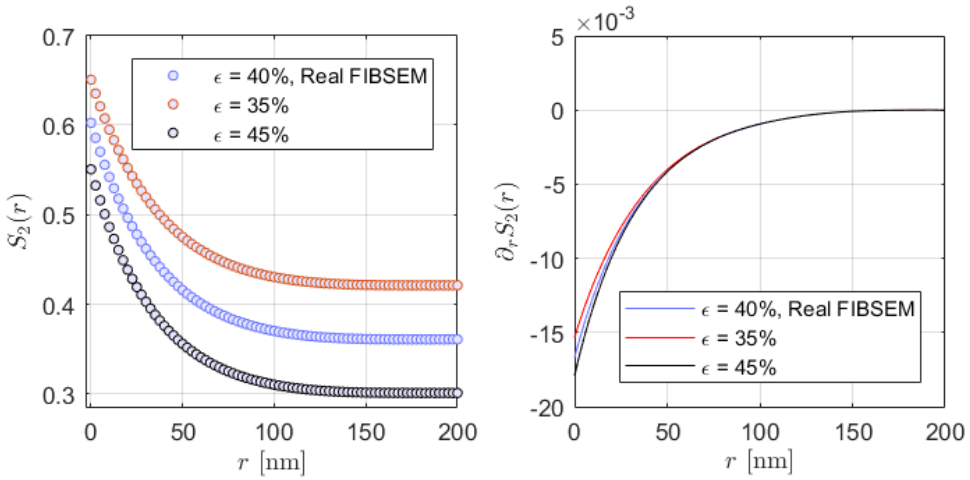

Figure 36 - Two-point correlation function for the solid phase (left). First derivative of the correlation function (right). The 40% porosity function was determined from FIB-SEM data, 35% and 45% porosity were inferred.

4.5 Finite Difference Method for Obstruction Factor

3D finite difference simulations followed the approach described by Figure 29 and Equation (4-5). Laplace's equation with spatially variable diffusivity governed non-dimensional oxygen transport as in Equation 1 and was relaxed by a Jacobi method according to the discretization in Equation (4-14). The spatial dimensions, x, y, z, are indexed as i, j, k, in the discretization and the differencing length was one voxel, the natural choice when working with segmented, structural tomographic images.

$$\nabla \cdot (D \nabla C) = 0 \tag{4-14}$$

Applying the chain rule, Equation (4-15) is obtained.

$$D\left(C^{(xx)} + C^{(yy)} + C^{(zz)}\right) + \left(D^{(x)} + D^{(y)} + D^{(z)}\right)$$
$$\left(C^{(x)} + C^{(y)} + C^{(z)}\right) = 0 \tag{4-15}$$

The generalized Taylor series is:

$$f(x_1, \ldots, x_n) = \sum_{j=0}^{\infty} \left\{ \frac{1}{j!} \left[\sum_{k=1}^{n} (x_k - a_k) \frac{\partial}{\partial x_k'} \right]^j f(x_1', \ldots, x_n') \right\} \tag{4-16}$$

For n = 3 and to 2nd-order accuracy,

$$f(x + \Delta x, y + \Delta y, z + \Delta z) = f(x, y, z) + (\Delta x) f^{(x)} + (\Delta y) f^{(y)} + (\Delta z) f^{(z)}$$
$$+ \frac{1}{2!} \left[(\Delta x)^2 f^{(xx)} + (\Delta y)^2 f^{(yy)} + (\Delta z)^2 f^{(zz)} + 2(\Delta x)(\Delta y) f^{(xy)} + \right. \tag{4-17}$$
$$\left. 2(\Delta x)(\Delta z) f^{(xz)} + 2(\Delta y)(\Delta z) f^{(yz)} \right].$$

Using a 6-stencil connectivity and summing or differencing discretizations for the first and second derivatives, the six equations for the derivatives are obtained.

$$f_{ijk}^{(xx)} = f_{i+1,j,k} + f_{i-1,j,k} - 2f_{i,j,k}$$

$$f_{ijk}^{(yy)} = f_{i,j+1,k} + f_{i,j-1,k} - 2f_{i,j,k}$$

$$f_{ijk}^{(zz)} = f_{i,j,k+1} + f_{i,j,k-1} - 2f_{i,j,k}$$

$$f_{ijk}^{(x)} = \frac{1}{2}\left(f_{i+1,j,k} - f_{i-1,j,k}\right) \tag{4-18}$$

$$f_{ijk}^{(y)} = \frac{1}{2}\left(f_{i,j+1,k} - f_{i,j-1,k}\right)$$

$$f_{ijk}^{(z)} = \frac{1}{2}\left(f_{i,j,k+1} - f_{i,j,k-1}\right)$$

Laplace's equation is restated in Equation (4-19) and grouping terms and after some algebra, Equation (4-20) is obtained. Note that the second term on the right-hand side of the discretization adds the effect of spatially-variable diffusivity. Without this term, the discretization would describe constant diffusivity over space.

$$\nabla \cdot \left(\widetilde{D}(x,y,z)\,\nabla C(x,y,z)\right) = 0 \tag{4-19}$$

$$\begin{aligned} C_{\mathrm{i,j,k}} = \frac{1}{6}\left[C_{\mathrm{i+1,j,k}} + C_{\mathrm{i-1,j,k}} + C_{\mathrm{i,j+1,k}} + C_{\mathrm{i,j-1,k}} + C_{\mathrm{i,j,k+1}} + C_{\mathrm{i,j,k-1}}\right] \\ + \frac{1}{24\widetilde{D}_{\mathrm{i,j,k}}}\left[\widetilde{D}_{\mathrm{i+1,j,k}} - \widetilde{D}_{\mathrm{i-1,j,k}} + \widetilde{D}_{\mathrm{i,j+1,k}} - \widetilde{D}_{\mathrm{i,j-1,k}} + \widetilde{D}_{\mathrm{i,j,k+1}} - \widetilde{D}_{\mathrm{i,j,k-1}}\right] \\ \times \left[C_{\mathrm{i+1,j,k}} - C_{\mathrm{i-1,j,k}} + C_{\mathrm{i,j+1,k}} - C_{\mathrm{i,j-1,k}} + C_{\mathrm{i,j,k+1}} - C_{\mathrm{i,j,k-1}}\right] \end{aligned} \tag{4-20}$$

Dirichlet boundary conditions were chosen to approximate a fuel cell operating in a mass-transport limiting condition; $C = x_{O_2} p_{cell}/RT \cong 10$ at x = 0 (the cathode/GDL interface) and $C = 0$ at $x = L_{cathode}$ (the opposite side of the microstructure near the cathode/PEM interface). These boundary conditions could be altered depending on expectations of current distribution in the cathode layer. Periodic boundary conditions were applied at the $y = 0$, $y = y_{max}$, $z = 0$, and $z = z_{max}$ boundaries to avoid artifice at the domain edges. A no-flux condition, $\boldsymbol{n} \cdot \nabla C = 0$, was applied at the void-solid interface everywhere in the microstructure. Importantly, the diffusivity, $\widetilde{D}$, used in Equation (4-19) and (4-20) was distinct from that in Equations (4-1) and (4-2). $\widetilde{D}$ is a parameterization of the molecular and Knudsen diffusivities as a function of voxel-wise pore radius. This parameterized diffusivity is elaborated upon below.

In these simulations, diffusion was considered for dilute oxygen in nitrogen with T = 353 K and p_{cell} = 1.5 × 10^5 Pa motivated by the environment of an *operando* PEMFC cathode. For the present analysis, water vapor was ignored which is justified at low relative humidity operation but may become problematic at high relative humidity. The Knudsen diffusivity for low-density, elastic hard-spheres is given by Equation (4-21) and the binary, molecular Chapman-Enskog diffusivity for an ideal gas is given by Equation (4-22).[74,92]

$$D_{Kn} = \frac{2r}{3}\sqrt{\frac{8RT}{\pi M_i}} \tag{4-21}$$

$$D_{m,ij} = \frac{3}{8\widetilde{N}p\sigma_{ij}^2\Omega_{D,ij}}\sqrt{\frac{(RT)^3}{2\pi}\left(\frac{1}{M_i}+\frac{1}{M_j}\right)} \tag{4-22}$$

R is the gas constant, T is temperature, M is molar mass, p is pressure, N is Avogadro's number, σ is the collisional cross-section, and Ω_D is the collision integral determined by a Lennard-Jones interaction potential. The Knudsen number is the ratio of the mean free path, λ, to the characteristic system length. The Maxwell mean free path for a pure, low-density gas is given by Equation (4-23) wherein k_B is Boltzmann's constant. For the present analysis, the similar mass and polarity of O_2 and N_2 obviate need for correction to the pure gas mean free path.

$$\lambda = \frac{k_B T}{\sqrt{2}\pi\sigma^2 p} \tag{4-23}$$

Transition regime diffusion theory attempts to marry the limiting cases of molecule-molecule collisions dominating with molecule-wall collisions dominating as the relevant length scales of the system become similar. Bosanquet diffusivity macroscopically expresses mass diffusing serially through both molecular and Knudsen regimes. In Figure 37 at left and middle, diffusivity vs. radius is shown for four considered diffusivities on log- and linear-axes plots. Knudsen number vs. radius is shown on right. For determination of the local (voxel-wise) diffusivity for use in the finite discretization, Bosanquet diffusivity was inappropriate as shown in Figure 37 at middle. Bosanquet diffusivity predicts diffusivity smaller than either the molecular or Knudsen regimes, particularly at larger pore radii. Recalling Figure 34 (left) and shown in Figure 37 (right), the pore sizes within two standard deviations of the mean, i.e., 95% of pores if assumed Gaussian distributed, reside within $1 < Kn < 20$.[74,93]

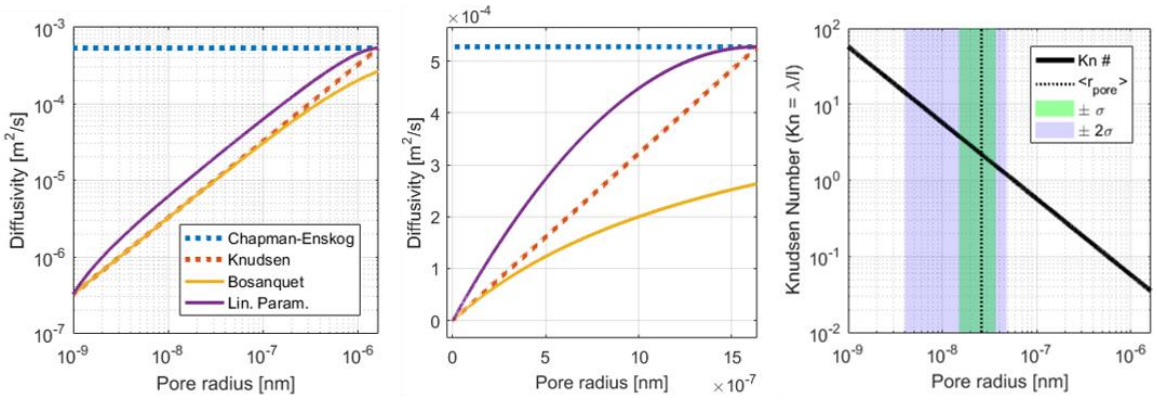

Figure 37 - Chapman Enskog diffusivity, Knudsen diffusivity, Bosanquet Diffusivity, and the linear parameterization of diffusivity (left and middle), Knudsen number versus pore radius with pore radius histogram overlain (right).

Accordingly, a local, voxel-wise accurate diffusivity was linearly parameterized to hybridize the Knudsen and molecular regimes as a function of r. This was accomplished via the mediating parameter, $\gamma(r)$, which behaves according to $\gamma(r) \to 0$ when $Kn \gg 1$ and $\gamma(r) \to 1$ when $Kn \ll 1$. In practice, noting that the Knudsen diffusivity equals the molecular diffusivity at $r \approx 1.6$ μm (Figure 9, left and middle), $\gamma(r)$ was itself linearly parameterized in r and bounded by r_{Kn}, the smallest pore radius observed in the distribution, and r_m, the radius at which the Knudsen diffusivity equals the molecular (Chapman-Enskog) diffusivity. The values used were $r_m = 1.6 \times 10^{-6}$ and $r_{Kn} = 1.6 \times 10^{-9}$. This linearly parameterized diffusivity, $\widetilde{D}$, is written mathematically in Equations (4-24) and (4-25) and was used in the CFD simulations in conjunction with the voxel-wise accurate pore radius.

$$\widetilde{D} = \gamma D_m + (1-\gamma) D_{Kn} \tag{4-24}$$

$$\gamma = \left(\frac{1}{r_m - r_{Kn}}\right) r - \frac{r_{Kn}}{r_m - r_{Kn}} \tag{4-25}$$

4.6 Results and Correlation for Geometric Effective Transport

Determination of $D_{O_2}^{\text{eff}}$ in the cathode by geometric transport parameters and obstruction factor first assumed that α was obtained accurately by CFD; i.e., $\alpha = \alpha_{CFD}$. Improved understanding of an *operando* PEMFC cathode for example through Direct Simulation Monte Carlo or Lattice Boltzmann methods could lead to improvement upon $\alpha = \alpha_{CFD}$ (i.e. $\alpha = \alpha_{DSMC}$ or $\alpha = \alpha_{LBM}$) but this was considered outside the scope of this paper. Over two hundred unique annealed cathodes were generated. Utilizing the methods described previously, four parameters, α_{CFD}, ε_g, τ_g, and δ_g, were determined for each unique annealed cathode; these are referred to as data in this section. Geometric tortuosity and geometric constrictivity were defined in the Methods section however, in this section, τ_g and δ_g are the mean values of twenty individual trials of the definitions provided in Methods whereby each trial began from a unique start point on the starting plane of the microstructure (cf. Figure 31). Overline notation is omitted for simplicity of reading. Multiple trials were performed and averaged to acceptably capture statistical variations.

These data were first examined for superficial trends. As discussed in Methods, the strong dependence of $S_2(r)$ on porosity resulted in annealed cathodes with precisely 35%/40%/45% porosity and no porosity values in between. This can be seen in Figure 38, on left. The range of α_{CFD} was nearly 40% of the mean value, i.e., substantial variation in $D_{O_2}^{\text{eff}}$ arose among all microstructures tested. Moreover, within a single value of porosity, the range was nearly 10% of the mean value which demonstrated that non-trivial variation

in $D_{O_2}^{\text{eff}}$ arose that could not be explained by porosity alone. In Figure 10, the transport parameters of each microstructure were plotted with a distinct color, ranging from blue for the lowest α_{CFD} through yellow/green at moderate α_{CFD} up to red for the highest α_{CFD}.

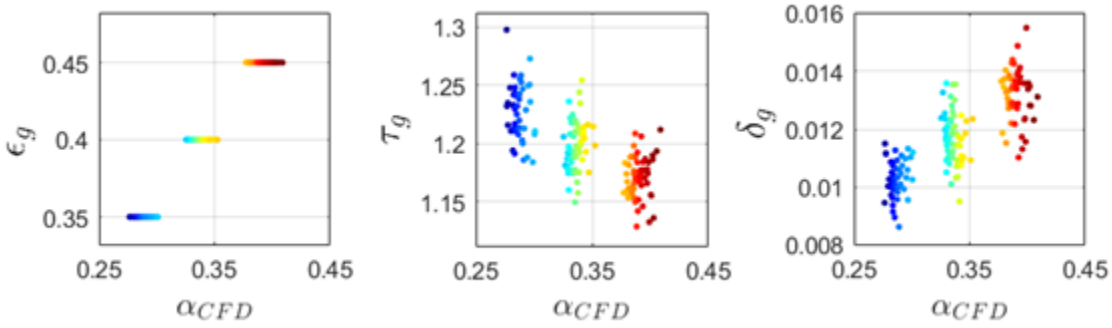

Figure 38 - Individual geometric transport parameters versus obstruction factor by CFD.

α_{CFD} was most strongly dependent on porosity, as anticipated. τ_g was consistently less than many determinations of tortuosity factor elsewhere in literature. This is in accord with the fact that the "everything else" tortuosity factor used elsewhere subsumes multiple physical phenomena, not only the elongation of fluid paths as advertised. Instead, δ_g was utilized to help account for the reduction in effective diffusion in this work. The absolute quantities of δ_g were 1-2 orders of magnitude smaller than the other parameters due to normalization by a much larger pore radius value that was chosen as to be independent of any individual annealed cathode microstructure. τ_g was inversely correlated with α_{CFD} while δ_g was directly correlated with α_{CFD} suggesting that shorter pathing was achieved in paths with less constrictive pores, as anticipated. However, significant variation arose in τ_g and δ_g at a single value of porosity which suggested that these parameters were viable candidates to account for the variation in α_{CFD} that porosity could not explain.

Determination of $D_{O_2}^{\text{eff}}$ by geometric obstruction factor also assumed that some functional form does exist, i.e., $\alpha_{CFD} = \alpha_g$, although it was initially unknown. The task was then to find the functional form, the correlation, $\alpha_g = f(\varepsilon_g, \tau_g, \delta_g)$, that acceptably minimized the difference between α_{CFD} and α_g. Toward this end, several functional forms of α_g were posited. These included optimally-fit pre-factors and/or exponents to properly scale the transport parameters, notably δ_g as previously described. A trust-region-reflective algorithm implemented in Matlab R2017b was used to determine the optimal parameters. Functional forms of α_g, the root mean squared error (RMSE) between α_{CFD} and α_g, and the values of the best-fit coefficients/exponents, γ_i, are tabulated in Table 5. Note that RMSE normalizes for the number of data points *and* the number of best-fit parameters to avoid spurious correlations due to the addition of best-fit parameters. Several different correlations were tested but four notables were tabulated and discussed.

Table 5 – Correlation functional forms for geometric obstruction factor, RMSE values, and coefficients/parameters used in each correlation.

Correlation Number	α_g	RMSE	Coefficients/Parameters
1	$\gamma_1 \varepsilon_g$	1.0e-2	γ_1 = 8.45e-1
2	$\gamma_2 \varepsilon_g / \tau_g$	9.1e-3	γ_2 = 1.01
3	$\gamma_3 \varepsilon_g \delta_g / \tau_g$	4.2e-2	γ_3 = 83.01
4	$(\gamma_{4a}\varepsilon_g)^{\gamma_{4b}}(\gamma_{4c}\delta_g)^{\gamma_{4d}}(\gamma_{4e}\tau_g)^{\gamma_{4f}}$	6.7e-3	γ_{4a} = 8.68e-1; γ_{4b} = 1.23; γ_{4c} = 3.87e2; γ_{4d} = 2.29e-6; γ_{4e} = 5.28e1; γ_{4f} = 5.18e-2

Correlation #1 was equivalent to Equation 1, $\alpha = \varepsilon/\tau$, with $\tau = 1/\gamma_1$, the most commonly applied functional form, utilizing τ as an "everything else" parameter. This is notable because, as is immediately clear from the RMSE values, Correlation #1 was not the best correlation tested. Correlation #2 incorporated τ_g and was improved from Correlation #1, albeit only slightly. Correlation #3 further incorporated δ_g. The RMSE of Correlation #3 increased from Correlations #1 and #2 although this was largely attributed to incommensurate scaling, i.e., the differing orders of magnitude, of the individual parameters as Correlation #4 used δ_g and was improved. Indeed, Correlation #4 incorporated all three geometric transport parameters and, properly scaled, further reduced the RMSE between α_{CFD} and α_g. Other correlations that were tested but not presented did not sufficiently reduce the RMSE as to warrant reporting.

In Correlation #4, the best fit pre-factors, γ_{4a}, γ_{4c}, and γ_{4e}, were of varying order of magnitude such that the product of the pre-factor and parameter were all approximately of order unity. The magnitude of the best fit exponents, γ_{4b}, γ_{4d}, and γ_{4f}, indicated the relative "predictiveness" or "importance" of the transport parameter used. This suggests that porosity was the most strongly predictive parameter of the three used with geometric tortuosity somewhat less predictive and geometric constrictivity even less predictive. This is consistent with known intuition than a porous medium's porosity will most strongly control the obstruction factor.

To validate the correlations, the four above were tested on a FIB-SEM microstructure obtained by our group, as discussed in Methods, and a FIB-SEM

microstructure obtained by Ziegler et al., who first demonstrated FIB-SEM on PEMFC cathodes.[26] For each real microstructure, the geometric parameters were obtained, α_{CFD} was determined, and the four correlations above were determined.

Table 6 – Validation of geometric transport parameters and geometric correlations compared to FIB-SEM data collected by our group and by Ziegler et al.

Parameter / Correlation	Present Work	Ziegler et al.
ε_g	0.40	0.38
τ_g	1.24	1.24
δ_g	1.14e-2	1.03-e2
α_{CFD}	0.36	0.34
$\alpha_{g,1}$	0.34	0.32
$\alpha_{g,2}$	0.33	0.31
$\alpha_{g,3}$	0.31	0.26
$\alpha_{g,4}$	0.34	0.32

In Table 2, the validations demonstrated some successes and some shortcomings. Correlation (α_g) #3 was the worst predictor of α_{CFD}, as expected based on the RMSE. Correlation #2 did not predict α_{CFD} as well as Correlation #1 for either microstructure despite achieving a lower RMSE than Correlation #1. Correlation #4 and Correlation #1 were the best predictors among the four notables. All correlations underpredicted α_{CFD} which suggested that a feature of the microstructures obtained by FIB-SEM deviated slightly from the stochastic annealed microstructures. This deviation most likely arose from

the difference in the ionomer distribution between real (FIB-SEM) cathodes and the annealed cathodes. The annealed cathodes assumed a Rayleigh-distributed, non-uniform ionomer thickness based on the extensive TEM imaging conducted on PEMFC cathodes over many years by many researchers. Nevertheless, a complete understanding of the ionomer distribution and orientation in PEMFC cathodes remains an ongoing challenge and the ionomer model assumed in this work could be considered insufficiently accurate for some applications. Excepting Correlation #2, the trends in RMSE were reasonably commensurate with the accuracy of α_{CFD} prediction.

4.7 Conclusions

A simple, inexpensive method was demonstrated for rapid, accurate determination of effective oxygen diffusivity in the cathode catalyst layer and underlying geometric transport properties. The approach relied on combining tomographic imaging data and low-resource-intensive computation. A correlation for obstruction factor based on mathematically exact definitions of geometric tortuosity and geometric constrictivity was induced from hundreds of simulated annealed cathodes.

Only a small subset of all possible correlations were tested in this work and future search could reveal further improved correlations. Alternatively, slight modifications of the geometric transport parameters utilized could capture more important statistical information relating to effective oxygen transport in the cathode.

In general, additional work should be undertaken to bridge bottom-up with top-down characterization methods on PEMFC cathodes which would add credibility to both when shown consistent. By utilizing combinations of inexpensive tools readily available to

researchers, rather than relying on a single, expensive method, iterative cathode design may accelerate ultimately leading to PEMFC components and full cells that achieve technical targets and sooner electrify the automotive sector.

CHAPTER 5. COMPARISON OF VULCAN AND HSA CARBON SUPPORTS AT TWO CATALYST LOADINGS

In this project, PEMFC cathode durability was investigated, building upon previous results and characterization capability developed in previous chapters. Vulcan and HSA carbon supports with both 0.1 and 0.2 mg/cm^2 catalyst loadings were used in performance-durability studies. FIB-SEM tomography was performed with *in silico* characterization as discussed in previous chapters. The results connect the differences in microstructure and cathode transport between two likely candidate carbons in the range of medium to low catalyst loading. The durability results have implications for future cathode design in consideration of simultaneously meeting performance, cost, and durability technical targets.

5.1 Motivation

This projected expanded upon previous results relating to microstructural collapse, corrosion, and performance, particularly cathode transport. From Chapter 2, recall that catalyst degradation and carbon support corrosion in the cathode catalyst layer were connected and several important degradation phenomena were discussed. However, the precise relationships and rates of these degradations remain poorly quantified. Catalyst nanoparticle ripening and carbon corrosion are thermodynamically favored under typical PEMFC operating conditions. Many aspects of carbon corrosion have been studied: corrosion is greatly accelerated by platinum-carbon electrocatalytic coupling and water saturation and has been implicated in multiple undesirable effects including catalyst

nanoparticle detachment, cathode layer thinning, hydrophobicity loss, and alteration of both oxygen and water transport regimes, which are carefully optimized through choice of CCL architectures and needed for cell technical targets to be met.

Although many individual effects have been demonstrated through carefully designed and controlled experiments, degradation phenomena occur simultaneously in a field-deployed PEMFC and in a highly coupled manner. Thus, understanding the relative rates of the various degradation phenomena is essential toward design of robust and high-performing cathode architectures. Having developed capability for investigating cathode microstructure and transport as described in previous chapters, this project quantified the role of microstructure and transport in both Vulcan and HSA carbon supports and 0.2 mg_{Pt}/cm^2 and 0.1 mg_{Pt}/cm^2 loadings.

5.1.1 Role of Catalyst Loading and Carbon Type

Researchers and manufacturers remain undecided as to which cathode carbon material and catalyst loading (assuming platinum or platinum alloy nanospherical catalyst for this project) would result in optimal cost-normalized performance and durability. Comparatively, Vulcan carbon is more graphitized with less primary porosity but is more resistant to corrosion. HSA carbon features greater BET surface area, greater primary porosity, improved BoL platinum dispersion, and often improved BoL performance. However, HSA carbon features a greater fraction of amorphous C-H bonds, corrodes more readily, and often exhibits more accelerated platinum degradation relative to Vulcan carbon. This highlights the tradeoff between performance and durability. For both carbons, a complete understanding of the role of mesoscale microstructure in aging remains

unknown. Reduced catalyst loading would be desirable in PEMFC applications as the platinum represents a major portion of total stack cost (cf. Figure 4). Unfortunately, an over-and-above transport resistance has been shown to arise in cathode layers as platinum loading is reduced. This resistance remains incompletely understood and this project seeks to ascertain if end of life microstructure obtained by FIB-SEM can help explain the transport losses both at moderate and low platinum loadings.

5.1.2 Role of Cathode Gas During AST

To further expand upon the work discussed in Chapter 3, the accelerated stress tests (AST) were adjusted to include oxygen in the cathode environment during accelerated stress test. Prior work has demonstrated that the presence of oxygen greatly accelerates fluoride ion emission rate and is slightly decreased when hydrogen mole fraction in the anode gas is decreased; fluoride ions could be evolved from ionomer at the cathode/PEM interface or ionomer dispersed throughout the cathode.[94] In either case, the co-presence of oxygen and hydrogen is believed to accelerate the generation rate of hydrogen peroxide and related radical species in the cathode layer. Highly reactive radical OH• and OOH• species can degrade the stable C-F bonds in PFSA via radical attack leading to bond cleavage and the observed increase in fluoride emission in the cathode effluent.[8]

5.1.3 Differential Cells

For these experiments, a differential cell was used, as was necessary for the subsequent limiting current analysis. The term "differential cell" is used to indicate that the gas composition in the flow field channels is uniform throughout the channel. To enable

these experiments, a differential cell flow field was designed and employed for the experiments in this chapter. PTFE die-cut gaskets (transparent blue in Figure 39) were used to reduce the exposed ("active") area down to 5 cm^2 (depicted in red). The catalyst coated membranes were also fabricated with reduced active area. The manifold and parallel flow channels ensured uniform gas composition and fully developed flow everywhere in the region of the active area of the flow field (excluding the "land" regions of the flow field, itself).

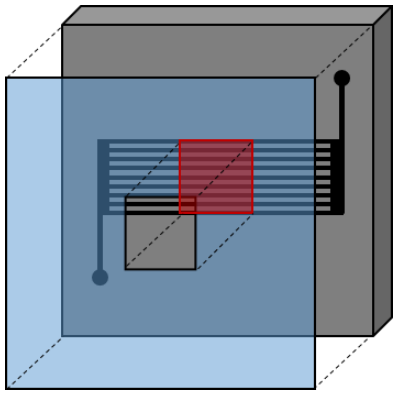

Figure 39 – Graphic of specially designed differential cell flow field with gasket (transparent blue) and active area (red)

Differential cell conditions were validated at the National Renewable Energy Laboratory on a FC test system which dynamically measured gas pressure upstream from the inlet and downstream from the outlet during all experiments. Gas stoichiometries were always above 10 and the measured pressure drop always remained at or under 4 kPa indicating that differential conditions were always achieved in the active area region of the cell at the stoichiometries and flow rates used in all experiments.

5.2 Materials

Ion Power NR-212 catalyst coated membranes of 5 cm^2 active area with 0.1 and 0.2 mg_{Pt}/cm^2 were used in all experiments. TGP-H-060 Toray carbon paper with 5% wet proofing was used as gas diffusion media (Fuel Cell Store). 152 μm (6 mil nominal) virgin PTFE (Enflo) was die-cut and used as gasket material. Cells were assembled in 5 cm^2 single cell hardware with parallel Poco graphite flow fields (Fuel Cell Technologies) as described in the Differential Cells subsection. The hardware was joined by eight bolts, each bolt spaced by eight Belleville washers, that were fastened by torque wrench set to 4.0 Nm. Cells were leak tested via N_2 pressurization at 300 kPa prior to wet up and testing. Some cell testing was performed on custom test equipment at the National Renewable Energy Laboratory and some was performed at Georgia Institute of Technology (GT). At GT, cells were tested with the same equipment as described in Chapter 3.

5.3 Methodology

5.3.1 Limiting Current Analysis

A limiting current analysis helped deconvolute the origin of transport resistances. This analysis was inspired by analyses performed by groups at Nissan, General Motors, and Toyota over the past decade.[69,95,96] The objective was to quantify the changes to the oxygen transport resistances from the flow field to the surface of the catalyst before and after the cathode was corroded.

To begin, a generalized mass transfer process was posited for oxygen transport between the channel of the flow field and catalyst surface, assuming four electron ORR, as in Equation (5-1).

$$\boldsymbol{N}_{O_2} = \frac{i_d}{4F} = \frac{1}{R_{total}}\left(C_{O_2,Ch} - C_{O_2,Pt}\right) \tag{5-1}$$

$\boldsymbol{N}_{O_2}$ is the oxygen flux, i_d is current density, F is Faraday's constant, $C_{O_2,i}$ is the oxygen concentration at either the flow-field channel or platinum surface, and R_{total} is then the lumped oxygen mass transfer resistance (reciprocal of admittance) arising between the channel of the flow field and the surface of the catalyst. The use of the differential cell hardware and operating conditions ensured that no appreciable in-plane oxygen concentration gradients existed anywhere in the cell. The oxygen transport resistances of each component, gas diffusion layer and components of the cathode catalyst layer (other), were then posed as serial resistances owing to the cell sandwich assembly as in Equation (5-2).

$$R_{total} = R_{GDL} + R_{other} \tag{5-2}$$

In this project, a microporous layer was intentionally avoided to reduce complexity in the transport analysis which was primarily intended to interrogate the cathode layer. The resistances of the cathode catalyst layer were further decomposed as in Equation (5-3) such that a gas phase and ionomer phase resistance were posited as series resistances.[69] This is justified by the fact that platinum catalyst must be coated with ionomer in order to be electrochemically active (accessible to protons *and* electrons).

$$R_{total} = R_{GDL} + R_{CCL} + R_{iono} \tag{5-3}$$

R_{CCL} was the cathode layer resistance arising from oxygen transport in the gas phase and R_{iono} was the cathode layer resistance arising from transport through ionomer before reaching catalyst.

At the limiting current, the concentration of oxygen at the surface of the platinum catalyst must be zero as additional polarization of the electrode no longer drives additional current as in Equation (5-4).

$$\boldsymbol{N}_{O_2,lim} = \frac{i_{d,lim}}{4F} = \frac{1}{R_{total}}\left(C_{O_2,Ch}\right) \tag{5-4}$$

Each transport resistance in Equation (5-3) varies in different proportion with different conditions. For example, oxygen diffusivity in the molecular regime varies as the balance gas changes but in the Knudsen regime, it does not. Limiting currents at varying cell conditions were collected to observe the difference between varying conditions and scaling relations help quantify the contribution of each component.

The resistance of the gas diffusion layer can be written as Equation (5-5).

$$R_{GDL} = \frac{L_{GDL}}{D^{eff}_{O_2,GDL}} \tag{5-5}$$

The effective diffusivity of oxygen in the gas diffusion layer was the diffusivity of oxygen in the mixture modulated by the porosity and tortuosity of the GDL.

$$D^{eff}_{O_2,GDL} = \frac{\varepsilon_{GDL}}{\tau_{GDL}} D_{O_2,mix} \tag{5-6}$$

In the GDL, the diffusivity of oxygen in the humid air mixture in the cathode was determined by Blanc's law from the binary diffusivities. [Properties of Liquids and Gases, Poling, Prausnitz, and O'Connell].

$$D_{O_2,mix} = \left(\frac{y_{N_2}}{D_{O_2,N_2}} + \frac{y_{H_2O}}{D_{O_2,H_2O}} \right)^{-1} \tag{5-7}$$

The binary diffusivity of oxygen and species j was determined according to Equation (5-8) where MM_j is the molar mass of species j and T is temperature, P is pressure, and Σ_j is the diffusion volume [Properties of Liquids and Gases, Poling, Prausnitz, and O'Connell].

$$D_{O_2,j} = \frac{0.00286 \left(\frac{1}{MM_{O_2}} + \frac{1}{MM_j} \right)^{1/2} T^{1.75}}{P \left(\Sigma_{O_2}^{1/3} + \Sigma_j^{1/3} \right)^2} \tag{5-8}$$

The cathode layer resistance is written as Equation (5-9).

$$R_{CCL} = \frac{\varepsilon_{CCL} L_{CCL}}{\tau_{CCL}} \left(\frac{1}{D_{O_2,mix}} + \frac{1}{D_{O_2,Kn}} \right) \tag{5-9}$$

Where the Knudsen diffusivity was given by (4-21) and is re-written as Equation (5-10).

$$D_{Kn} = \frac{2r}{3} \sqrt{\frac{8RT}{\pi MM_{O_2}}} \tag{5-10}$$

Following Takamura et al. and Nonoyama et al., oxygen at the void/ionomer interface is assumed to be in equilibrium at steady state according to Henry's law at the gas/ionomer

interface and is given by Equation (5-11) [Takamura et al. ECS Transactions, **16** (2) 2008; Nonoyama et al., J. Electrochem Soc. **158** (4) 2011].

$$R_{iono} = \frac{\delta_{iono}^{eff}}{A_{iono}^{eff} \psi_{iono,O_2} RT} \tag{5-11}$$

δ_{iono}^{eff} is an effective ionomer thickness, A_{iono}^{eff} is an effective gas/ionomer interfacial area, and ψ_{iono,O_2} is the ionomer permeation coefficient given by empirical correlation in Equation (5-12).

$$\psi_{iono,O_2} = 3.27 \times 10^{-15} \cdot \exp(1.28 \cdot RH) \cdot \exp\left(\frac{17200}{R}\left[\frac{1}{323.15} - \frac{1}{T}\right]\right) \tag{5-12}$$

Where RH is the relative humidity of cathode inlet gas. Limiting currents were measured for oxygen in the environment of both balance gases and at four temperatures to assess the quantitative contributions of each resistance. Molecular diffusion in the GDL is impacted by balance gas switching. Cathode gas phase diffusion and ionomer permeation are negligibly impacted by change of balance gas as the cathode pore size distribution ensured Knudsen regime diffusion was dominating (cf. Figure 34). Temperature was varied to quantify the contribution of the ionomer resistance.

5.3.2 Electrochemical Characterization

H_2/air polarization curves, H_2/air electrochemical impedance spectroscopy (EIS), and H_2/N_2 voltammetry were employed for characterization and benchmarking of fuel-cell performance. Specific cell conditions are noted with the data and presented in the Results

section. Cells were "wet-up" and broken in by sixty cycles of alternating between OCV, 0.6 V, and 0.2 V for one minute each. A N_2 "soak" was performed at the cathode after corrosion accelerated stress testing. This lowers the cell potential from an H_2/O_2 cell open circuit potential to that of an H_2/N_2 cell open circuit potential, around 0.12 V depending on the exact flow rates, temperatures, and relative humidity applied. This reduced and effectively "cleaned" oxidized and poisoned catalyst sites while allowing other weakly adsorbed material to pass from the electrode into the effluent stream. The N_2 soak was performed between AST and post-corrosion characterization to ensure observed losses were not recoverable losses[8]. Cathodic sweep polarization curves were collected following 5-minute holds at 0.3 V then the current was scanned toward open circuit voltage at 0.5 mV/s. The "beginning of life" (BOL) state of each fuel cell was assessed immediately after wet-up and break-in but with no further use. The "end of test" (EOT) state was assessed after a given corrosion protocol and after the N_2 soak. Ohmic losses and high-frequency resistance were determined by current interrupts and EIS and were found nearly unchanged before and after AST, as was intended by the design choice of thick PEM. H_2/air EIS spectra were preceded by a brief potential hold at 0.2 V followed by a ten-minute hold at the steady-state current density. The impedance response was measured from 10 kHz – 10 mHz with 5% of DC current as perturbation. To determine electrochemical surface area (ECSA), cell potential was swept between 0.05 V and 0.6 V three times at 20 mV/s while H_2/N_2 at 0.1 SLPM/0.1 SLPM and 100% RH were delivered to the cell at 40° C. For all samples, the second and third sweeps were identical and the third sweep was used to calculate electrochemical surface area by the hydrogen adsorption-related charge passed.[52]

5.4 Results

Corrosion was induced in each sample until polarization performance reached end of life according to the DOE durability target as discussed in Chapter 3. This allowed comparison of cells from beginning of life to the point as if they were at their end of service life, the first two data points needed for a long-term durability study.

The first result was the role of oxygen in the cathode during corrosion. End of life FIB-SEM porosities for the samples are shown in Table 7.

Table 7 – End of life porosity by FIB-SEM for Vulcan and HSA carbon supports at 0.2 mg/cm^2 and 0.1 mg/cm^2 catalyst loadings.

Carbon Type	Catalyst Loading [mg/cm^2]	Porosity
Vulcan	0.2	0.47
Vulcan	0.1	0.48
HSA	0.2	0.37
HSA	0.1	0.49

To the best of our knowledge, a cathode porosity fabricated with conventional methods and manufacturing techniques has never exceeded 50%. Accordingly, the end of life porosity values obtained indicated again that microstructural collapse, even in the presence of oxygen, would not likely be the primary concern when designing cathode materials and processing conditions to minimize degradation.

Limiting current data with varying carbon type, catalyst loading, balance gas, and temperature for BoL and EoL are given in Table 2. These limiting currents were subsequently used to quantify the transport resistances arising from different components of the cell.

Table 8 – Measured limiting current density data for each carbon type, loading, and balance gas at four temperatures at beginning of life and end of life.

Sample	Balance Gas	BoL $i_{d,lim}$ [mA/cm^2] at 50/60/70/80 °C	EoL $i_{d,lim}$ [mA/cm^2] at 50/60/70/80 °C
Vulcan 0.2	N_2	197/194/183/164	157/181/178/171
Vulcan 0.2	He	345/336/301/251	251/273/263/225
Vulcan 0.1	N_2	165/192/188/178	145/159/158/154
Vulcan 0.1	He	265/282/264/228	202/208/208/181
HSA 0.2	N_2	215/229/226/209	232/232/219/202
HSA 0.2	He	401/406/361/259	409/394/356/294
HSA 0.1	N_2	108/112/110/101	180/179/169/155
HSA 0.1	He	147/153/145/127	297/290/263/220

Total transport resistances were first obtained by Equation (5-4), these are plotted in Figure 40 for each carbon type and catalyst loading at both BoL and EoL.

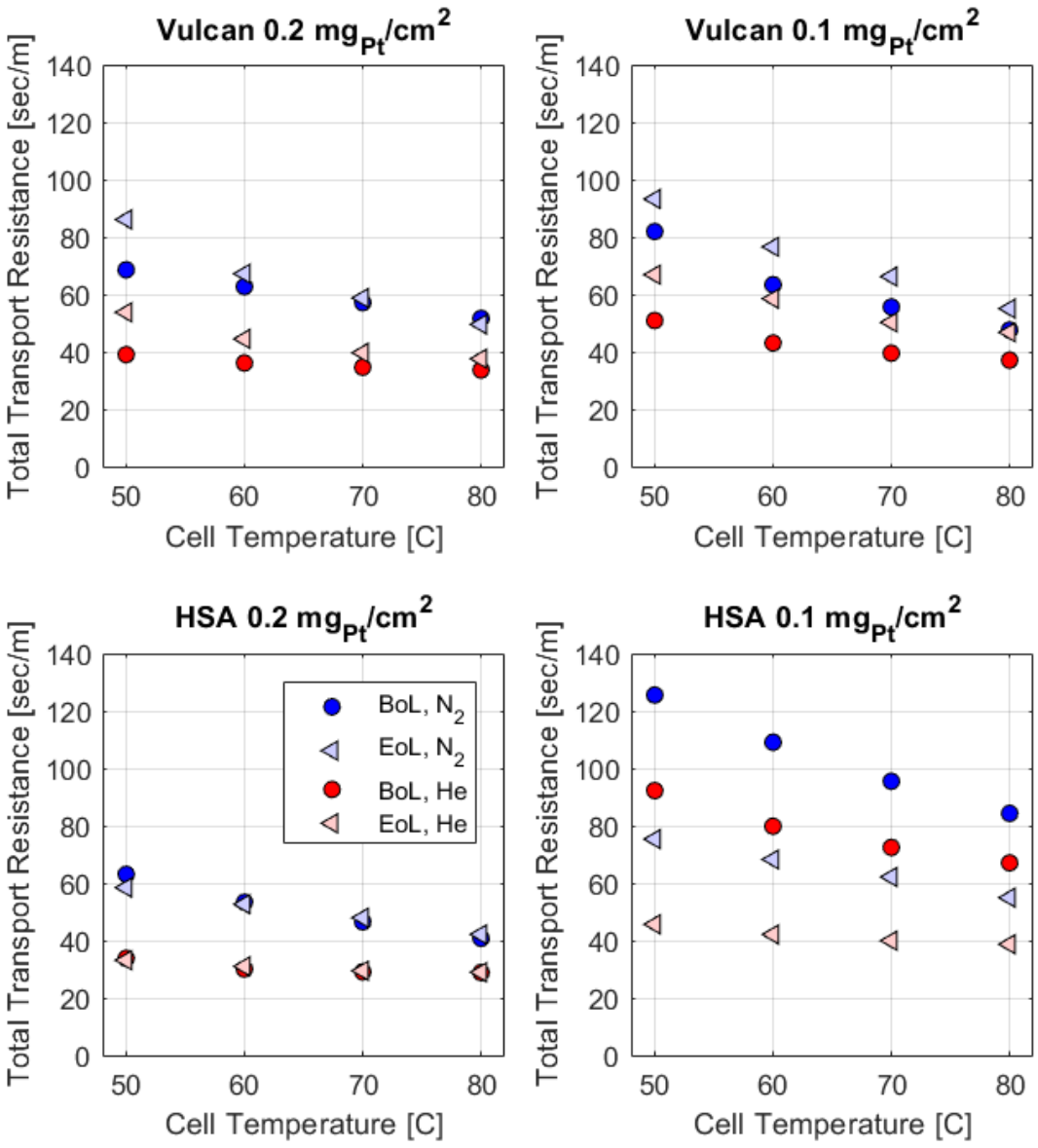

Figure 40 – Total transport resistances versus temperature at BoL and EoL in both N_2 and He balance gases.

Several trends emerge when comparing the total transport resistances. Vulcan total transport resistance was slightly greater at lower catalyst loading and increased slightly after corrosion AST at both catalyst loadings. In contrast, HSA total transport resistance began very slightly lower than Vulcan at moderate catalyst loading and was essentially

unchanged after corrosion AST while low-loaded HSA had substantially greater BoL transport resistance which *decreased* after corrosion.

To better understand these changes in total transport resistance, individual components of the cathode catalyst layer were quantified. The gas diffusion layer transport resistance and total cathode catalyst layer transport resistance (other) are plotted in Figure 41 for BoL and EoL.

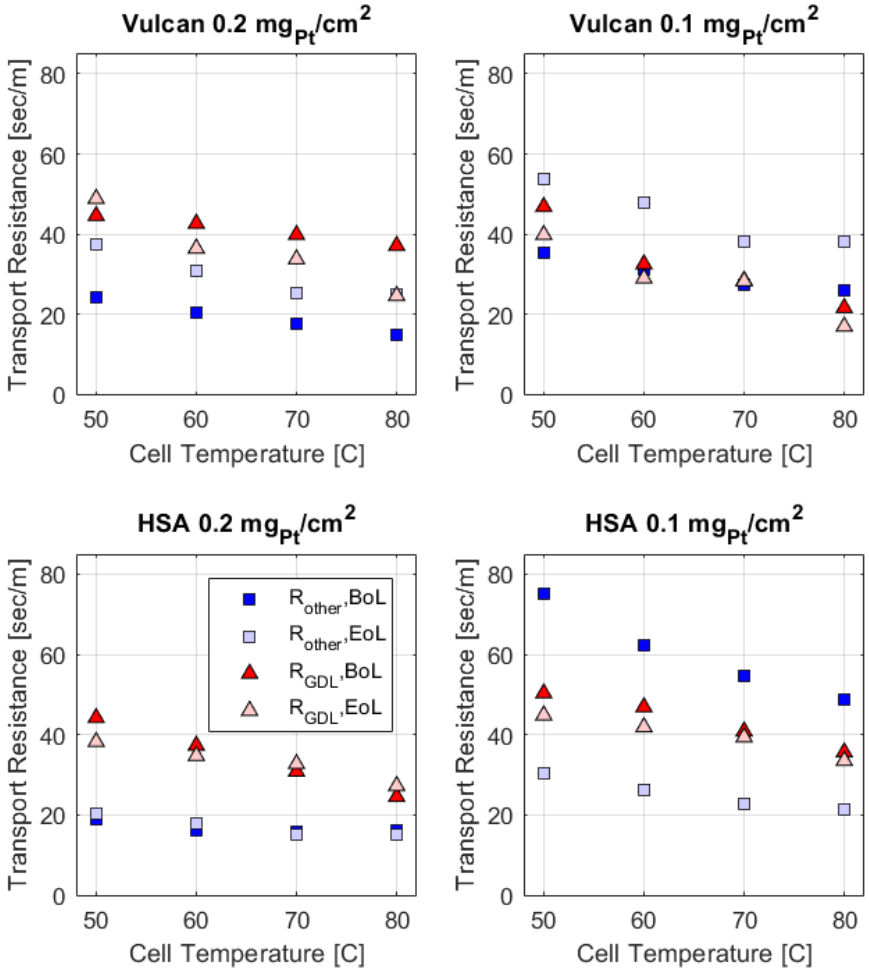

Figure 41 - GDL Resistance and "other" resistance at BoL and EoL.

The gas diffusion layer transport resistance model was reasonably constant across each cathode sample, as was anticipated due to the use of identical GDLs throughout all experiments. The considerable differences that arose in the total transport resistances were thus correctly ascribed to the CCL. The observed trends in the total transport resistances were consistent with the observed trends in the CCL (other) transport resistances. The CCL transport resistance was further decomposed into serial gas phase and ionomer phase resistances. These are plotted in Figure 42.

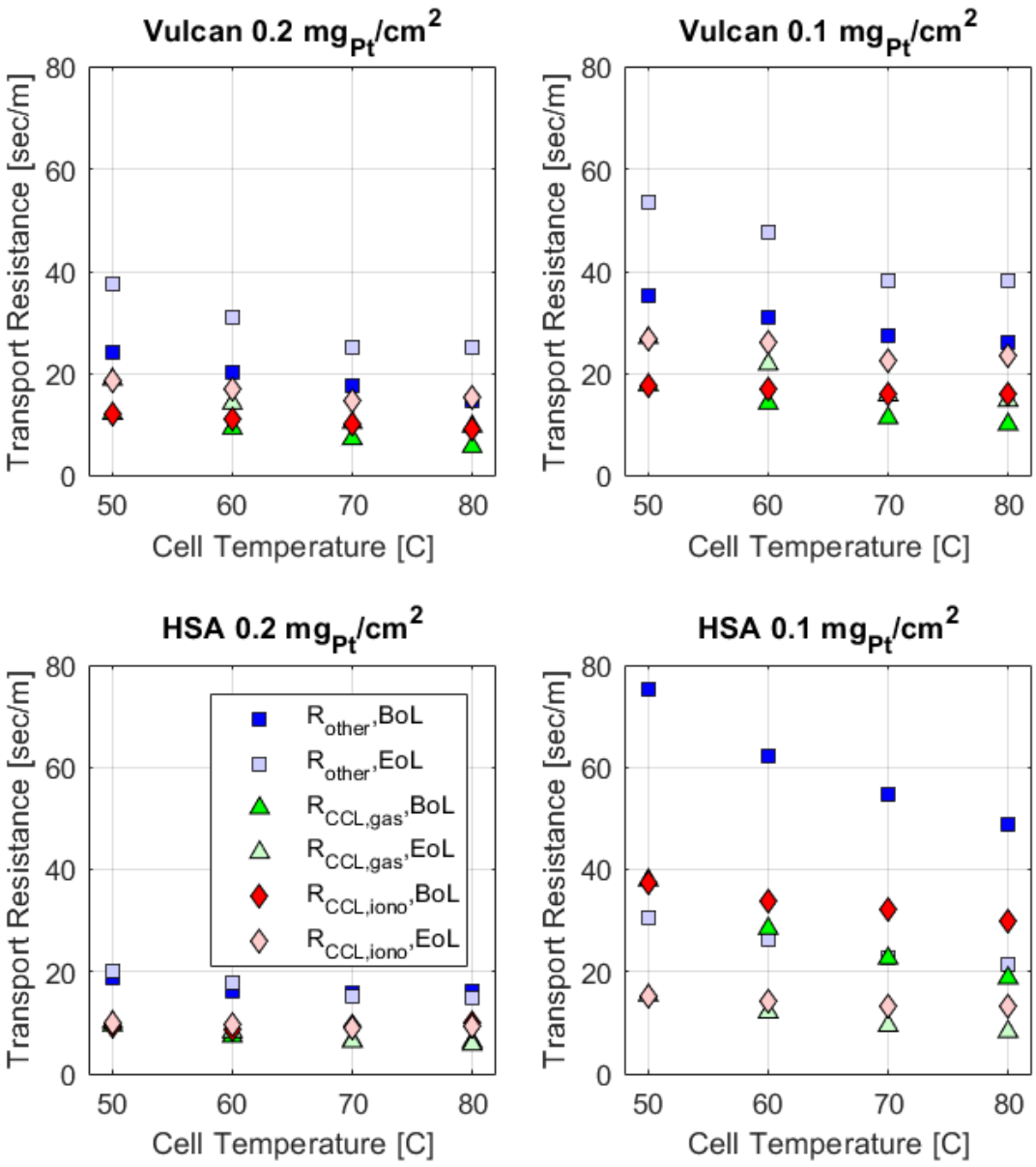

Figure 42 – Individual transport resistances in the CCL

Gas phase transport resistance was smaller than ionomer phase transport resistance for all samples at both BoL and EoL. However, between BoL and EoL, gas phase transport resistance varied more than ionomer phase transport resistance and importantly, for the low-loaded CCLs, gas phase transport resistance increased for Vulcan carbon and decreased for HSA carbon. The decrease in transport resistances for HSA at low-loading

likely resulted from the very low EoL thickness observed for this sample, estimated at around one micron as determined by cross-sectional trench milling and SEM imaging. No other sample thinned to this extent.

5.5 Conclusions

This project compared two likely candidate materials at moderate and low catalyst loadings. Performance was assessed at beginning of life and end of life and FIB-SEM microstructure was collected at end of life.

Oxygen was not found to induce microstructural collapse. Indeed, in the low loaded sample, porosity was very high, likely increased from beginning of life given its value, although the beginning of life porosity was not measured. In the larger context of PEMFC development, this is consistent with research in Chapter 3 which demonstrated that mesoscale collapse was not the most pressing concern for cathode design when attempting to mitigate cathode degradation. Confirming that the changes in transport resistances and FIB-SEM microstructure were consistent lends credibility to both techniques. This also highlights the utility of FIB-SEM as a tool for advanced characterization.

Additional modeling may better quantify the precise causes of changes the individual transport resistances by applying corrections based upon the work of complementary research in the field. Although the measurements obtained in this thesis preliminarily support the hypothesis that the “unexplained” mass transport resistance arises at or near the surface of the catalyst, further modeling will help reduce uncertainty in this claim and help shed light on relative contributions to mass transfer resistance over the course of cell life.

The fact that the transport resistances were shown to increase, remain the same, and decrease for the Vulcan 0.2, HSA 0.2, and HSA 0.1 samples, respectively, demonstrated that much more fundamental understanding of the coupled transport and microkinetics at the microscale, and relative degradation rates of the cathode materials, will be required for further improvement and rational design of cathode architectures. It is likely that the specific interplay of platinum, carbon support, and ionomer, and corrosion at the catalyst/carbon support interface, have the most significant effect on PEMFC durability. Future research such as a functionalized carbon supports for tethered catalyst particles may provide the most promising new route forward and the FIB-SEM and transport techniques developed previously could contribute toward characterization efforts in their development.

CHAPTER 6. PLATINUM PORE FILLING FOR HIGH FIDELITY *IN SITU* FIB-SEM TOMOGRAPHY

This project sought to develop and validate an enhanced method for platinum pore filling of the void space in a porous cathode to enable higher-fidelity FIB-SEM tomography. This project did not progress far enough to requisite publication, for example; however, the results were deemed interesting and potentially valuable to a future researcher.

6.1 Motivation

An improvement to our FIB-SEM method was attempted to reduce error arising from the "shine-through" problem as discussed in Chapter 2.2.2. An *in-situ* pore filling methodology was developed with promising initial results that exploited the gas injection capability present on modern dual-beam systems. Organoplatinum precursor gas (methylcyclopentadienyl [trimethyl] platinum) was injected into a small volume of interest where tomography would hypothetically be performed. Precursor gas adsorbs to the sample surface and is electronically cracked and deposited into a carbonaceous platinum coating via secondary electron (SE) emission generated by the field emission gun in the dual-chamber FIB-SEM. We label this process platinum electron beam-induced deposition (PtEBID).[97] The goal was then to develop PtEBID + FIB-SEM. We tested various combinations of application of organoplatinum precursor gas, such as continuous versus pulsed application and continuous versus pulsed electron beam application, and at different electron beam accelerating voltages and currents, to induce deposition.

This additional difficulty of PtEBID could theoretically be recouped through reduced error caused by both downstream ion milling and image processing. However, the PtEBID process itself could introduce new error. This project remains incomplete because we were unable to marshal the necessary resources to rigorously quantify the error caused by PtEBID. Lacking this analysis, we could not demonstrate potential downstream improvements in total FIB-SEM accuracy that may have been gained through simplifying ion milling and image processing. TOF-SIMS, STEM, EDS, and AFM were considered as techniques to characterize the differences between PtEBID and non-PtEBID samples and could be considered by future researchers.

6.2 Developments and Future Recommendations

Eswara-Moorthy et al. first demonstrated a platinum pore filling method on a PEMFC cathode. Their images demonstrated good contrast between the sample and pore-filling material but their downstream calculations such as cathode porosity significantly deviated from expected results. The cause of their discrepancy was not addressed and cannot be determined from their paper.[98] Prior to Eswara-Moorthy's demonstration, Botman et al. studied the elemental fraction of organoplatinum electron beam induced deposits and showed that increasing sample temperature during deposition increased the platinum to carbon ratio of the deposited material. Beneficially, our desired parameters are in the optimal regime (caveat: assumes this does not cause excessive sample heating).[99]

Figure 43 shows an example of one of our pristine cathodes before platinum pore filling and after pore filling from top and cross-sectional view.

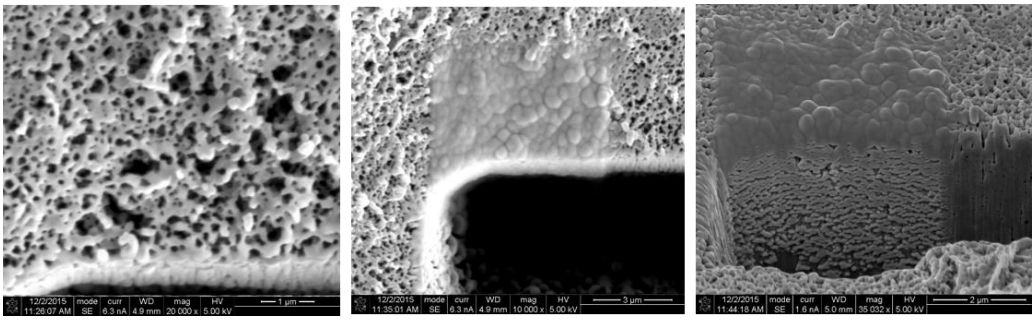

Figure 43 - Top view of ROI (left), top view after platinum deposition (middle), and cross-section view after platinum deposition (right).

Interior cross-sections after application of continuous organoplatinum gas injection and 1 hr of 29 kV and 25 nA for PtEBID show excellent contrast between the deposited platinum and the sample carbon. Figure 44 demonstrates the deposition characteristics that were achieved on a pristine cathode. The atomic contrast provides clear delineations for solid/pore segmentation by simple image processing techniques. Red arrows denote examples of interface between sample (carbon, dark) and contrast material (platinum, bright) with excellent (high gradient) contrast. Green arrows point to pore regions incompletely filled by contrasting platinum. However, these regions were not deemed problematic because simple, existing image processing algorithms were still able to easily differentiate these regions as pore phase.

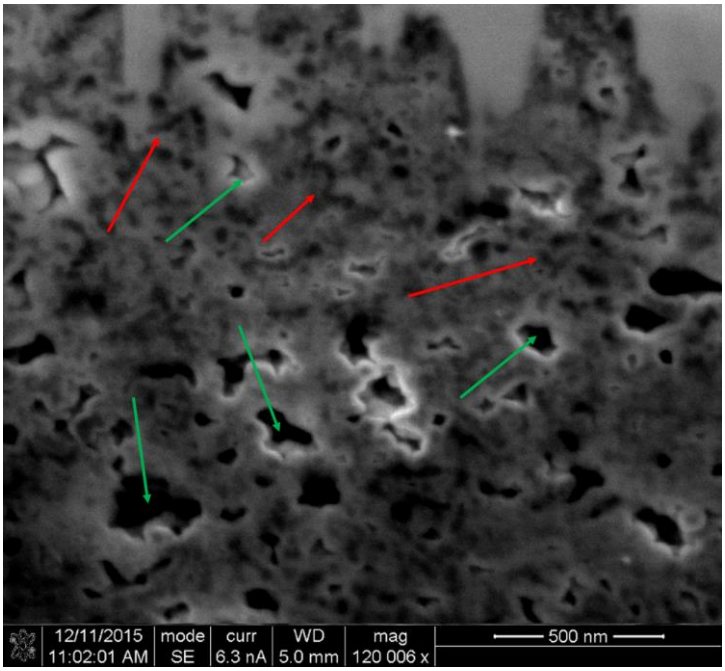

Figure 44 – Example of PtEBID interior cross section. Red arrows point to sharp contrast between deposited platinum and original sample. Green arrows point to pores that were incompletely filled but do not complicate image processing.

Progress toward optimizing image contrast and clarity included variation of suction tube voltage of the detector. Figure 45 shows contrast improvement at higher suction tube voltage, which filters the incoming electrons collected at the detector by their energies. This optimization would ultimately be essential toward achieving the best possible contrast for steep intensity gradients at the edges of particles.

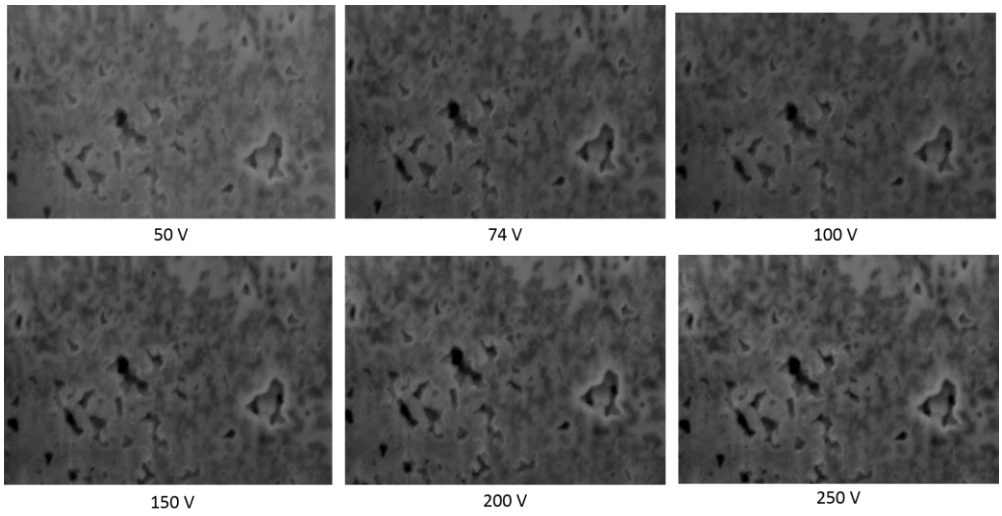

Figure 45 - SEM cross sectional images at at 5.0 kV, 1.6 nA, 35,000x mag with varying suction tube voltage to enhance contast between pore-filling platinum and sample carbon.

The results of additional workup experiments are described. A deposition time of ~10 minutes at high electron beam accelerating voltage (ca. 25 kV) and modest current (ca. 10 nA) was insufficient for complete pore filling but showed good deposition characteristics: relatively uniform deposition, i.e., on the top and bottom of sample particles, down to penetration depth of several microns. Periodic electron beam blanking (pulsed application of the electron beam) did not result in noticeable improvement and arguably worsened deposition characteristics. At 5 kV, rapid deposition took place immediately upon delivering organoplatinum gas. At 30 kV, deposition was considerably slower as compared to the 5 kV beam. This was well-explained by conventional theory [cite Reimer 1999]: greater accelerating voltage at equal current results in lower SE generation but larger sample interaction volume. This implies deeper penetration depth of the deposition, essential to the application. Greater current at equal accelerating voltage increases the SE emission rate, increases deposition rate, and increases the steady-state sample temperature

Taken together, the fact that good deposition characteristics were achieved at high accelerating voltage and modest to high current was evidence that the timescale of self-diffusion of organoplatinum gas in vacuum (~1e-6 torr) was adequately smaller than the sum of the timescales of organoplatinum gas adsorption, SE generation, and the kinetics of adsorbed organoplatinum electron-induced cracking. In other words, the deposition was either kinetically- or adsorption-limited, but not diffusion-limited at 30 kV and low current and possibly still at higher currents. Deposition times of ~1-2 hours showed complete or nearly complete deposition as in Figure 44 with good deposition characteristics.

Future work must aim to rigorously quantify the error caused by the PtEBID procedure. If PtEBID could be shown to cause negligible damage to the cathode layer microstructure, it would be an extremely valuable step toward improving the overall fidelity of FIB-SEM on PEMFC cathodes. Initial studies should seek to quantify the underlying fundamental processes involved. To begin, self-diffusion of the organoplatinum precursor gas in the porous cathode ROI must be quantified to ensure the extent of deposition would suffice for downstream FIB-SEM. This seems likely given our preliminary results. The kinetics of organoplatinum sorption-desorption onto all three constituent cathode materials, platinum catalyst, carbon support, and ionomer, should be studied on model systems such as a pure carbon black thin film, platinum(111) and/or platinum(100) crystal, and on pure PFSA thin film.

Because higher temperatures were shown to result in higher platinum to carbon ratio deposits, a higher sample temperature during deposition would be desirable. However, care must be taken not to exceed the glass transition temperature of PFSA which could lead to rearrangement of the microstructure, the most likely form of PtEBID-induced

error. A heated or cooled stage could be used although this adds cost and complexity. Ideally, improved understanding of the fundamental processes involved would lead to a procedure that utilized only the dissipated heat energy of the incident electron beam to bring the temperature of the ROI to the steady-state value determined for optimal deposition. To achieve this, heat transfer properties of the three cathode materials should be quantified including heat transfer between interfaces the three materials. Simulation software such as SRIM and TRIM could help quantify these properties to corroborate or even obviate the experiments proposed. Moreover, study of the model systems and/or extension to the cathode layer could reveal that exotic transport phenomena such as surface diffusion, thermal transpiration, and thermal diffusion could be important owing to the length scales of the system and possibly significant thermal gradients that could arise locally under the influence of the of the electron beam.

Experiments to quantify the relative secondary electron (SE) emission rates from the three constituent materials as functions of electron beam accelerating voltage and current would also be important. Low energy SEs initiate the organoplatinum cracking causing deposition. Thus, nonuniform depositions might result if the SE yields from constituent materials were significantly unequal.

TOF-SIMS, STEM, EDS, and AFM were considered as tools to characterize the differences between PtEBID and non-PtEBID samples. Lamella generation and lift-out for inspection on STEM may best reveal possible damage caused by the PtEBID procedure. Ultimately, a more robust method for characterizing the cathode layer microstructure could lead to significant improvements in PEMFC design.

CHAPTER 7. CONCLUDING REMARKS

Two ideas stand out to me upon conclusion of this dissertation. First, full cell degradation modeling is arguably the most important pursuit in contemporary PEMFC research but seems to be two problems: 1) full cell modeling as a function of constituent material structure and properties and 2) constituent material structure and properties as a function of the dynamic and conditions and hysteresis of the PEMFC materials. Improved understanding in both areas separately will likely lead to significant advances in the pursuit of full cell performance prediction over the lifetime of the cell. Improved fundamental studies, likely on model/reduced systems, to quantify the rates of coupled degradation phenomena may be required. Second, the most exciting scientific/technological advances of the past decade or more have been in machine learning, computational capabilities, and artificial intelligence. I suspect PEMFC researchers can and will benefit greatly from these advances.

REFERENCES

1. (2017) https://www.eia.gov/totalenergy/data/annual/.

2. *World Energy Outlook 2017* http://www.iea.org/Textbase/npsum/weo2017SUM.pdf.

3. Department of Defense, 1–14 (2015) http://archive.defense.gov/pubs/150724-congressional-report-on-national-implications-of-climate-change.pdf?source=govdelivery.

4. L. UChicago Argonne, https://greet.es.anl.gov/results.

5. M. L. Perry and T. F. Fuller, *J. Electrochem. Soc.*, **149**, S59 (2002) http://jes.ecsdl.org/cgi/doi/10.1149/1.1488651.

6. D. Papageorgopoulos, in *2016 Annual Merit Review and Peer Evaluation Meeting*, (2016).

7. M. K. Debe, *Nature*, **486**, 43–51 (2012).

8. R. Borup, J. Meyers, B. Pivovar, N. G. Yu Seung Kim, Rangachary Mukundan, D. Myers, M. Wilson, F. Garzon, D. Wood, P. Zelenay, K. More, K. Stroh, T. Zawodzinski, J. Boncella, O. M. I. James E. McGrath, K. Miyatake, M. Hori, K. Ota, Z. Ogumi, S. Miyata, A. Nishikata, Z. Siroma, Y. Uchimoto, K. Yasuda, K. Kimijima, and N. Iwashita, *ACS Chem. Rev.*, **107**, 3904–3951 (2007).

9. P. Trogadas, T. F. Fuller, and P. Strasser, *Carbon N. Y.*, **75**, 5–42 (2014).

10. C. Reiser, L. Bregoli, T. W. Patterson, J. S. Yi, J. D. Yang, M. L. Perry, and T. D. Jarvi,

Electrochem. Solid-State Lett., **8**, A273 (2005).

11. N. Takeuchi and T. F. Fuller, *J. Electrochem. Soc.*, **155**, B770-5 (2008).

12. L. M. Roen, C. H. Paik, and T. D. Jarvi, *Electrochem. Solid-State Lett.*, **7**, A19 (2004) http://esl.ecsdl.org/cgi/doi/10.1149/1.1630412.

13. A. Pandy, Z. Yang, M. Gummalla, V. V. Atrazhev, N. Y. Kuzminyh, V. I. Sultanov, and S. Burlatsky, *J. Electrochem. Soc.*, **160**, F972–F979 (2013).

14. R. Mukundan, G. James, D. Ayotte, J. R. Davey, D. Langlois, D. Spernjak, D. Torraco, S. Balasubramanian, A. Z. Weber, K. L. More, and R. L. Borup, *ECS Trans.*, **50**, 1003–1010 (2013).

15. Z. Y. Liu, J. L. Zhang, P. T. Yu, J. X. Zhang, R. Makharia, K. L. More, and E. A. Stach, *J. Electrochem. Soc.*, **157**, B906 (2010) http://jes.ecsdl.org/cgi/doi/10.1149/1.3391737.

16. R. L. Borup, D. D. Papadias, R. Mukundan, D. Spernjak, D. A. Langlois, R. Ahluwalia, K. L. More, and S. Grot, *ECS Trans.*, **69**, 1029–1038 (2015) http://ecst.ecsdl.org/cgi/doi/10.1149/06917.1029ecst.

17. A. A. Franco and M. Gerard, *J. Electrochem. Soc.*, **155**, B367 (2008) http://jes.ecsdl.org/cgi/doi/10.1149/1.2838165.

18. K. G. Gallagher and T. F. Fuller, *Phys. Chem. Chem. Phys.*, **11**, 11557–11567 (2009).

19. K. Malek and A. A. Franco, *J. Phys. Chem. B*, **115**, 8088–8101 (2011).

20. L. Castanheira, W. O. Silva, F. H. B. Lima, A. Crisci, L. Dubau, and F. Maillard, *ACS*

Catal., **5**, 2184–2194 (2015).

21. J. Newman and K. E. Thomas-Alyea, *Electrochemical Systems*, 3rd ed., p. 672, Wiley, (2004).

22. G. Möbus and B. J. Inkson, *Mater. Today*, **10**, 18–25 (2007).

23. J. R. Wilson, W. Kobsiriphat, R. Mendoza, H.-Y. Chen, J. M. Hiller, D. J. Miller, K. Thornton, P. W. Voorhees, S. B. Adler, and S. A. Barnett, *Nat. Mater.*, **5**, 541–544 (2006).

24. M. Ender, J. Joos, T. Carraro, and E. Ivers-Tiffee, *J. Electrochem. Soc.*, **159**, A972–A980 (2012).

25. S. Hemes, G. Desbois, J. L. Urai, B. Schröppel, and J. O. Schwarz, *Microporous Mesoporous Mater.*, **208**, 1–20 (2015).

26. C. Ziegler, S. Thiele, and R. Zengerle, *J. Power Sources*, **196**, 2094–2097 (2011).

27. H. Schulenburg, B. Schwanitz, N. Linse, G. G. Scherer, A. Wokaun, J. Krbanjevic, R. Grothausmann, and I. Manke, *J. Phys. Chem. C*, **115**, 14236–14243 (2011).

28. P. Dobson, C. Lei, T. Navessin, and M. Secanell, *J. Electrochem. Soc.*, B514–B523 (2012).

29. C. A. Volkert and A. M. Minor, *MRS Bull.*, **32**, 389–399 (2007).

30. M. Cantoni and L. Holzer, *MRS Bull.*, **39**, 354–360 (2014).

31. E. A. Wargo, T. Kotaka, Y. Tabuchi, and E. C. Kumbur, *J. Power Sources*, **241**, 608–618 (2013) http://dx.doi.org/10.1016/j.jpowsour.2013.04.153.

32. P. I. M. Ulsh, (2017).

33. D. B. V. H. A. P. S. J. Susac, *ECS Trans.*, **50**, 405–413 (2012).

34. L. A. Giannuzzi and F. A. Stevie, *Introduction to focused ion beams: Instrumentation, theory, techniques and practice*, p. 1-357, (2005).

35. T. Prill, K. Schladitz, D. Jeulin, M. Faessel, and C. Wieser, *J. Microsc.*, **250**, 77–87 (2013).

36. M. Klingele, R. Zengerle, and S. Thiele, *J. Power Sources*, **275**, 852–859 (2015).

37. B. P. Setzler and T. F. Fuller, *J. Electrochem. Soc.*, **162**, F519–F530 (2015) http://jes.ecsdl.org/cgi/doi/10.1149/2.0361506jes.

38. R. F. Egerton, P. Li, and M. Malac, *Micron*, **35**, 399–409 (2004).

39. S. J. Osborn, M. K. Hassan, G. M. Divoux, D. W. Rhoades, K. A. Mauritz, and R. B. Moore, *Macromolecules*, **40**, 3886–3890 (2007).

40. ImageJ, *IJ 1.46r*, 187 (2003) http://rsbweb.nih.gov/ij/docs/guide/user-guide.pdf.

41. T. Prill and K. Schladitz, *Scanning*, **35**, 189–95 http://www.ncbi.nlm.nih.gov/pubmed/22915353.

42. T. Prill, K. Schladitz, D. Jeulin, M. Faessel, and C. Wieser, *J. Microsc.*, **250**, 77–87 (2013).

43. M. Salzer, S. Thiele, R. Zengerle, and V. Schmidt, *Mater. Charact.*, **95**, 36–43 (2014).

44. M. Salzer, T. Prill, A. Spettl, D. Jeulin, K. Schladitz, and V. Schmidt, *J. Microsc.*, **257**, 23–30 (2015) http://www.ncbi.nlm.nih.gov/pubmed/25231671.

45. C. Kim and C. J. Kuo, *Spring Briefs in Electrical and Interactive Segmentation Techniques Algorithms and Performance Evaluation* C. J. Kuo and W.-S. Gan, Editors, Springer New York, Singapore, (2014).

46. J. Sauvola and M. Pietikäinen, *Pattern Recognit.*, **33**, 225–236 (2000).

47. A. Ramkumar, P. J. Stappers, W. J. Niessen, S. Adebahr, T. Schimek-jasch, U. Nestle, Y. Song, A. Ramkumar, P. J. Stappers, W. J. Niessen, and S. Adebahr, *Int. J. Human–Computer Interact.*, **0**, 1–12 (2016).

48. L. Reimer, *Scanning Electron Microscopy: Physics of Image Formation and Microanalysis* D. P. W. Hawkes, Editor, 2nd ed., Springer-Verlag Berlin, Heidelberg, (1998).

49. A. P. Young, J. Stumper, and E. Gyenge, *J. Electrochem. Soc.*, **156**, B913 (2009).

50. K. L. More, in *DOE Hydrogen and Fuel Cell Program 2013 Annual Merit Review Proceedings*,, Arlington, VA (2013).

51. S. Abbou, J. Dillet, D. Spernjak, R. Mukundan, J. D. Fairweather, R. L. Borup, G. Maranzana, S. Didierjean, and O. Lottin, *ECS Trans.*, **58**, 1631–1642 (2013).

52. K. M. and S. G. Rodney L. Borup, D. D. Papadias, Rangachary Mukundan, Dusan Spernjak, David Langlois, R. Ahluwalia, *ESC Trans.*, **69**, 1029–1038 (2015).

53. F. A. Coutelieris and J. M. P. Q. Delgado, (2012).

54. E. W. Dijkstra, *Numer. Math.*, **1**, 269–271 (1959).

55. S. Torquato, *Random Heterogeneous Materials*, Springer New York, New York, NY, (2002).

56. *Fuel Cell Technologies Office Multi-Year Research, Development, and Demonstration Plan*, p. 1-58, (2016) https://energy.gov/sites/prod/files/2016/10/f33/fcto_myrdd_fuel_cells.pdf.

57. A. Z. Weber, R. L. Borup, R. M. Darling, P. K. Das, T. J. Dursch, W. Gu, D. Harvey, A. Kusoglu, S. Litster, M. M. Mench, R. Mukundan, J. P. Owejan, J. G. Pharoah, M. Secanell, I. V Zenyuk, P. Systems, and B. C. Vj, **161**, 1254–1299 (2014).

58. B. P. Setzler, thesis, Georgia Institute of Technology (2015).

59. P. J. Ferreira, G. J. la O', Y. Shao-Horn, D. Morgan, R. Makharia, S. Kocha, and H. A. Gasteiger, *J. Electrochem. Soc.*, **152**, A2256 (2005).

60. S. Maass, F. Finsterwalder, G. Frank, R. Hartmann, and C. Merten, *J. Power Sources*, **176**, 444–451 (2008).

61. L. Melo, A. P. Hitchcock, V. Berejnov, D. Susac, J. Stumper, and G. A. Botton, *J. Power Sources*, **312**, 23–35 (2016).

62. Z. Y. Liu, J. L. Zhang, P. T. Yu, J. X. Zhang, R. Makharia, K. L. More, and E. a. Stach, *J. Electrochem. Soc.*, **157**, B906 (2010).

63. P. T. Yu, W. Gu, R. Makharia, F. T. Wagner, and H. A. Gasteiger, in *ECS Transactions*,, vol. 3, p. 797–809, ECS (2006).

64. D. Spernjak, J. Fairweather, R. Mukundan, T. Rockward, and R. L. Borup, *J. Power Sources*, **214**, 386–398 (2012).

65. K. G. Gallagher, D. T. Wong, and T. F. Fuller, *J. Electrochem. Soc.*, **155**, B488 (2008).

66. J. M. Zalc, S. C. Reyes, and E. Iglesia, *Chem. Eng. Sci.*, **59**, 2947–2960 (2004).

67. P. C. Carman, *Trans. Inst. Chem. Eng.*, **75**, S32–S48 (1937) http://linkinghub.elsevier.com/retrieve/pii/S0263876297800032.

68. M. M. Mench, *Fuel Cell Engines*, p. 1-515, John Wiley and Sons, (2008).

69. N. Nonoyama, S. Okazaki, A. Z. Weber, Y. Ikogi, and T. Yoshida, *J. Electrochem. Soc.*, **158**, B416 (2011).

70. E. Ferrando-May, H. Hartmann, J. Reymann, N. Ansari, N. Utz, H. U. Fried, C. Kukat, J. Peychl, C. Liebig, S. Terjung, V. Laketa, A. Sporbert, S. Weidtkamp-Peters, A. Schauss, W. Zuschratter, and S. Avilov, *Microsc. Res. Tech.*, **79**, 463–479 (2016).

71. B. Tjaden, D. J. L. Brett, and P. R. Shearing, *Int. Mater. Rev.*, **6608**, 1–21 (2016) https://www.tandfonline.com/doi/full/10.1080/09506608.2016.1249995.

72. M. B. Clennell, *Geol. Soc. London, Spec. Publ.*, **122**, 299–344 (1997).

73. Y. Ichikawa and A. P. S. Selvadurai, *Transport Phenomena in Porous Media*, 1st ed., Springer-Verlag Berlin, Heidelberg, (2012).

74. S. Chapman and T. G. Cowling, *The Mathematical Theory of Non-Uniform Gases*, Third., Cambridge University Press, Cambridge, (1995).

75. P. K. Sinha, P. Halleck, and C.-Y. Wang, *Electrochem. Solid-State Lett.*, **9**, A344 (2006) http://esl.ecsdl.org/cgi/doi/10.1149/1.2203307.

76. A. Bazylak, *Int. J. Hydrogen Energy*, **34**, 3845–3857 (2009) http://dx.doi.org/10.1016/j.ijhydene.2009.02.084.

77. H. Wu, B. Khaykovich, X. Wang, and D. S. Hussey, *Phys. Procedia*, **88**, 184–189 (2017) http://dx.doi.org/10.1016/j.phpro.2017.06.025.

78. K. More, B. Sneed, and D. Cullen, in *ECS Conference: ORR III (Noble Metal)*, (2016).

79. A. Curtis, C. Calvi, J. Tinsley, R. Hollinger, V. Kaymak, A. Pukhov, S. Wang, A. Rockwood, Y. Wang, V. N. Shlyaptsev, and J. J. Rocca, *Nat. Commun.*, **9**, 1077 (2018) http://www.nature.com/articles/s41467-018-03445-z.

80. K. Vafai, *Handbook of Porous media*, 2nd ed., Taylor & Francis Group, LLC, Boca Raton, (2005).

81. F. Yang, F. F. Hingerl, X. Xiao, Y. Liu, Z. Wu, S. M. Benson, and M. F. Toney, *Sci. Rep.*, **5**, 10635 (2015) http://www.nature.com/srep/2015/150603/srep10635/full/srep10635.html.

82. M. J. Blunt, B. Bijeljic, H. Dong, O. Gharbi, S. Iglauer, P. Mostaghimi, A. Paluszny, and C. Pentland, *Adv. Water Resour.*, **51**, 197–216 (2013) http://dx.doi.org/10.1016/j.advwatres.2012.03.003.

83. D. Silin and T. Patzek, *Phys. A Stat. Mech. its Appl.*, **371**, 336–360 (2006).

84. W. K. Epting, J. Gelb, and S. Litster, *Adv. Funct. Mater.*, **22**, 555–560 (2012).

85. J. van Brakel and P. M. Heertjes, *Int. J. Heat Mass Transf.*, **17**, 1093–1103 (1974).

86. C. L. Y. Yeong and S. Torquato, *Phys. Rev. E*, **58**, 224–233 (1998).

87. P. P. Mukherjee and C.-Y. Wang, *J. Electrochem. Soc.*, **153**, A840 (2006) http://jes.ecsdl.org/content/153/5/A840.full.

88. G. Inoue and M. Kawase, *J. Power Sources*, **327**, 1–10 (2016) http://dx.doi.org/10.1016/j.jpowsour.2016.07.037.

89. S. H. Kim and H. Pitsch, *J. Electrochem. Soc.*, **156**, B673 (2009) http://jes.ecsdl.org/cgi/doi/10.1149/1.3106136.

90. I. C. B. Association, *Carbon Black User's Guide*, p. 36, (2016) http://www.carbon-black.org/images/docs/2016-ICBA-Carbon-Black-User-Guide.pdf.

91. A. Kusoglu and A. Z. Weber, *Chem. Rev.*, **117**, 987–1104 (2017).

92. R. B. Bird, W. E. Stewart, and E. N. Lightfoot, *Transport Phenomena* W. Anderson, K. Hepburn, P. Kulek, M. Lesure, and G. Aiello, Editors, 2nd ed., John Wiley and Sons, Inc., New York, (2002).

93. R. Cunningham, *Diffusion in Gases and Porous Media*, 1st ed., Springer US, New York, (1980).

94. J. M. Fenton, M. P. Rodgers, D. K. Slattery, X. Huang, V. O. Mittal, L. J. Bonville, and H. R. Kunz, *ESC Trans.*, **25**, 233–247 (2009).

95. T. Mashio, A. Ohma, S. Yamamoto, K. Shinohara, E. C. S. Transactions, and T. E.

Society, *ECS Trans.*, **11**, 529–540 (2007) http://ecst.ecsdl.org/content/11/1/529.abstract.

96. D. R. Baker, D. A. Caulk, K. C. Neyerlin, and M. W. Murphy, *J. Electrochem. Soc.*, **156**, B991 (2009) http://jes.ecsdl.org/cgi/doi/10.1149/1.3152226.

97. FEI, *Using beam chemistries with SEM , FIB and DualBeam ™ for surface modification*, (2015) http://marketing.fei.com/acton/attachment/4019/f-0254/1/-/-/l-004f/l-004f:3f0c/file.pdf.

98. S. K. Eswara-Moorthy, P. Balasubramanian, W. Van Mierlo, J. Bernhard, M. Marinaro, M. Wohlfahrt-Mehrens, L. J??rissen, and U. Kaiser, *Microsc. Microanal.*, **20**, 1576–1580 (2014).

99. A. Botman, M. Hesselberth, and J. J. L. Mulders, *Microelectron. Eng.*, **85**, 1139–1142 (2008).